

**ULTRATHIN BLACK PHOSPHORUS: A NEW
HIGH-MOBILITY TWO-DIMENSIONAL
SEMICONDUCTOR**

ROSTISLAV A. DOGANOV

NATIONAL UNIVERSITY OF SINGAPORE

2017

**ULTRATHIN BLACK PHOSPHORUS:
A NEW HIGH-MOBILITY TWO-DIMENSIONAL
SEMICONDUCTOR**

ROSTISLAV A. DOGANOV

(Dipl.-Phys., Heidelberg University)

**A THESIS SUBMITTED
FOR THE DEGREE OF DOCTOR OF PHILOSOPHY**

Supervisor: Prof Barbaros Özyilmaz

Examiners: Asst Prof José Carlos Viana-Gomes

Asst Prof Quek Su Ying

Prof Gregory Stewart, University of Florida

**NUS GRADUATE SCHOOL FOR INTEGRATIVE
SCIENCES AND ENGINEERING
NATIONAL UNIVERSITY OF SINGAPORE**

2017

DECLARATION

I hereby declare that this thesis is my original work and it has been written by me in its entirety. I have duly acknowledged all the sources of information which have been used in the thesis.

This thesis has not been submitted for any degree in any university previously.

Rostislav Doganov

13 January 2017

Acknowledgments

I would like to thank Prof Barbaros Özyilmaz for giving me the opportunity to conduct research and pursue a PhD degree in his laboratory. I am grateful to Prof Antonio Castro Neto and Prof Vitor Pereira for being part of the thesis advisory committee and for providing valuable feedback.

I especially thank Dr Steven Koenig for a friendly and productive collaboration throughout the work in this thesis. I am grateful to Dr Eoin O'Farrell for his friendship and guidance in low-temperature transport measurements. I also want to thank Jun You Tan and Yuting Yeo for their tireless support in the cleanroom micro-fabrication facility.

I want to thank all members of Prof Özyilmaz's group for creating a friendly and competitive research atmosphere. In particular, I would like to thank Eeshan Kulkarni, Dr Henrik Andersen, Dr Gavin Koon, Dr Ahmet Avsar, and Dr Alexander Mayorov. I am also grateful to Dr Alexandra Carvalho for providing theoretical support for some of the experimental work.

Most importantly, I am filled with gratitude towards my family - my wife, my mother, and my sister - for their unconditional love, support, and understanding during the course of the PhD.

Contents

1	Introduction: From Prehistory to Graphene and Beyond	1
2	Review of Basic Concepts	5
2.1	Two-Dimensional Materials	5
2.1.1	Graphene	6
2.1.2	Monolayer Transition Metal Dichalcogenides	9
2.1.3	Hexagonal BN and Other 2D Materials	13
2.1.4	Van der Waals heterostructures	15
2.2	Field-Effect Transistors Based on 2D Materials	16
2.2.1	The Capacitor Model and On-State Operation	16
2.2.2	Schottky Barrier Height and Sub-Threshold Operation	20
2.3	Material Properties of Bulk Black Phosphorus	23
3	Experimental Methods	30
3.1	Micromechanical Exfoliation	30
3.2	Dry Transfer Method	32
3.3	Raman Spectroscopy	37
3.4	Atomic Force Microscopy	38
3.5	Micro-fabrication of Electrical Contacts	40

3.5.1	Electron Beam Lithography	41
3.5.2	Thermal Evaporation and Lift-off	43
3.6	Packaging and Wire-bonding	43
3.7	Electrical Transport Measurements	44
3.8	Low-Temperature and Magnetic Field Measurements	45
4	Results	46
4.1	Electrical Transport in Bulk bP	46
4.2	Electric Field Effect in Few-layer bP	48
4.3	Van der Waals Passivation of Few-layer bP in Inert Atmosphere	52
4.4	Electrical Properties of Few-Layer bP on hBN	62
4.5	N-type Doping of Few-Layer Phosphorene Using Metal Adatoms	71
5	Critical Discussion	90
5.1	Comparison to Results from the Literature	90
5.1.1	Isolation and Electrical Characterization of Ultrathin bP	90
5.1.2	Passivation of Ultrathin bP	93
5.1.3	High-Mobility Ultrathin bP on hBN Substrate	96
5.1.4	Adatom Functionalization and Electron Doping of Ultrathin bP	97
5.2	What Makes Phosphorene Interesting?	98
5.3	Ultrathin bP for opto-electronic applications	99
5.4	Ultrathin bP: Prospects and Future Challenges	100
5.4.1	Large-scale Growth of Ultrathin bP	101
5.4.2	Isolation and Characterization of High-Quality Monolayers	102
5.4.3	Optimization of the Device Control	102
5.4.4	Long-term Passivation	103

Summary

A unique combination of physical properties, i.a. high crystallinity, excellent transport characteristics, high mechanical strength, two-dimensional (2D) carrier confinement, high optical transparency, and mechanical flexibility has made 2D materials a fascinating playground for basic science and applied research. Following the first isolation of graphene in 2004, the research focus during the past decade was on studying the material properties of graphene and members of the transition metal dichalcogenide family, and in particular of MoS₂. However, the search for new and better semiconducting 2D materials is still ongoing.

In this thesis I report on the isolation and experimental characterization of electrical transport properties of a new 2D crystal consisting of phosphorus atoms. The ultrathin material was exfoliated from bulk black phosphorus (bP) and is now known as ultrathin bP, or phosphorene. The results in this thesis comprise electrical transport characterization of phosphorene and experiments on the crystal's degradation, surface passivation, and functionalization with metal adatoms. The experiments and critical discussions aim to analyze phosphorene's prospects to serve as a 2D semiconductor for field effect transistors.

In particular, we performed charge transport measurement and show that ultrathin bP is a semiconductor that exhibits both a higher carrier mobility than MoS₂, and allows higher on-off current ratio than in graphene transistors. In contrast to

MoS₂ and graphene, phosphorene is found to react with air and to gradually degrade in ambient atmosphere. The observed chemical instability led to research on passivation of the crystal. We demonstrate a method to encapsulate phosphorene by incorporating it in a 2D heterostructure in inert atmosphere, thereby covering it with graphene or hexagonal boron nitride (hBN). This allows us to measure the charge transport properties of ultrathin bP samples which have not undergone any oxidation and to study the pristine material. The results reveal an improvement in n-type charge transport and nearly symmetric carrier mobility for electrons and holes in passivated samples. This sheds light on the crystal's intrinsic properties and the unintentional p-type doping caused by degradation. We further perform a comparative study of the transport properties of ultrathin bP on SiO₂ and hBN. It is found that hBN provides a superior substrate than SiO₂ and that vacuum annealing can de-oxidize ultrathin bP and improve the n-type charge transport. As a next step, this allows us to study the controlled doping of ultrathin bP by metal adatoms and to develop a method to reproducibly lower the threshold voltage for n-type transport. The research culminates in the demonstration of a scalable ultrathin bP voltage inverter, fabricated on an hBN substrate with selective adatom channel doping, which exhibits the highest inverter gain and the best noise margins achieved with 2D materials to date.

List of publications

Results of this thesis were published in the following peer-reviewed articles:

1. Applied Physics Letters **104**, 103106 (2014), “*Electric field effect in ultrathin black phosphorus*”, Steven P. Koenig, **Rostislav A. Doganov**, Hennrik Schmidt, A. H. Castro Neto, and Barbaros Özyilmaz.
2. Nature Communications **6**, 6647 (2014), “*Transport properties of pristine few-layer black phosphorus by van der Waals passivation in an inert atmosphere*”, **Rostislav A. Doganov**, Eoin C.T. O’Farrell, Steven P. Koenig, Yuting Yeo, Angelo Ziletti, Alexandra Carvalho, David K. Campbell, David F. Coker, Kenji Watanabe, Takashi Taniguchi, Antonio H. Castro Neto, and Barbaros Özyilmaz.
3. Applied Physics Letters **106**, 083505 (2015), “*Transport properties of ultrathin black phosphorus on hexagonal boron nitride*”, **Rostislav A. Doganov**, Steven P. Koenig, Yuting Yeo, Kenji Watanabe, Takashi Taniguchi, and Barbaros Özyilmaz.
4. Nano Letters **16**, 2145 (2016), “*Electron Doping of Ultrathin Black Phosphorus with Cu Adatoms*”, Steven P. Koenig, **Rostislav A. Doganov**, Leandro Seixas, Alexandra Carvalho, Jun You Tan, Kenji Watanabe, Takashi Taniguchi, Nikolai Yakovlev, Antonio H. Castro Neto, and Barbaros Özyilmaz.

List of Tables

2.1	Effective carrier masses in bulk black phosphorus.	28
2.2	Summary of the electrical properties of bulk black phosphorus.	29
4.1	Comparison of the effective carrier masses for electrons and holes of some common semiconductors.	72

List of Figures

2.1.1 Crystal and band structure of graphene.	7
2.1.2 Periodic table of monolayer transition metal dichalcogenides and their lattice structure.	10
2.1.3 Schematic of the progressive filling of d-orbitals in monolayer transition metal dichalcogenides.	12
2.1.4 Known families of two-dimensional materials.	14
2.2.1 Schematic of a monolayer MoS ₂ field-effect transistor. Experimental validation of the parallel-plate capacitor model in the on-state of MoS ₂ and ultrathin black phosphorus.	19
2.2.2 Schematic and experimental validation of the Schottky-barrier sub-threshold model of Penumatcha, Salazar, and Appenzeller.	22
2.3.1 Lattice structure of black phosphorus.	25
2.3.2 Band structure of bulk black phosphorus and schematic of the 3p orbital band gap formation.	27
3.1.1 Optical images of bulk black phosphorus crystals and exfoliated material on Nitto tape.	31
3.2.1 A step-by-step schematic of the dry transfer method for creating van der Waals heterostructures.	33

3.2.2 Optical images of the custom tools used in the dry transfer method.	35
3.2.3 Optical images of the alignment platform used in the dry transfer method.	37
3.3.1 Angular dependence of the polarization-resolved Raman spectrum of black phosphorus.	39
3.4.1 Specifications of the Bruker FASTSCAN-A AFM tip.	40
3.5.1 Micrograph of a wafer with exfoliated black phosphorus after EBL marker writing. A representative EBL design for electrode fabrication.	42
3.6.1 Optical images of the used device packaging and the 16 Tesla cryogen-free low-temperature measurement system.	44
4.1.1 Measured resistivity, carrier concentration, and Hall mobility of a bulk black phosphorus.	47
4.2.1 Lattice structure, optical micrograph, AFM scan, and Raman spectrum of exfoliated black phosphorus.	49
4.2.2 In situ observation of the degradation of exfoliated black phosphorus by measuring the AFM roughness.	50
4.3.1 AFM demonstration of the passivating effect of graphene and hBN transferred onto ultrathin black phosphorus.	54
4.3.2 Optical micrograph and Raman characterization of degraded and passivated ultrathin black phosphorus.	56
4.3.3 Comparison of the electrical transport in passivated and air-exposed ultrathin black phosphorus.	58
4.3.4 Two-probe electrical characterization of a passivated ultrathin black phosphorus field-effect transistor exhibiting symmetric electron and hole transport.	61

4.4.1 Device schematic, optical micrograph, Raman spectrum, and gate-dependent conductance of ultrathin black phosphorus on hBN.	64
4.4.2 Conductance and mobility of ultrathin black phosphorus on hBN at $T = 190$ K.	66
4.4.3 Measurements and numerical modeling of the temperature-dependent mobility in ultrathin black phosphorus on hBN.	67
4.4.4 Comparison of the gate-dependent conductance of ultrathin black phosphorus on SiO ₂ and hBN.	70
4.5.1 Calculated band structure of four-layer black phosphorus with atomic Cu dopants.	74
4.5.2 AFM image showing the clustering of Cu deposited by thermal evaporation onto ultrathin black phosphorus.	76
4.5.3 AFM, XPS, UPS and ToF-SIMS characterization of the Cu adatom deposition.	77
4.5.4 Comparison of the electrical characteristics of ultrathin black phosphorus before and after Cu deposition.	80
4.5.5 Conductance versus gate voltage showing the doping of ultrathin black phosphorus by Cu, Ag, and Au adatoms.	82
4.5.6 Characterization of a p-FET and n-FET fabricated by the selective Cu adatom doping of a graphene/hBN/bP heterostructure.	84
4.5.7 Electrical characterization of a voltage inverter fabricated from graphene, hBN, and ultrathin black phosphorus.	86
4.5.8 Electrical characterization of the voltage inverter at elevated temperature and over a period of 10 days in vacuum.	87
4.2.3 Electrical characteristics of a black phosphorus field-effect device. . .	89

5.1.1 Thickness-dependent mobility and conductance anisotropy of exfoliated black phosphorus.	92
5.1.2 Electrical characterization of ultrathin black phosphorus passivated with ALD-grown AlO_x	94
5.1.3 Optical micrograph of an ultrathin black phosphorus crystal fully encapsulated with hBN and contacted using graphene electrodes. Source-drain current versus gate voltage of the device.	95
5.1.4 Quantum oscillations in the resistance of high-mobility ultrathin black phosphorus at low temperature and in high magnetic field.	96
5.1.5 Electrical characterization of ultrathin black phosphorus with additional electron doping by Cs_2CO_3 and Al-atom deposition.	97

Chapter 1

Introduction: From Prehistory to Graphene and Beyond

The technological development of mankind is closely connected to the discovery of new materials. For example, one of the most established methods for classifying different technological periods in human prehistory is using the three-age system, which names the age after the predominant material of the time: the stone age, the bronze age, and the iron age.[1] Technological progress to a new period is connected with the discovery of a new material or significant improvements in material processing. The transition from the stone to the bronze age required the development of mining and the building of furnaces with high enough temperatures to melt the bronze alloy. The subsequent progress towards the iron age required significant improvements in the methods for purifying iron ore (which is naturally more abundant than copper and tin) and the development of forging to make iron harder than bronze.[2]

Following this line of thought, and the history in metallurgy, it is interesting to speculate on the most important and characteristic material for mankind today. It appears that our age is characterized by the rapid developments in electronics and

information technology. For the past several decades digital device technology, and in particular computers, have been transforming human society in a way that many compare in scale to the transformations brought by the industrial revolution of the 19-th century.[3] From a materials science perspective, at the heart of this transformation is mankind's unprecedented understanding and application of semiconductor materials. Of all known semiconductors by far the most wide-spread, technologically important, and naturally abundant is Silicon. It can therefore be argued that we are currently in an age which could be called the "Silicon age".

During the past 40 years the hallmark of Si technology has been its ability to constantly miniaturize the transistor device in dense integrated circuits. This has resulted in a continuous exponential growth of the number of transistors in a digital micro-processor. For example, the Intel "4004" processor from the year 1971 features 2300 transistors, while a modern Intel "Core" chip packs more than 1 000 000 000.[4] This exponential growth in transistor count has directly resulted in an increase in computational complexity, improved processor capabilities, and increased digital memory storage. This, in turn, has allowed the chronological development of the first digital computer, then the personal computers, modern-day portable computer devices, and ultimately the boom of information technology in just a few decades. The underlying increase in transistor count is best captured by the 1965 prediction by Gordon Moore which stated that in the following decades the number of components on an integrated circuit will approximately double every two years.[5] Known as "Moore's law", this empirical observation and prediction has served as a road-map for semiconductor technology for more than 40 years. During this period the scaling down has resulted both in more and *better* transistors with every next generation.

However, as the physical length of the transistor channel approaches the 10 nm range, Si technology is projected to reach its fundamental scaling limits within the

next 10-20 years.[6] 2016 marked the the first year in which the semiconductor industry announced that it will not be able to keep up with Moore’s law.[7] Future rapid improvements in computational performance, like the ones observed in the past decades, can not be taken for granted in the time ahead. Scientists have already started exploring new computation paradigms and the future could hold anything from molecular electronics [8], through biological- to quantum-computing [9, 10]. Whatever the exact computation paradigm, new materials are likely to play a key role and we might soon see a transition away from the “Silicon age”.

One of the most important developments in material science from the 21st century is the discovery of a new two-dimensional (2D) crystal, called graphene, which in 2010 was recognized with the Nobel Prize in Physics.[11] Graphene is a single sheet of perfectly-ordered carbon atoms, a million times thinner than a hair, and yet possessing considerable mechanical strength and electrical conductance.[12] Since this discovery, research has expanded towards the study of a plethora of atomically-thin 2D materials, which could play a pivotal role in enabling next-generation applications. Just like graphene can be considered as a single-layer equivalent of graphite, all well-studied 2D materials so far have a three-dimensional analogue which consists of a weakly-bonded stack of individual sheets.

In this thesis I present experimental results on the isolation of a new 2D material consisting of phosphorus atoms. This material is now called phosphorene and is obtained by exfoliation (thinning down) of bulk black phosphorus (bP), which is a crystalline form of elemental phosphorus. Together with Refs.[13, 14, 15, 16], the results in this thesis constitute some of the earliest electrical characterizations of ultrathin bP and experiments on the crystal’s environmental instability, surface passivation, and functionalization.

The thesis is organized as follows. In Chapter 2 I review some basic concepts

which aim to provide a basis for understanding the experimental results. In particular, section 2.1 reviews the the properties of 2D materials; section 2.2 explains the operating principle of field-effect devices based on 2D materials; and section 2.3 summarizes the known properties of bulk bP.

In Chapter 3 I explain the experimental methods employed in the thesis, aiming to provide sufficient details for replicating the experiments. I give details on the sample preparation, characterization, device fabrication, and electrical measurements.

Chapter 4 constitutes the main part of the thesis and is where the findings of the research are presented. In particular, section 4.1 shows electrical transport characterization of bulk bP; section 4.2 summarizes the earliest studies on exfoliation and electrical measurements of ultrathin bP; section 4.3 reports on the characterization of ultrathin bP passivated with graphene and hBN; section 4.4 shows the electrical transport of ultrathin bP on hBN and a study aimed at understanding the mobility limit in the samples; and section 4.5 shows results on the controlled doping of ultrathin bP using metal adatoms.

Chapter 5 provides a discussion of the experimental findings. In particular, in section 5.1 I compare the research findings of this thesis to recent results from the literature. Section 5.2 summarizes the distinctive properties of ultrathin bP; and section 5.3 aims to provide an outlook of the outstanding research challenges. The main results of the thesis are summarized once again in the conclusion, Chapter 6.

Chapter 2

Review of Basic Concepts

In this chapter I give a literature review which forms the basis and starting point for the research presented in the results chapter. In section 2.1 I give a broad review of the properties of two-dimensional materials and, in particular, of graphene, monolayer transition-metal dichalcogenides, and hBN. In section 2.2 I review the operating principle of field-effect transistors based on 2D materials. In section 2.3 I review the properties of bulk black phosphorus, which is the starting material for the exfoliation of 2D phosphorene.

2.1 Two-Dimensional Materials

The first isolation and characterization of monolayer graphene by Novoselov et al. in 2004 [17] has resulted in constantly expanding research on two-dimensional (2D) materials, which is turning into a separate subdomain of condensed matter physics. Under 2D materials we will understand *crystalline* solids which are only a single or few atoms thick, but have large lateral surface dimensions with long-range in-plane

order.¹ In order to be thermodynamically stable, the atoms of 2D materials form strong in-plane bonds and smooth layers without any out-of-plane dangling bonds. [18] In practice, all well-studied 2D materials to date are single-layer equivalents of a previously known highly-anisotropic three-dimensional (3D) layered crystal, where the individual layers are kept together by weak van der Waals forces. [18]

2D materials exhibit an intriguing combination of properties which can be seen to arise from the marriage of *high crystallinity* with *atomic thinness*. The high crystallinity ensures that 2D materials pertain excellent transport properties, for example in charge-, heat-, and spin-transport, and also allows them to exhibit considerable mechanical tensile strength, and near-perfect gas impermeability. On the other hand, the atomic thinness adds a plethora of additional properties that are normally not associated with crystalline solids, such as: optical transparency, mechanical flexibility, and 2D carrier confinement. This unique combination of properties arising from crystallinity and atomic thinness makes 2D materials a fascinating research playground for fundamental and applied science.

2.1.1 Graphene

Graphene was the first 2D crystal to be isolated and characterized and is arguably still the most important among the 2D materials. In the search for new 2D crystals it is important to review the novelty and excitement that came with the discovery of graphene, and that eventually led to the 2010 Nobel Prize in Physics.

Graphene is a single sheet of sp²-bonded carbon atoms ordered into a hexagonal 2D crystal lattice, as shown in Figure 2.1.1(a). The band diagram can be calculated analytically in the tight-binding approximation with nearest neighbor interactions.[19] The analytical result is

¹Throughout the text the terms “2D crystals” and “2D materials” will be used interchangeably.

$$E(\mathbf{k}) = \pm\gamma\left(1 + 4\cos^2\left(\frac{4k_y a}{2}\right) + 4\cos\left(\frac{4k_y a}{2}\right)\cos\left(\frac{\sqrt{3}k_x a}{2}\right)\right)^{1/2}$$

where $\gamma=2.8\text{eV}$ is the nearest-neighbor hopping energy, and $a = 0.246$ nm is the lattice constant. The theoretical Fermi level E_F at zero temperature is exactly at the Dirac point and a Taylor expansion for small momenta around $\mathbf{K} = (\frac{2\pi}{3a}, \pm\frac{2\pi}{3\sqrt{3}a})$ leads to a linear dispersion relation $E(\mathbf{q}) \approx v_F|\vec{q}|$ for $\mathbf{k} = \mathbf{K} + \mathbf{q}$, $q \ll K$, with a resulting zero effective mass with $v_F \approx 10^6$ m/s. A plot of the full band structure is shown in Figure 2.1.1(b).

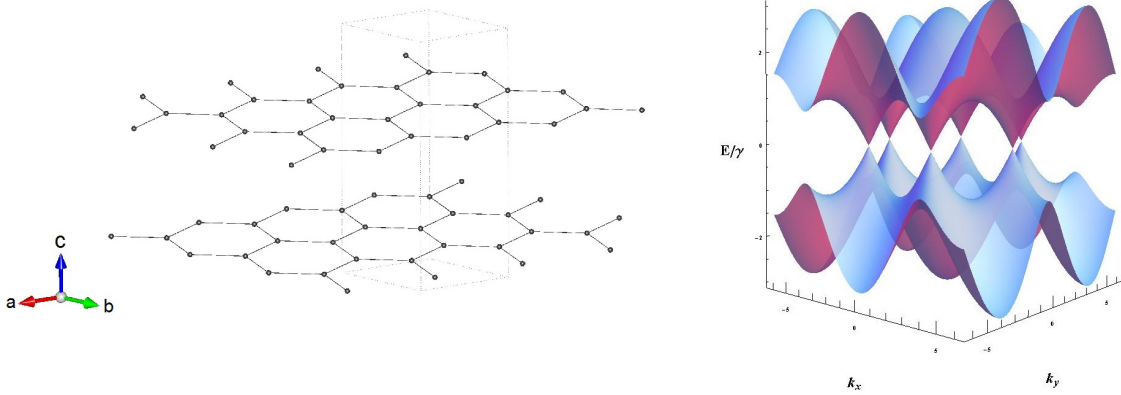


Figure 2.1.1: **(a)** Crystal structure of two layers of graphene. The C-C bond length is about 0.142 nm and the separation between the layers 0.33 nm. The ball size represents the C atom's van der Waals radius of around 0.017 nm. The image was generated by the VESTA structural model visualization software.[20] **(b)** Band structure of graphene.

Experimentally small pieces of mono- and few-layer graphene had been observed experimentally since the 1960s, and even grown by chemical vapor deposition (CVD) as early as 1995.[21] However, the enormous potential of the 2D material was not realized until the seminal paper by Novoselov et al. in 2004.[17] Here I highlight the main physical properties that have made graphene an important and far-reaching discovery.

(1) Monolayer graphene sheets were found to be surprisingly crystalline. Single-crystalline samples larger than $100 \mu\text{m}^2$ can be exfoliated easily and now even wafer-scale single crystals can be grown on a Ge substrate.[22] The excellent long-range order was surprising because it is known that fluctuational displacements diverge in infinitely large and free-standing 2D systems.[23]

(2) Despite its atomic thinness graphene exhibits excellent electronic quality, best highlighted by room temperature mobility of around $10^4 \text{cm}^2 \text{V}^{-1} \text{s}^{-1}$ in the first reported samples. This value is close to the high mobility found in GaAs/AlGaAs 2D degenerate gases (2DEG), which are much more complicated and technical to fabricate. On a hBN substrate the carrier mobility of graphene can reach $10^6 \text{cm}^2 \text{V}^{-1} \text{s}^{-1}$ [24], which is comparable to the values measured in bulk graphite single crystals.[25] Thus, despite the ultimately reduced thickness, graphene does not lose its excellent electronic quality and transport properties.

(3) The Fermi level, E_F , of intrinsic clean graphene is at the Dirac point, in an interval with low density of states (DOS).[19] This allows the electrostatic modulation of E_F over a wide energy range ($\pm 0.3 \text{eV}$) using a relatively simple Si/SiO₂ back gate. [26]

(4) The band structure of monolayer graphene is distinctively different from that of bulk graphite or even bilayer graphene.[19] The linear dispersion relation leads to low-energy excitations which obey the relativistic Dirac equation and enables the study of counter-intuitive relativistic phenomena, like Klein tunneling.[19]

(5) The thickness of an atomic carbon sheet is much smaller than the penetration depth of visible light into bulk graphite, which results in high optical transparency of mono- and few-layer graphene, even if light absorption relative to the material thickness remains high.[27]

(6) The atomic thinness of graphene allows high mechanical flexibility, while the

absence of bulk defects, like dislocations, results in extremely high mechanical tensile strength in single-crystalline samples.[28]

(7) Graphene is composed entirely of carbon - an abundant and inexpensive element. This allows the growth of high-quality electronic samples from abundant gases, like methane.[29]²

The combination of all these properties in a single material has made graphene, and 2D crystals in general, an exciting field of research.[12] From the point of basic science, the significant contribution of graphene has been in the possibility to study pure high-mobility 2D electronic systems and measure effects like: Klein tunneling[30], new topological states (anomalous integer quantum Hall states and fractional quantum Hall states)[31], Coulomb drag effect[32], valley polarized carrier transport[33], and others. From an applied science perspective the promises of graphene are even more; for example in transparent conductors, flexible electronics, high-frequency transistors, gas separation membranes, and many more.[12]

2.1.2 Monolayer Transition Metal Dichalcogenides

Despite graphene's huge technological potential it was realized that the absence of a band gap and a true insulating state pose significant limitations to its use as an active electronic material.[34] Graphene is a semi-metal, not a semiconductor which, limits its usefulness in active components such as transistors, diodes, and photocells. Therefore, researchers started looking for new *semiconducting* 2D materials which led to intense research on monolayer transition metal dichalcogenides (TMDC), and especially on MoS₂ and WS₂. [35, 36, 37]

²Much like in Si electronics, where the starting material for wafer growth is sand.

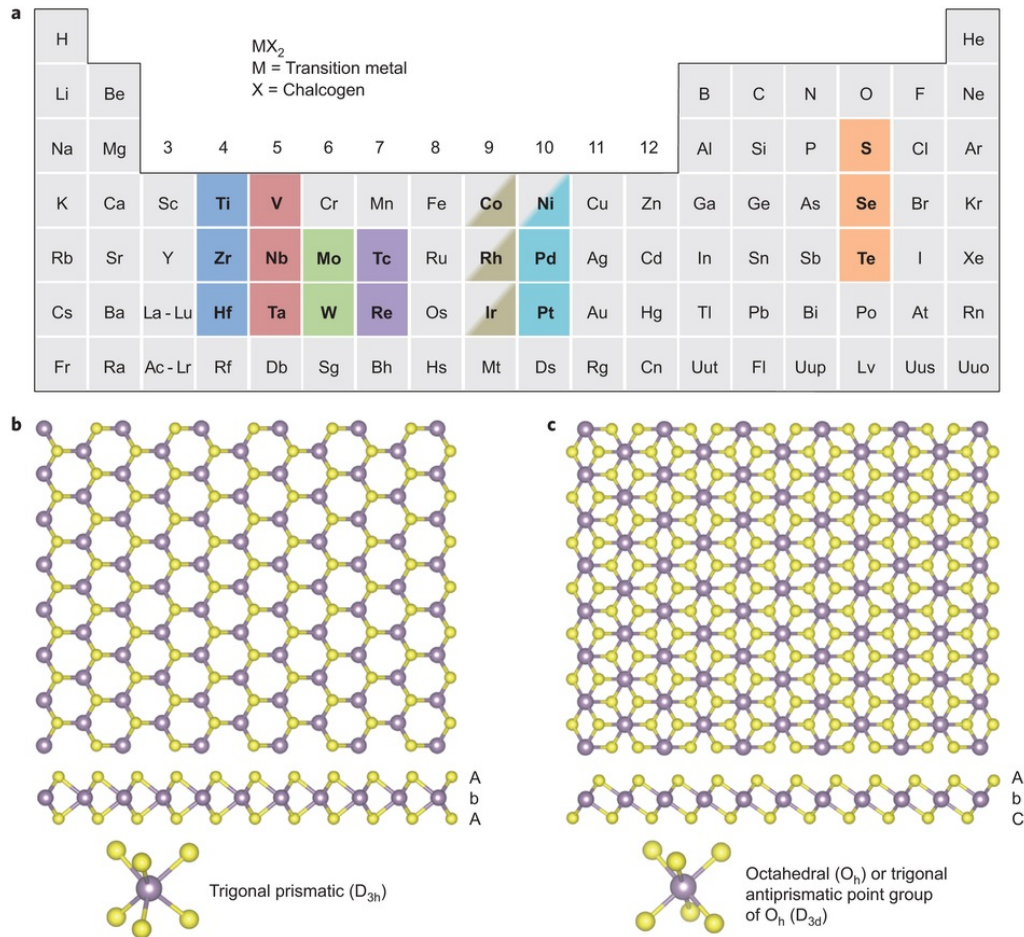


Figure 2.1.2: **(a)** About 40 different layered TMDC compounds exist. The transition metals and the three chalcogen elements that predominantly crystallize in those layered structure are highlighted in the periodic table. Partial highlights for Co, Rh, Ir and Ni indicate that only some of the dichalcogenides form layered structures. **c**-axis and section view of single-layer TMDCs with trigonal prismatic **(b)** and octahedral **(c)** coordinations. Atom color code: purple, metal; yellow, chalcogen. The labels AbA and AbC represent the stacking sequence where the upper- and lower-case letters represent chalcogen and metal elements, respectively. Adapted by permission from Macmillan Publishers Ltd: Nature Chemistry [38], copyright 2013.

TMDCs have the general formula MX_2 , where M is a transition metal and X is a chalcogen atom (S, Se, or Te). A single TMDC sheet consists of three atomic layers X-M-X, as shown in Figure 2.1.2, and has a monolayer thickness of 7 to 8 Å.[38, 39] The coordination geometry of the X atoms around the transition metal can be either

trigonal prismatic (known as $\text{MX}_2\text{-2H}$), or octahedral ($\text{MX}_2\text{-T}$). The electronic character of the material is mainly determined by the number of non-bonding d electrons of the transition metal atom.[38] Group 4, 6, and 10 transition metal atoms form semiconducting materials, while the group 5 and 7 elements form metallic crystals. This can be seen by the progressive filling of the d orbitals, as illustrated in the schematic of Figure 2.1.3. The large number of possible M-X combinations makes TMDCs the largest 2D materials family. Furthermore, the presence of both semiconducting and metallic compounds has widened the research scope. The semiconducting TMDCs are being studied with a clear prospect of technological applications, while recently the metallic crystals have attracted attention in basic research because at low temperatures they often exhibit of highly-correlated phases like superconductivity and charge density wave (CDW) order.[40]

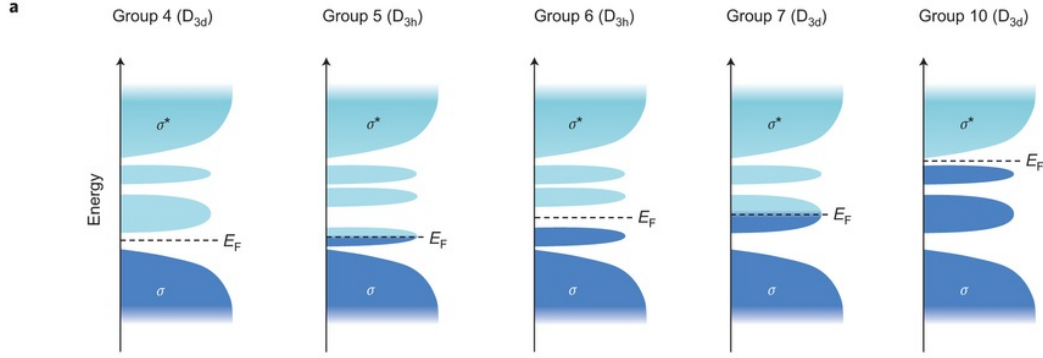


Figure 2.1.3: Qualitative schematic illustration showing progressive filling of d orbitals that are located within the band gap of bonding (σ) and anti-bonding states (σ^*) in group 4, 5, 6, 7 and 10 TMDCs. D_{3h} and D_{3d} refer to the point group associated with the trigonal prismatic and the octahedral coordination of the transition metals. It should be noted that this simple model assumes ideal coordination; structural distortion often seen in many tellurides and group 7 TMDCs lead to deviation in the electronic structure. The filled and unfilled states are shaded with dark and light blue, respectively. According to ligand field theory, D_{3d} compounds form two non-bonding d orbitals, $d_{yz,xz,xy}$ (bottom) and d_{z^2, x^2-y^2} (top), while D_{3h} (or O_h) compounds exhibit three d orbitals whose character is predominantly d_{z^2} , dx^2-y^2, xy , and $d_{xz,yz}$ (from bottom to top). When an orbital is partially filled (such as in the case of group 5 and 7 TMDs), the Fermi level (E_F) is within the band and the compound exhibits a metallic character. When an orbital is fully filled (such as in group 6 TMDs), the Fermi level is in the energy gap and a semiconducting character is observed. Adapted by permission from Macmillan Publishers Ltd: Nature Chemistry [38] copyright 2013.

Currently MoS_2 and WS_2 are the most well-studied semiconducting TMDCs.[41] Both crystals exhibits the trigonal prismatic (2H) coordination geometry and the respective bulk van der Waals crystals have a band gap of 1.2 eV and 1.3 eV. Upon reducing the number of layers the band gap starts to increase due to quantum confinement effects, and the monolayer band gap is 1.9 eV for MoS_2 and 2.1 eV for WS_2 . [36] A further important change in the band structure is the fact that the monolayers exhibit a direct band gap at the K point.[36] This transition from an indirect to direct band gap is associated with the disappearance of interlayer interactions in the monolayer crystals.[42]. For both materials the carrier mobility at room temperature

is on the order a $100 \text{ cm}^2\text{V}^{-1}\text{s}^{-1}$ [41]. The large band gap allows the fabrication of MoS_2 transistors with on-off current ratio as high as 10^8 which holds promise for application in next-generation low-power electronics.[41]

2.1.3 Hexagonal BN and Other 2D Materials

Besides graphene and TMDCs there is a plethora of other 2D materials which have been isolated and characterized to some extent. Figure 2.1.4 provides a summary of the known families of 2D crystals before the discovery of ultrathin bP. Of particular importance for this thesis is hexagonal BN (hBN). It is the most stable form of BN forming a hexagonal lattice with point group D_{6h} and space group $P6_3/mmc$, similar to graphite.[43] hBN is considered an insulator with a band gap of more than 5 eV in bulk and around 6 eV in the monolayer form. The crystal is remarkably stable with a decomposition temperature of up to 1000 °C in air.[43] The main application of exfoliated hBN in the field of 2D materials research is to serve as a smooth insulating substrate for 2D conducting crystals, or to form a gate dielectric for field-effect devices.[24, 44, 45]

Graphene family	Graphene	hBN 'white graphene'	BCN	Fluorographene	Graphene oxide
2D chalcogenides	MoS ₂ , WS ₂ , MoSe ₂ , WSe ₂		Semiconducting dichalcogenides: MoTe ₂ , WTe ₂ , ZrS ₂ , ZrSe ₂ and so on	Metallic dichalcogenides: NbSe ₂ , NbS ₂ , TaS ₂ , TiS ₂ , NiSe ₂ and so on	
				Layered semiconductors: GaSe, GaTe, InSe, Bi ₂ Se ₃ and so on	
2D oxides	Micas, BSCCO	MoO ₃ , WO ₃	Perovskite-type: LaNb ₂ O ₇ , (Ca,Sr) ₂ Nb ₃ O ₁₀ , Bi ₄ Ti ₃ O ₁₂ , Ca ₂ Ta ₂ TiO ₁₀ and so on	Hydroxides: Ni(OH) ₂ , Eu(OH) ₂ and so on	
	Layered Cu oxides	TiO ₂ , MnO ₂ , V ₂ O ₅ , TaO ₃ , RuO ₂ and so on		Others	

Figure 2.1.4: Known families of 2D materials. Monolayers proved to be stable under ambient conditions (room temperature in air) are shaded blue; those probably stable in air are shaded green; and those unstable in air but that may be stable in inert atmosphere are shaded pink. Grey shading indicates 3D compounds that have been successfully exfoliated down to monolayers, as is clear from atomic force microscopy, for example, but for which there is little further information. ‘Others’ indicates that many other 2D crystals—including borides, carbides, nitrides and so on—have probably been or can be isolated. BCN, boron carbon nitride. Reprinted by permission from Macmillan Publishers Ltd: Nature, advance online publication, [18] (doi: 10.1038/sj.nature12385).

As a smooth substrate, exfoliated hBN crystals of 20-30 nm thickness exhibit a surface roughness of around 0.1 nm, which is up to three times less than the roughness of prime grade Si/SiO₂ wafers.[24, 44] Additionally, hBN forms a flat surface with no dangling bonds and has a less reactive surface termination than SiO₂. Therefore, graphene transferred on an hBN crystal exhibits 10 to 100 times higher carrier mobility, than on SiO₂. [24, 44] This makes hBN an important 2D material for fabricating heterostructures with high electronic quality.

hBN can also serve as a good gate dielectric because it exhibits a static relative permittivity (dielectric constant), ϵ_r , of around 4-5, which is larger than the value found for SiO₂ ($\epsilon_r=3.9$). At the same time, hBN exhibits a dielectric strength (dielectric breakdown voltage) of around 12 MV/cm, which is similar to that of SiO₂. [46] In the results section 4.4 we will compare the transport properties of few-layer phos-

phorene on SiO₂ and hBN, and in section 4.5 a 30 nm thick hBN crystal will be used as a gate dielectric for a ultrathin bP field-effect device.

Further 2D materials, besides graphene, TMDC monolayers, and hBN, that have been reported in mono- or few-layer form include some mica silicates and perovskites, see Figure [18]. However, these have not yet been studied in depth and will not be important for this work.

2.1.4 Van der Waals heterostructures

A natural continuation of the expanding research on 2D crystals is the idea to isolate monolayers of different materials and stack them together to form a heterostructure.[18] By appropriately choosing the constituent layers of these heterostructures one could tailor the physical properties and build new materials which are not present in nature. Importantly, the physical and chemical properties of the individual atomic layers could be chosen so different from one another, that the structures would be impossible to fabricate using standard crystal growth or deposition techniques.

In this work we will study the electrical transport properties of several ultrathin bP heterostructures. In section 4.3 we demonstrate the chemical passivation of ultrathin bP by covering it with graphene or hBN. Then, in section 4.4 we will transfer ultrathin bP onto a hBN crystal and measure how the substrate affects the electrical transport properties. In section 4.5 we fabricate a graphene/hBN/ultrathin bP heterostructure which will be used for selective channel doping and the fabrication of a voltage inverter. The dry transfer method for stacking 2D crystals and fabricating heterostructures is described in section 3.2.

2.2 Field-Effect Transistors Based on 2D Materials

The major goal of the performed experiments is to understand the charge transport properties of ultrathin bP and to study the material's capabilities in proof-of-principle electronic devices. All studies in the results sections include electrical characterization of ultrathin bP field-effect devices. In this section I summarize my understanding of the operation of field-effect devices based on 2D materials. To the best of my knowledge, to date there is no concise (textbook-like) description of the operating principle of transistors based on 2D materials, and different researchers concentrate in their explanations on different aspects of the operation (such as carrier-injection, band-bending, Schottky barrier modulation, etc). The subject is sometimes additionally convoluted by the use of analogies to bulk semiconductor devices (like inversion mode, surface potential, threshold voltage, etc.), which are not always directly applicable to 2D materials. The following exposition aims to provide a coherent picture of the operation 2D-materials-based FET devices.

2.2.1 The Capacitor Model and On-State Operation

Field-effect devices based on 2D crystals are, by definition, a stack consisting of: a conductor, a dielectric, a 2D semiconductor, and another dielectric. The conductor could be either below the bottom dielectric (in which case it is called a back gate), or above the top dielectric (a top gate). If there is a back gate, the top insulator is often only air or vacuum. The simplest geometry is a 2D semiconductor exfoliated onto a Si/SiO₂ wafer. In this case the bottom conductor is the Si (which is heavily doped and conducting, although this is not always explicitly mentioned), the bottom dielectric is the SiO₂, and the top dielectric is air or vacuum.³

³The arrangement of the materials is already different than the standard bulk FET technology, which consist of: a bulk semiconductor, a dielectric, and a top conductor. There are bulk semi-

In order to operate as a transistor, two electrodes are fabricated directly onto the 2D semiconductor channel, which are usually referred to as the source and drain electrodes. Figure 2.2.1(a) shows a schematic of typical device utilizing an MoS₂ monolayer sandwiched between Si/SiO₂ and HfO₂/Au (in this case there is both a top and a back gate).

The operation of the device in the on-state and when the contact resistance is not dominating the transport, can be understood within a simple parallel-plate capacitor model. The 2D semiconductor channel consists of a single surface with negligible extrinsic doping, low intrinsic carrier density, and overall low atom density. As such there is no semiconductor “bulk” to contribute to the device operation, so there is no surface potential and the situation is simpler than in bulk Si field effect transistors (FETs). Applying a voltage between the gate conductor and the 2D material (across the dielectric) can be understood in a simple parallel-plate-capacitor model. The gate conductor serves a one of the capacitor electrodes, and the 2D semiconductor as the other one. Applying a positive voltage, V_g , on the gate conductor results in the accumulation of a charge $+Q$ on the gate conductor and $-Q$ in the 2D semiconductor. The charge Q is proportional to V_g by $Q = CV_g$, where C is the fixed capacitance of the device. For a parallel-plate capacitor we have the simple relation $C = \frac{\epsilon A}{d}$, where A is the area, $\epsilon = \epsilon_0 \epsilon_r$ is the permittivity, and d is the thickness of the dielectric. If we convert this to an areal number density we obtain the simple yet important relation:

$$n = \frac{Q}{eA} = \frac{\epsilon}{ed} V_g$$

where e is the absolute value of the electron charge. Since a positive voltage on the conductor technologies which employ a thin slab of semiconductor placed between two insulators, known as “silicon-on-insulator”. It employs a “buried” oxide in the bulk substrate, also known as “BOX”. The operation of “silicon-on-insulator” devices resembles the operation of FETs based on 2D materials.

gate conductor results in a charge $-Q$ in the 2D crystal, applying positive V_g accumulates electrons in the semiconductor and a negative V_g accumulates holes (depletes electrons). For example, in the case of a SiO_2 dielectric with 300 nm thickness, the typical voltage that can be applied is $-100 \text{ V} < V_g < +100 \text{ V}$. Plugging in $d=300 \text{ nm}$, $V_g=\pm 100 \text{ V}$, and the permittivity of SiO_2 , results in $n = \mp 7.184 \times 10^{12} \text{ cm}^{-2}$ electrons (holes) accumulated in the 2D semiconductor. This number is important because it gives a guide to whether a large field effect can be observed in a given crystal using a solid-state gate. If the intrinsic carrier density of the 2D material is much lower than 10^{12} cm^{-2} , the charge accumulated by the gate will constitute the dominant fraction of carriers in the crystal. For example, in graphene the intrinsic carrier density is in the order of $10^9 - 10^{10} \text{ cm}^{-2}$ so the conductance can easily be controlled by the electric field. If instead we consider a thin Au film, with a typical carrier density on the order of 10^{14} cm^{-2} , the charge accumulation by the gate will still be present, but it will be changing less than 1% of the film's carrier density and the effect will be negligible.

The parallel-plate capacitor model for the amount of carriers induced by the electric field in a 2D material has been validated experimentally. Figures 2.2.1(b)&(c) show the carrier density of monolayer MoS_2 and ultrathin bP measured by the Hall effect at different gate voltages. In both cases the observed linear dependence of the carrier density with gate voltage in the on-state can be fitted to the parallel-plate model (a straight line) with an additional small carrier density n_0 , i.e. a finite constant shift V_g . Given the carrier density, the conductivity, σ , in the on-state of the device is simply determined by the channel's mobility, μ , by $\sigma = ne\mu$.

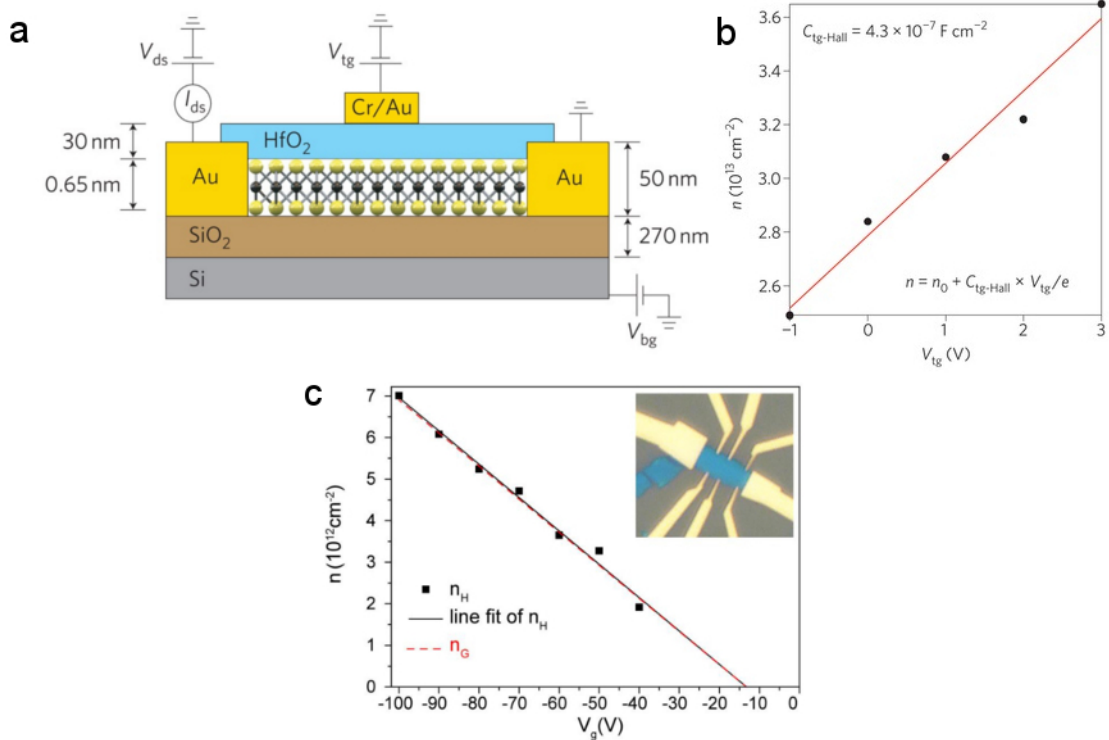


Figure 2.2.1: **(a)** Cross-sectional view of the structure of a monolayer MoS₂ FET together with electrical connections used to characterize the device. A single layer of MoS₂ (thickness, 6.5 Å) is deposited on a degenerately doped silicon substrate with 270-nm-thick SiO₂. The substrate acts a back gate. One of the gold electrodes acts as drain and the other source electrode is grounded. The monolayer is separated from the top gate by 30 nm of HfO₂ grown by atomic layer deposition. Adapted by permission from Macmillan Publishers Ltd: Nature Nanotechnology [35], copyright 2011. **(b)** Charge-carrier concentration, n , extracted from Hall resistance R_{xy} and its dependence on the applied V_{tg} . The linear fit allows the top-gate capacitance, $C_{tg-Hall}$, to be extracted. n_0 , residual doping level; e , electron charge. Adapted by permission from Macmillan Publishers Ltd: Nature Nanotechnology [47], copyright 2013. **(c)** Measured carrier density n_H n as a function of gate voltage (black squares) for the device pictured in the inset . Two opposing contacts in the middle are used to measure the Hall coefficient. The black solid line is a linear fit of the data. They agree well with the calculated n_G shown as the red dashed line . Adapted by permission from Macmillan Publishers Ltd: Nature Nanotechnology [13], copyright 2014.

2.2.2 Schottky Barrier Height and Sub-Threshold Operation

The capacitor model for determining the on-state carrier density and conductivity does not apply in the sub-threshold V_g region (off-state) of the device. This is seen from the need to introduce a small constant offset, n_0 , around $V_g = 0$ and, most importantly, from the fact that the source-drain current in the off-state (in semiconducting 2D materials) does not depend linearly on V_g . In this region the conductance is determined by the transmission through the source and drain electrodes, which requires analyzing the Schottky barrier between the metal (the source/drain electrode) and the 2D semiconductor.

Bringing a metal into contact with a semiconductor unavoidably leads to some charge redistribution at the interface and to the formation of a finite potential-energy barrier that can affect the carrier flow. In the simplest picture, the Schottky-Mott rule states that the energy barrier, Φ_B , is determined by the band-bending at the interface, i.e. by the difference between the work function of the metal, W_M , (relative to vacuum) and the electron affinity (or vacuum ionization energy) of the semiconductor, χ_S , $\Phi_B \approx W_M - \chi_S$. [48] Depending on the height and spatial width of the Schottky barrier, the interface could exhibit non-linear I-V characteristics. The presence of chargeable gap states, arising from either the interface or the semiconductor surface, can additionally complicate the description. In this case the charge redistribution will fill the interfacial states and the Fermi level will necessarily align to their energy (independent of W_M), leading to so called “Fermi level pinning”. [48]

A relatively simple and intuitive model to describe the off-state of ultrathin-body devices was recently proposed by Penumatcha, Salazar, and Appenzeller in Ref. [49]. The Fermi level at the metal-semiconductor interface is assumed to be pinned somewhere in the gap, leading to two constant barrier heights for electron and hole in-

jection, $\Phi^{(n)}_{\text{B}}$ and $\Phi^{(p)}_{\text{B}}$. The sum of the two barrier heights gives the band gap energy $E_{\text{gap}} = \Phi^{(n)}_{\text{B}} + \Phi^{(p)}_{\text{B}}$. The electrostatics of the device is controlled by a body-thickness parameter, $\alpha = \sqrt{\frac{\epsilon_{\text{S}}}{\epsilon_{\text{ox}}} t_{\text{S}} t_{\text{ox}}}$, where ϵ_{S} , ϵ_{ox} denote the permittivity, and t_{S} , t_{ox} denote the thickness of the semiconductor and the gate oxide, respectively. a determines the lateral spatial width of the Schottky barrier. The effect of the gate voltage, V_{g} , is to change the position of the valence and conduction band edges, E_{V} and E_{C} , relative to the pinned Fermi level under the contacts. The drain-source voltage, V_{sd} , offsets the Fermi level of one of the two contacts to $E_{\text{F}} - eV_{\text{sd}}$. A schematic of the model and the important parameters is shown in Figure 2.2.2(a). The gate-dependent source-drain current through the device per unit width is then calculated using

$$I_{\text{sd}} = \frac{2e}{h} \int_{-\infty}^{E_{\text{V}}} T(E) M_{\text{V}}(E) [f(E) - f(E - eV_{\text{sd}})] dE$$

where $M_{\text{V}} = \frac{g}{\pi\hbar} \sqrt{2m_{\text{h}}(E_{\text{V}}(V_{\text{g}}) - E)}$, $E_{\text{V}} > E$, represents the number of modes per unit width, and h is the Planck constant. Here g is the valley degeneracy, m_{h} is the effective mass, $f(\cdot)$ is the Fermi-Dirac distribution, and $T(E)$ is the energy-dependent transmission through the barrier. Performing the integral requires an assumption for the barrier shape which in [49] is taken as being triangular with a base length a . The transmission through the barrier can then be calculated in the Wentzel-Kramers-Brillouin (WKB) approximation, $T(E) = \exp\left(-\int_0^{x_0} \kappa(E) dx\right)$, with $\kappa(E) = \hbar^{-1} \sqrt{2m_{\text{h}}(E - E_{\text{V}}(x))}$. Here x_0 is the length within the gate-controlled channel at which $E = E_{\text{V}}$, see Figure 2.2.2(a).

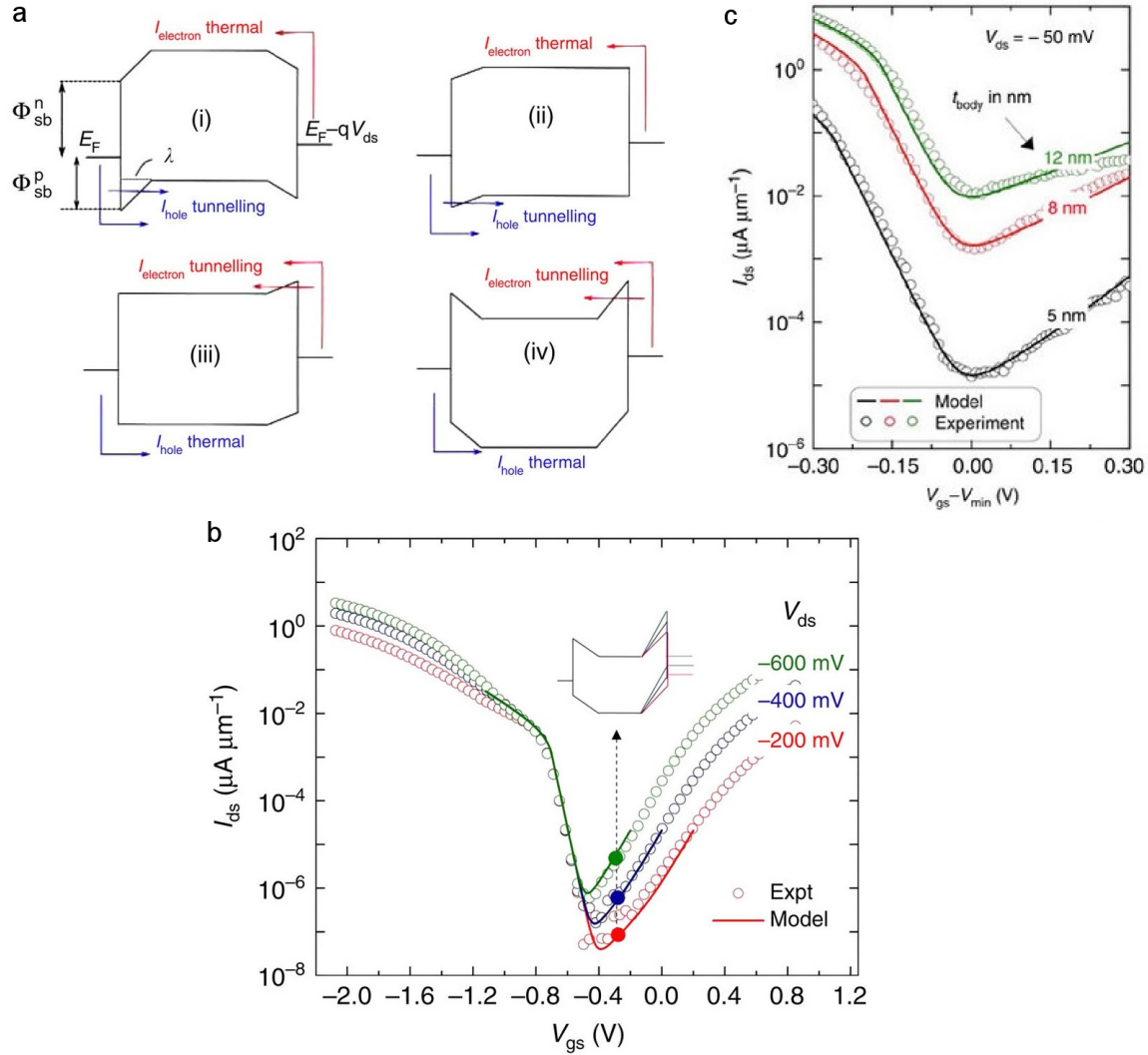


Figure 2.2.2: **(a)** Schematic illustrating the parameters ($\Phi_B^{(n)}$, $\Phi_B^{(p)}$, E_F , V_{ds} , and α) of the subthreshold model. **(b)** Transfer characteristic of a silicon Schottky barrier FET with $L_{ch}=2\mu m$, $t_{ox}=3$ nm and $t_{Si}=25$ nm. Experimental data are plotted in red, blue and green open circles. The fits to the different V_{ds} curves using the Schottky barrier FET model are plotted using solid lines of the corresponding color. The same $\Phi_B^{(n)}$ and $\Phi_B^{(p)}$ were used to fit all three $I_{ds}-V_g$ curves for different V_{ds} values. The inset shows the band bending situation for different V_{ds} -voltages at a fixed V_g . **(c)** Plots showing fits to the experimental data (open circles) using the Schottky-Barrier subthreshold model. The x axis of the experimental $I_{ds}-V_{gs}$ data has been re-scaled to account for the effect of C_{it} (interface trap capacitance). Adapted from [49] under a Creative Commons “Attribution 4.0 International” license.

The model can predict I_{sd} versus V_g , provided that $\Phi_B^{(n)}$, $\Phi_B^{(p)}$, α , and V_{sd}

are specified. Alternatively, given a measured $I_{sd} - V_g$ curve with known a and V_{sd} (which are known design and measurement parameters), the model can be fitted to extract $\Phi_B^{(n)}$ and $\Phi_B^{(p)}$.

The discussed Schottky-barrier model for sub-threshold operation has been shown to give good agreement when tested against experimental $I_{sd} - V_g$ curves obtained from ultrathin-body Si transistors and few-layer black phosphorus devices, see Figure 2.2.2(a)&(b).[49] It gives an intuitive description of the factors determining the operation in this device regime. However, it also requires a shifting of the minimum conductance to $V_g = 0$ V, and does not account for shift in the threshold voltage by external doping, or gate-sweep hysteresis. To the best of my knowledge, there is still no unified model capable of describing both the on-state operation and sub-threshold region, and in addition, account for the channel’s doping, threshold voltage, and trap states.

2.3 Material Properties of Bulk Black Phosphorus

In this section I review the material properties of bulk black phosphorus (bP) which is the starting material for the exfoliation of few-layer phosphorene and the fabrication of field-effect devices. The review is loosely based on Ref.[50]. In order to avoid confusion with the chemical compound boron phosphide (BP), I adopt the notation bP throughout the text.

Black phosphorus is a crystalline allotrope of phosphorus. It is the most chemically stable form in ambient conditions of the group-15 element P, which is also found in the form of “white” and “red” phosphorus. White phosphorus is a soft, waxy substance which consists of P_4 molecules and ignites spontaneously at around 30^o C in air. If white phosphorus is heated with a catalyst in the absence of air to 300^o C, it turns

into a more stable form called red phosphorus, which consists of chains of P_4 -like molecules with one broken bond . The bonding angle of the P_4 molecule in white phosphorus is sharp, at 60° , which induces large strain and makes P_4 unstable. If the tetrahedron is allowed to “open” by breaking one of the 6 bonds, this allows re-bonding to a nearby P atom, which reduces the strain and makes red phosphorus less reactive and with a polymer-like structure. If white phosphorus is put at high pressure of 1.2 GPa at 200°C , or red phosphorus is put at high pressure of 3.8 GPa at 270°C , they form a crystalline solid known as bP.

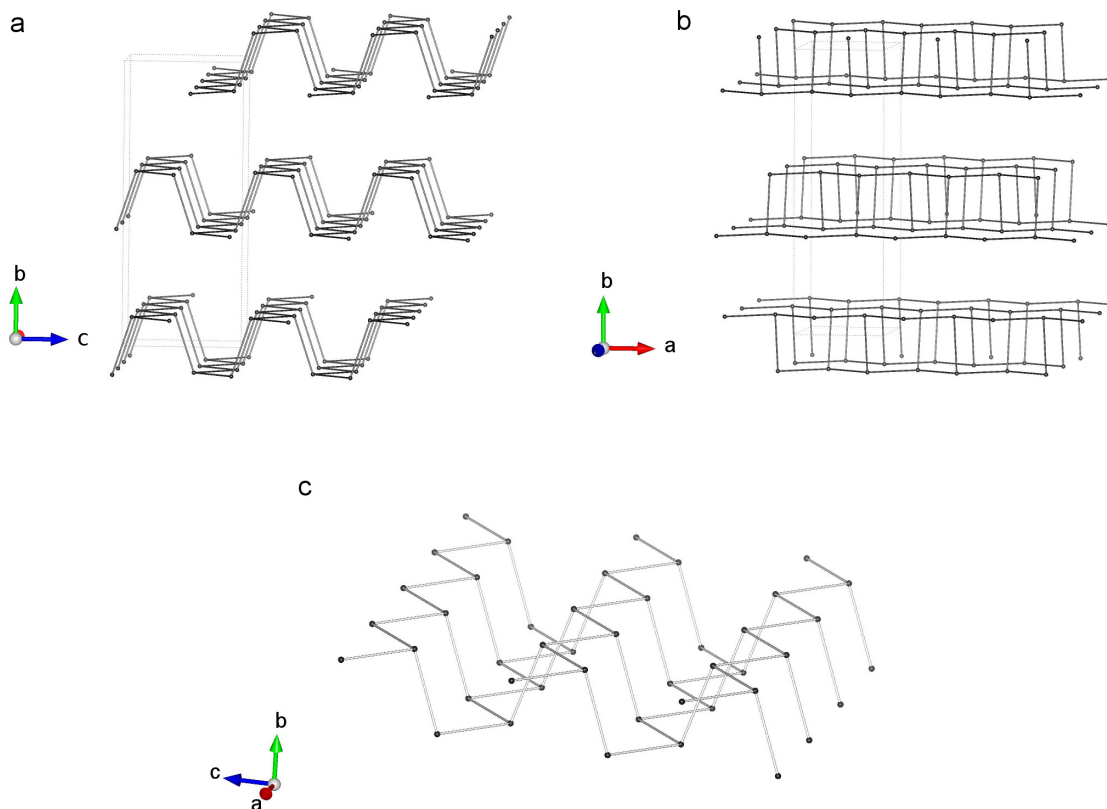


Figure 2.3.1: Lattice structure of bP from different perspectives. **(a)** Three-layers as seen from the c-b plane. **(b)** Three-layers as seen from the a-b plane. **(c)** A schematic of the monolayer. The ratio between all lengths is accurate. The size of the balls represents the van der Waals radius of the P atom at 190 pm. The image was generated using the VESTA software package.[20]

The crystal structure of bP is orthorhombic with a 64 C_{mca} space group and consists of “puckered” layers held together by weak van der Waals forces.[50] The lattice constants are $a=3.3136 \text{ \AA}$, $b=10.478 \text{ \AA}$, and $c=4.3763 \text{ \AA}$, with structural parameters P:(0.0, 0.10168, 0.08056). [50] The bond length is about 2.222 \AA for the nearest two atoms, and 2.277 \AA for the puckered vertical bond. A structural visualization of the lattice of bP is shown in Figure 2.3.1.

Elemental phosphorus is not found as bP in nature. The crystal was synthesized

for the first time in 1914 by P. W. Bridgman⁴ while studying white phosphorus at high pressure.[52] In 1982 Endo et al. succeeded for the first time in producing large, mm-sized bP crystals by transforming red phosphorus at high pressure.[53] This allowed a more detailed study of the material's electronic properties in the following years.

⁴In 1946 P. W. Bridgman was awarded the Nobel Prize in Physics *"for the invention of an apparatus to produce extremely high pressures, and for the discoveries he made therewith in the field of high pressure physics"*. [51]

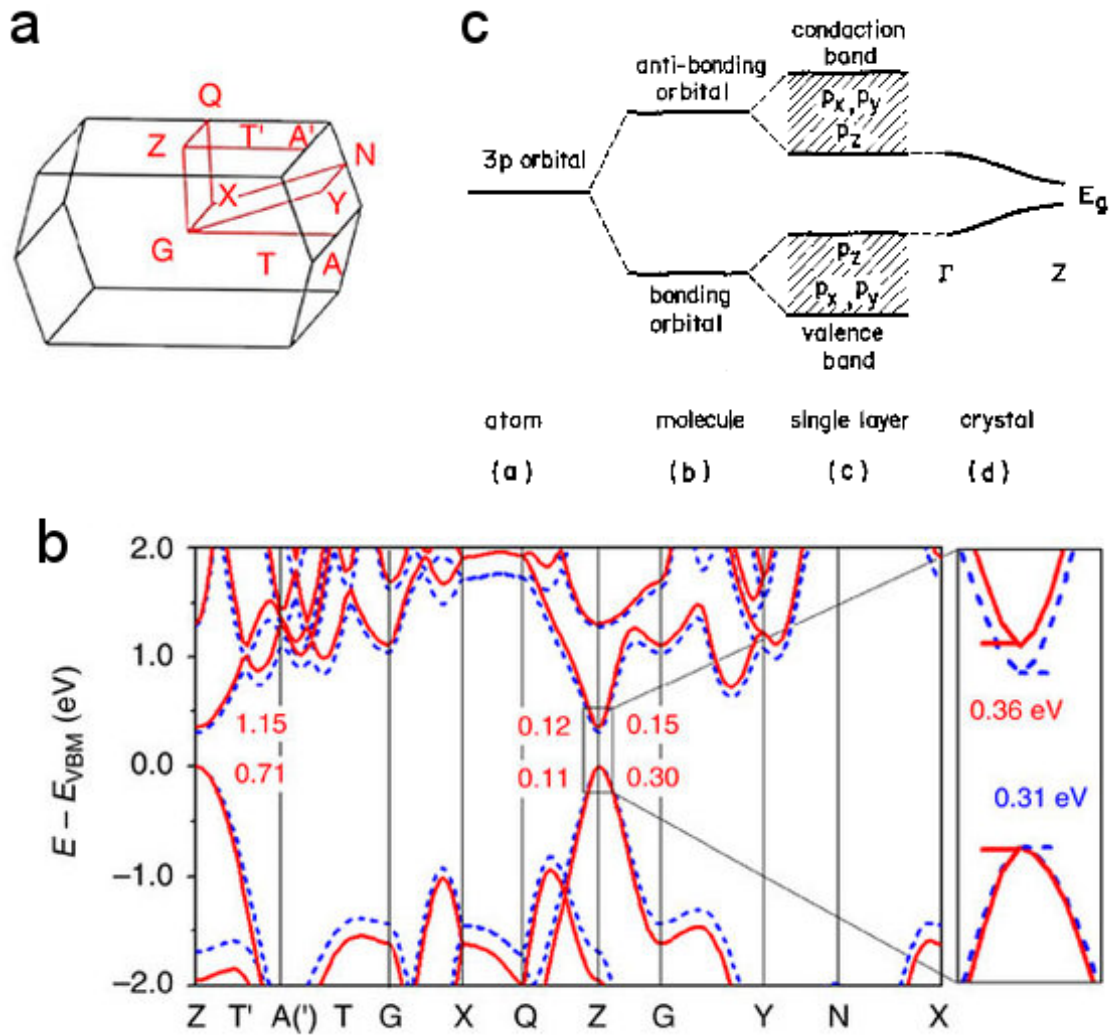


Figure 2.3.2: From left to to right: **(1)** Brillouin zone path of bP primitive cell. **(2)** Electronic band structures for bulk bP calculated with the HSE06 functional (red solid line) and the mBJ potential (blue dashed line), together with fitted effective masses along the Z-T'-A', Z-Q and Z-G directions. At the right of the image, a zoomed-in plot shows the direct band gap at Z. EVBM is the energy of valence-band maximum. Adapted from [54] under a Creative Commons "Attribution-NonCommercial" license. **(3)** Schematic energy-level diagrams of phosphorus 3p orbital in (a) atom, (b) molecule, (c) single puckered layer, and (d) black phosphorus. In the case of (d), the top of the valence band and the bottom of the conduction band along the line F-Z are shown. *Springer Applied Physics A*, "Semiconducting Black Phosphorus", 39, 1986, 227, A. Morita. With permission of Springer.

The band structure of bP, calculated by density functional theory (DFT), is shown

in Figure 2.3.2(1)&(2).[54] The material is a semiconductor with a direct band gap of about 0.3 eV at the Z point. The band structure can be understood as arising from the P atom’s outer-most 3p orbital, as illustrated in Figure 2.3.2(3). In a hypothetical P-P molecule the 3p orbital splits into a bonding and anti-bonding state. In a single bP layer the top part of the valence band and the bottom part of the conduction band form a direct band gap at Γ , which consists mainly of p_z -orbitals. In the bulk crystal inter-layer interactions cause an upward bend of the valence band and a downward dispersion of the conduction band along the Γ -Z direction which results in a decrease of the gap to 0.3 eV at the Z point of the bulk crystal, see Figure 2.3.2(3).[50]

The large in-plane anisotropy of the crystal (as seen in the puckered structure) results in large difference between the effective carrier masses along the three crystal directions. Experimental and theoretical values for the hole and electron effective mass are summarize in Table 2.1.[50] The effective mass is lowest along the arm-chair direction (across the puckered structure), and higher along the zig-zag direction (parallel to the puckered ridges). The heaviest mass is along the y direction, which corresponds to transport across the layers. The in-plane anisotropy is more significant for holes than for electrons.

Direction	Hole		Electron	
	Expt.	Calc.	Expt.	Calc.
m_x/m_0	0.076	0.09	0.0826	0.09
m_y/m_0	0.648	0.81	1.027	1.16
m_z/m_0	0.280	0.36	0.128	0.17

Table 2.1: Effective masses of carriers in black-P. *Springer Applied Physics A*, “Semiconducting Black Phosphorus”, 39, 1986, 227, A. Morita. With permission of Springer.

Charge transport measurements were first performed between 1953 and 1963 in poly-crystalline samples.[55, 56] It was found that all samples exhibited p-type conduction and a narrow band gap of 0.3 eV. In 1983 after the first growth of millimeter-

size single-crystals by Endo et al., the same group performed detailed transport measurements on single crystal bP.[57] The effective concentration of unintentional acceptors, (N_A-N_D) , was found to be in the region $2-5 \times 10^{15} \text{ cm}^{-3}$ but their origin remained unknown. The Hall mobility for holes was found to be around $1200 \text{ cm}^2\text{V}^{-1}\text{s}^{-1}$ and $500 \text{ cm}^2\text{V}^{-1}\text{s}^{-1}$ at 300 K for the armchair and zig-zag directions, respectively. The maximum mobility was found at low temperature, around 20 K, and was about $65\,000 \text{ cm}^2\text{V}^{-1}\text{s}^{-1}$ and $20\,000 \text{ cm}^2\text{V}^{-1}\text{s}^{-1}$ for the two directions. The decrease in mobility from 300 K to 20 K was found to follow a $\mu \propto T^{-3/2}$ behavior characteristic of phonon scattering in 3D.[58] N-types samples were also studied using Te doping with a donor concentration of $(N_D-N_A) = 2-3 \times 10^{16} \text{ cm}^{-3}$. The transport results of Ref.[57] are summarized in Table 2.2.

Direction	Hole			Electron		
	x	y	z	x	y	z
Hall mobility ($\text{cm}^2\text{V}^{-1}\text{s}^{-1}$) at 200 K	3000	1200	540	2300	460	400
Max. value $\times 10^{-3}$ ($\text{cm}^2\text{V}^{-1}\text{s}^{-1}$)	65	20	8.5	16	2.2	1.0
Activation energy of impurity	$\approx 18 \text{ meV}$			$\approx 20 \text{ meV}$		
Effective impurity concentration	$2-5 \times 10^{15} \text{ cm}^{-3}$			$2-3 \times 10^{16} \text{ cm}^{-3}$		
Energy gap E_g at room temp.	335 meV					

Table 2.2: Electrical properties of bP. *Springer Applied Physics A*, “Semiconducting Black Phosphorus”, 39, 1986, 227, A. Morita. With permission of Springer.

Electrical transport measurements on bulk bP are also performed as part of this thesis and the results are discussed in section 4.1.

Chapter 3

Experimental Methods

This section describes the experimental methods and equipment that were employed in the isolation of ultrathin bP, the fabrication of field-effect devices, and their characterization.

3.1 Micromechanical Exfoliation

Ultrathin crystals were exfoliated using low-adhesion tape produced by Nitto model “ELEP HOLDER BT-150E-CM”, which was chosen because it leaves the least glue residue. The starting material is bulk black phosphorus obtained from one of three sources, as specified in the particular results section. The first set of bulk crystals was purchased from “SmartElements” GmbH, with a producer-specified purity of 99.998% and synthesized by gas phase transport. A second source of bulk material was purchased from “HQ graphene” which was produced using a high-pressure and high-temperature conversion of red phosphorus to black phosphorus. These crystals were found to have flatter facets and, therefore, be more suitable for exfoliation. A third set of crystals, also grown by high-pressure and high-temperature conversion of

commercial red phosphorus, were obtained from the group of Prof Takashi Taniguchi from the National Institute for Materials Science in Tsukuba, Japan.

The crystals were exfoliated onto prime grade Si $\langle 100 \rangle$ wafers, 650-700 μm in thickness, with 300 nm of dry chlorinated thermal oxide on both sides and single side polished. The wafers were purchased from NOVA Electronic Materials LLC, heavily p-doped with to a produced-specified resistivity of 0.01 - 0.02 Ωcm . The wafers were purchased in 6 inch size (15.24 cm) and were then manually sliced in 0.5 to 1.0 inch squares (1.27 to 2.54 cm). The exfoliation and characterization was performed in a class 1000 micro-fabrication cleanroom facility unless specified otherwise.

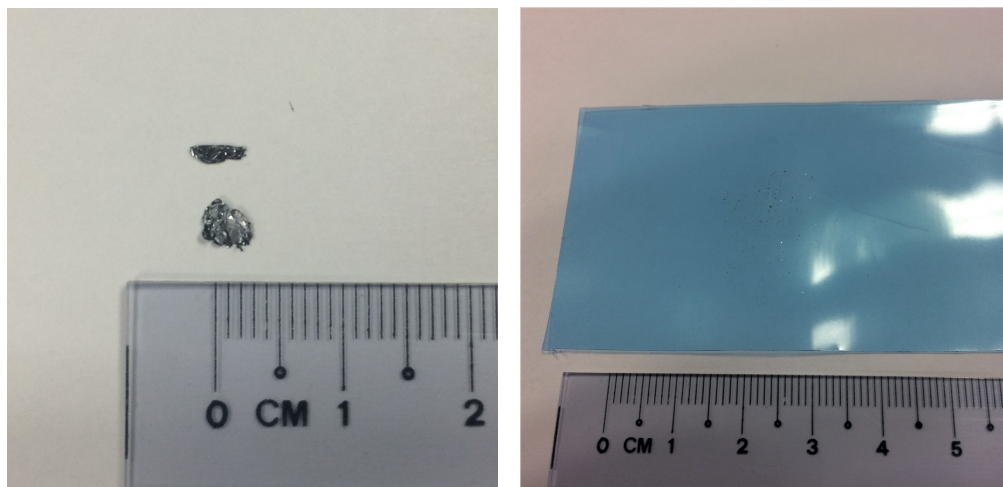


Figure 3.1.1: **(a)** Two pieces of millimeter-sized bulk bP purchased from “SmartElements” GmbH. **(b)** Tape with exfoliated black phosphorus (small black speckles).

The exfoliation is performed in the following steps. Diced wafer pieces (from now on also referred to as “wafers”) are placed in an acetone-filled beaker and cleaned in an ultrasonic bath for 5 min. The wafers pieces are then transferred to an isopropyl alcohol (IPA) beaker and cleaned for another 1-3 min in ultrasonic bath. The wafers are then taken out of the beaker and dried using compressed N_2 gas. After the wafers are cleaned, the Nitto tape is cut into roughly 3 cm by 20 cm stripes. A piece of

bulk black phosphorus is placed near one end of the tape, which is then compressed against the other end. The tape is slowly pulled apart and the procedure is repeated until small black phosphorus pieces cover an area on both ends of the tape, which is comparable or slightly larger in size than the substrate, Figure 3.1.1 (a). The two ends of the tape are separated by cutting in the middle with scissors. The wafers are placed on a flat surface with the polished side up and the tape is slowly lowered onto them, so as to avoid the formation of air bubbles between the tape and the substrate. The tape is pressed against the substrate with a thumb for about 10 sec. The tape is then slowly peeled off from the wafer, with a rate of about 10 mm/s. Figure 3.1.1 shows photographs of millimeter-sized black phosphorus crystals and the tape before placing it on the wafer.

The obtained wafers are covered by small, micrometer-sized bP crystals. The wafers are examined under a 10X or 20X optical microscope in order to locate ultrathin bP crystals. Crystals with thickness below 15 nm appear blue in color. Suitable thin-looking crystals are chosen for further characterization and device fabrication by noting down the coordinates relative to one of the wafer's corners and by acquiring optical microscope images.

3.2 Dry Transfer Method

Most of the experiments and devices presented in the results chapter require the stacking of a micrometer-sized ultrathin bP crystal with another exfoliated 2D material, like graphene or hBN. In order to obtain a good heterostructure the interface between the adjacent 2D crystals needs to be atomically clean [59]. Any polymer residue, moisture, or natural oxide is detrimental and this puts severe requirements and limitation on the transfer process [18]. The contact surfaces must be atomically

smooth and clean in order to avoid adsorption of water molecules or hydrocarbons. Polymer coating of the contact surfaces must also be avoided, or must be followed by high temperature annealing. Since the size of the exfoliated monolayers is usually on the order of tens of micrometers, the transfer process must also allow precise alignment on the micron scale. Furthermore, the monolayers need to be identified under optical microscopy prior to the transfer, so the process must involve exfoliation on a Si/SiO₂ wafers which are known to give good contrast [19].

Here we use a dry transfer method which was developed in Refs.[24][60] and was adopted by our group [44]. The 2D crystal which is to be transferred is exfoliated on a wafer coated by two transparent polymers - a release layer and a support layer. The transparency of the polymers allows the 2D crystals to be identified under optical microscopy, while the release layer allows the crystal to be peeled off from the substrate and then transferred.

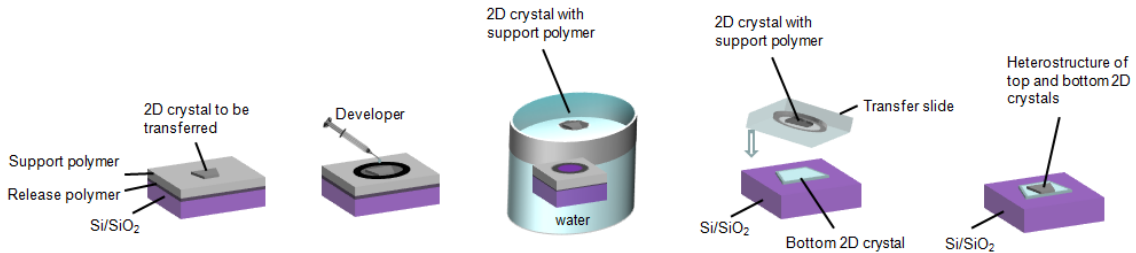


Figure 3.2.1: A step-by-step schematic of the dry transfer method for creating van der Waals heterostructures.

The dry transfer is performed in the following steps, summarized in Figure 3.2.1. Clean wafers are spin coated with polymethylglutarimide (PMGI) at 4000 rpm for 60 sec and baked on a hotplate for 3 min at 130^o C. The PMGI-covered wafer is then further coated with polymethyl methacrylate (PMMA) with molecular weight 495 000 and 3% anisole solvent (495PMMA A3) at 4000 rpm for 60 sec and baked for 3 min at 130^o C. The PMMA coating and baking is repeated two more times (a total of three)

in order to obtain a thicker PMMA film. Here the PMMA is used as a transfer layer which supports the exfoliated 2D crystal during the transfer. The underlying PMGI layer is used as a sacrificial release layer which can be liquefied using a developer agent, thereby allowing the release of the PMMA film from the wafer, see Figure 3.2.1, step 1. The transfer continues as follows.

The wafer coated with PMGI and PMMA is used as a substrate for micromechanical exfoliation, as described in the previous section. The 2D material which is to be transferred is exfoliated onto the PMMA film and a suitable crystal for the transfer is chosen under optical microscopy. The crystal is then placed in the center of the field of view of a 5X optical microscope. Using sharp metal tweezers, and while looking under the microscope, a circle with diameter of about 4-5 mm is scratched by hand around the 2D crystal. The scratch effectively tears a small channel in the PMGI+PMMA film. Next, small droplets of a PMGI developer liquid, MicroChem MF319, are carefully inserted (pushed into) the scratched channel using small droplets at the metal tweezers tip. The developer liquid gets underneath the PMMA and starts liquefying the PMGI layer. The hydrophobicity of PMMA ensures that no PMGI is likely to get on top of the PMMA circle near the chosen 2D crystal, but still the MF319 has to be inserted into the channel carefully under 5X magnification. After a typical period of 1 to 10 min the PMGI film fully liquefies and the PMMA circle, with the 2D crystal on top, are released from the substrate. If necessary, additional MF319 is inserted into the channel during this time period. See Fig 3.2.1 step 2.

Next, the wafer with the detached (floating on MF319 droplets) PMMA circle is carefully placed in a water beaker. The hydrophobicity of the PMMA film ensures that the small detached circle will remain floating on top of the water surface, as illustrated in Fig 3.2.1 step 3.

Next the floating PMMA circle has to be scooped from the top of the water

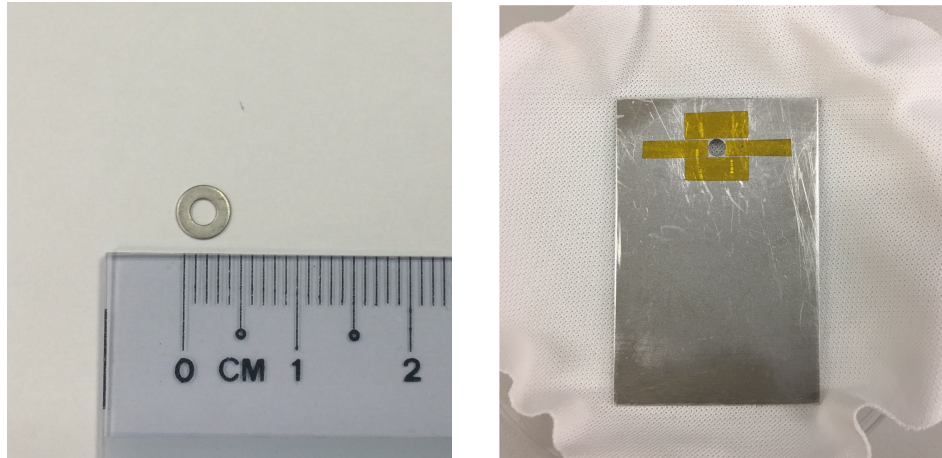


Figure 3.2.2: **(a)** A photograph of the washer used for scooping the floating PMMA film from the water surface. **(b)** The washer is attached to the transfer plate using double sided tape around the hole.

surface. The water also helps clean the remaining MF319 liquid on the bottom side of the film. We use a small metal washer with a hole with diameter slightly smaller than the PMMA circle (3.0 mm), see Figure 3.2.2(a). The washer is held using sharp metal tweezers and lowered underneath the water surface. Under good illumination the almost-transparent PMMA film can be located on the water surface and manually scooped using the washer, so that the center of the PMMA film is suspended in the washer's hole. Next, the washer is placed on a custom approximately 5 cm by 10 cm metal plate with a small see-through hole, which is slightly smaller than the outer radius of the metal washer. The washer holding the PMMA film is fixed on the plate using small pieces of double-sided tape around the plate's hole, see Figure 3.2.2(b).

Next, the plate (holding the washer and the PMMA film) is fixed face down onto a micro-manipulator stage shown in Figure 3.2.3(a). The micro-manipulator stage is brought and fixed to a custom transfer-microscope set up, shown in Figure 3.2.3(b). Now a second wafer with an exfoliated 2D crystal is brought and located under the

transfer microscope. The PMMA film is then brought above the underlying exfoliated crystal. Using 5X, 10X, and 20X objectives the top and bottom crystal are carefully aligned within a few micrometer precision. During the alignment and lowering the wafer (holding the bottom 2D crystal) is heated to 80^o C by a custom PID heater controller, in order to promote the adhesion between the PMMA and SiO₂ when the two surfaces touch. Using the micro-manipulator stage the film is slowly lowered onto the underlying wafer and additionally aligned to the bottom crystal as necessary. At the end of the lowering and aligning procedure, the edges of the washer will normally touch the underlying substrate before the 2D crystals are in contact or the PMMA is in contact with the SiO₂ surface. At this point, when no additional lowering is possible, we use a medical needle to carefully pierce the PMMA film around the crystal area (near the washer's edge) under a 5X objective. After one or a few touches with the needle the PMMA film will abruptly stick to the heated underlying wafer and the two crystals will form a heterostructure. Finally, under a 5X objective the PMMA film is carefully separated (torn) from the edge of the washer through the hole using a needle. The washer can then be lifted and removed while the remaining PMMA film, together with the 2D crystals remain onto the Si/SiO₂ substrate. In order to promote adhesion between the newly-formed heterostructure, the wafer is heated on a hotplate for 5 min at 130^o C. The PMMA film is then removed in acetone. In order to reduce PMMA residue, we use flowing acetone for a few minutes, followed by 15 min in an acetone beaker and IPA rinsing.

Successfully performing the described process for the first time can require several months of practice and takes around one day to be completed from start to finish.

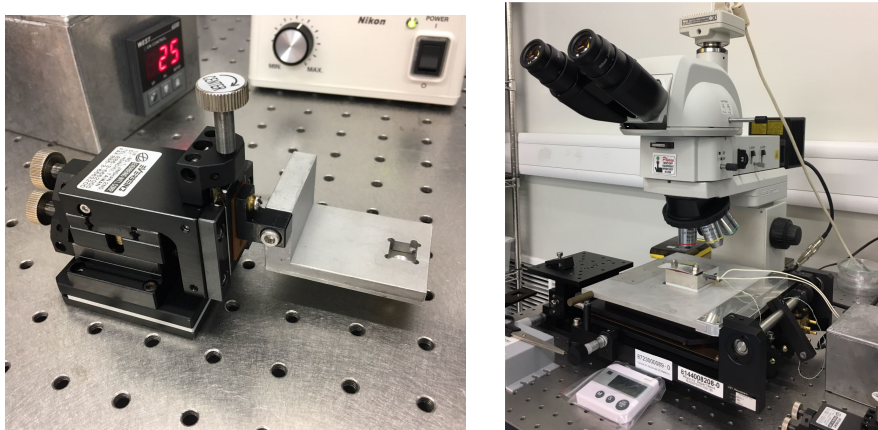


Figure 3.2.3: (a) A photograph of the micro-manipulator to which the plate with the washer is attached, and (b) the custom transfer stage with a microscope and PID heater controller.

3.3 Raman Spectroscopy

Raman spectroscopy is an important tool in the characterization of 2D materials.[61] It is a spectroscopic technique for observing the low-frequency phonon modes in a solid (or the low-energy vibrational modes of a molecule). The sample is illuminated with monochromatic laser light. The reflected light is then collected and passed through a spectrometer. The majority of the photons will be scattered elastically and there will be no change in their frequency. However, a small fraction of the photons will interact with low-energy excitations of the sample (the phonons in a solid) and will be scattered inelastically. When the reflected light is analyzed with a spectrometer the Raman-scattered photons will show as peaks shifted from the original laser frequency. The peak wavenumber offset from the main laser frequency correspond to different low-energy excitations of the sample. The peak's wavenumber (relative to the illuminating light frequency) and intensity can be used as a fingerprint of the material, and can be analyzed for extracting material properties.[61] Raman

spectroscopy is particularly well-suited for characterizing exfoliated 2D materials, because the laser beam can be easily focused down to 1 μm spot size. This makes it possible to easily perform fingerprint measurements on small crystals, unlike x-ray techniques, such as x-ray diffraction (XRD) or x-ray photo-electron spectroscopy (XPS).

For the work in this thesis we employ back-scattering Raman spectroscopy, where the crystal surface is placed normal to the incident light direction and the collected (reflected) light is parallel to the incident light. The laser wavelength is 532 nm and the typical illumination intensity is around 200 - 500 $\mu\text{W}/\text{cm}^2$. The measurements are done under 100X magnification with a spot size of around 1 μm .

In graphene the analysis of the Raman peak's shape, position, and intensity ratio can give useful information about the crystal's doping, thickness, and defect density. [61] For ultrathin bP it was found that polarization-resolved Raman spectroscopy is one of the easiest ways to determine the crystal direction.[62] When determining the crystal direction we use a polarization filter and only collect reflected light with polarization parallel to the incident light. The sample is then rotated relative to the direction of the incident polarization (which remains fixed) and a Raman spectrum is acquired every 10° or 15° . The angle at which the first Raman peak of bP (A_g^1 at 360 cm^{-1}) has its minimum corresponds to the polarization oriented along the crystal's zig-zag direction, see Figure 3.3.1.

3.4 Atomic Force Microscopy

Atomic force microscopy (AFM) is another characterization tool which is widely employed throughout the results section and in the field of 2D materials in general. AFM is a type of scanning probe microscopy in which a cantilever with a sharp tip (with

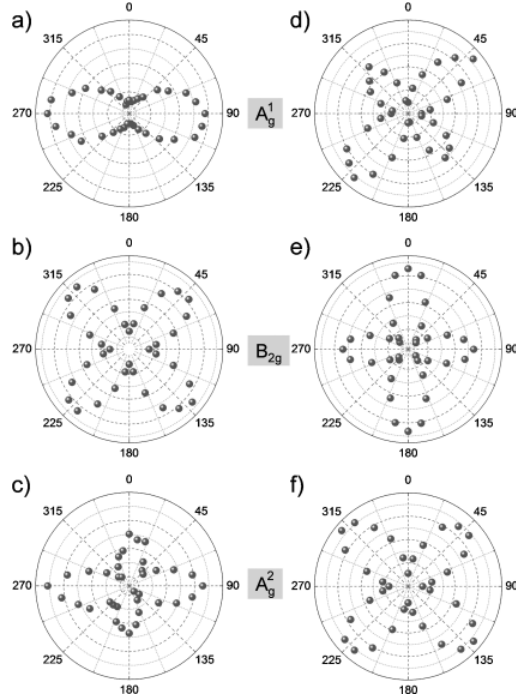


Figure 3.3.1: Polar plots of the fitted peak intensities of **(a, d)** A_g^1 , **(b, e)** B_{2g} , and **(c, f)** A_g^2 modes as a function of sample rotation angle ϑ under (a–c) parallel and (d–f) cross-polarization configurations. $\vartheta = 0$ corresponds to the polarization oriented along the zig-zag direction. Reprinted from [62] with permission from Wiley.

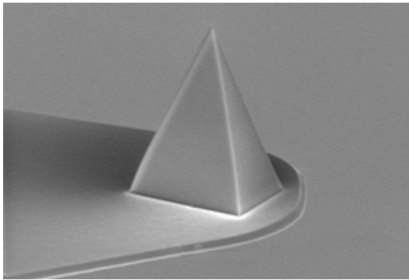
a radius of a few nm) is scanned across the surface of a sample. The backside of the cantilever serves a reflection mirror directing a laser beam into a position-sensitive photodiode. Minuscule changes in the cantilever’s deflection are amplified by the long beam path and are detected as a position change in the reflected laser spot at the photodiode. AFM is an excellent tool for scanning the surface of 2D materials with sub-nanometer resolution, thereby revealing the surface topology and artifacts like contaminants or cracks on the surface. AFM is also an accurate way to measure the thickness of the crystal.

For the research presented in this thesis we use a commercial Bruker “Dimension FastScan” AFM. The scans are performed in tapping mode in air, where the cantilever is oscillating above the sample surface and the topography is mapped by monitoring

changes in the oscillation amplitude (and minimizing them through a deflection feedback loop). Tapping mode is chosen because it enables fast scanning rates, and also allows the tip to be at a larger distance from the surface (compared to contact mode), thereby minimizing potential damage to the surface by the tip. The used AFM probe is Bruker “FASTSCAN-A” with silicon nitride cantilever, nominal 5 nm tip radius, and 1.4 MHz resonant cantilever frequency.

Shape	Resonant Freq. kHz			Spring Const. N/m			Length μm			Width μm		
	Nom.	Min.	Max.	Nom.	Min.	Max.	Nom.	Min.	Max.	Nom.	Min.	Max.
Triangular	1400	800	2000	18	10	25	27	24	30	33	30	36

Tip Specification

	Geometry:	Rotated (Symmetric)
	Tip Height (h):	2.5 - 8 μm
	Front Angle (FA):	$15 \pm 2.5^\circ$
	Back Angle (BA):	$25 \pm 2.5^\circ$
	Side Angle (SA):	17.5°
	Tip Radius (Nom):	5 nm
	Tip Radius (Max):	12 nm
	Tip SetBack (TSB)(Nom):	5 μm
	Tip Set Back (TSB)(RNG):	0 - 7 μm

Tip Schematic

Figure 3.4.1: Specifications of the Bruker “FASTSCAN-A” AFM tip.[63]

3.5 Micro-fabrication of Electrical Contacts

Performing electrical transport measurements on exfoliated ultrathin bP requires the fabrication of electrical contacts to the crystal. The width of the electrical contacts, on the crystal side, has to be on the order of one micrometer or less. At the measurement-equipment side the electrical connections have to be large enough for standard 50 Ω Bayonet Neill–Concelman (BNC) connectors. The transition from micrometer-sized contacts on the crystal to BNC connectors is achieved in three stages: micro-fabrication, wire-bonding, and a beak-out box. First, micrometer-sized

metal contacts are fabricated using electron beam lithography (EBL), thin film deposition, and lift off. The thin-film contacts are on the Si/SiO₂ wafer and extend outside of the sample to include $\approx 100 \times 100 \mu\text{m}^2$ pads. These pads allow the sample to be packaged and wire-bonded to a standard chip carrier. Finally, the connections from the chip carrier are extended using wires into a breakout box with BNC connectors. The next subsections describes the micro-fabrication of the metal thin-film electrical contacts.

3.5.1 Electron Beam Lithography

All studied ultrathin bP devices were fabricated using the following general procedure. After a suitable crystal is selected (or a heterostructure is assembled using the dry transfer method) the wafer is prepared for EBL by coating with PMMA resist. We use two coatings of 495 PMMA A3 at 2000 rpm for 80 sec, followed by a 3 to 5 min baking at 170^o C. Then another layer of 950 PMMA A5 is spin coated at 4000 rpm for 90 sec and baked at 170^o C for 5 min. The bilayer PMMA serves two purposes; first the 495 PMMA A3 was found to leave less residue after removal of the resist with acetone, and second, the lower molecular weight of the bottom layer creates an undercut profile which facilitates lift off.

First, a relatively large 1.2 x 1.2 mm² EBL pattern, consisting of regularly spaced small markers is exposed in the area of the crystal using the coordinates relative to the wafer edge obtained during optical microscopy. This large pattern is referred to as “markers” and it allows a fine alignment of the electrode pattern to the crystal in the second EBL step. We use a commercial FEI “NovaNanoSEM 230” apparatus, which is designed as a scanning electron microscope, but was converted to an EBL writer using a proprietary Nanometer Pattern Generation System (NPGS) software.

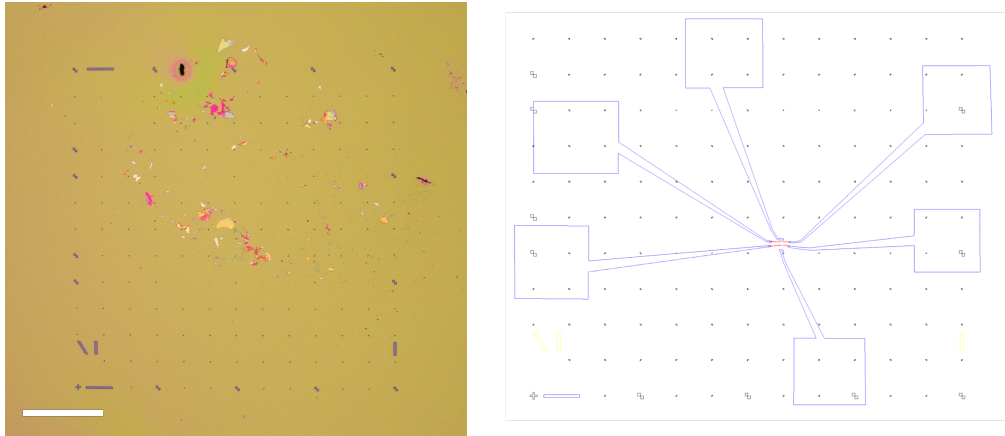


Figure 3.5.1: **(a)** Optical microscope image under 5x magnification of a wafer with exfoliated bP and after EBL alignment marker exposure and development. The yellow color is the PMMA resist. The magenta-color dots and lines are the markers, exposing regions of Si/SiO₂ under the PMMA. The scale bar is 300 μm . **(b)** A CAD drawing of an electrode design . The blue polygons are the larger features of the design. The red polygons are the small features. The black structures show the already alignment markers, which have been exposed already.

The beam energy is 30 kV in all EBL steps. For the markers we use an exposure dose of 550 $\mu\text{C}/\text{cm}^2$. After writing the alignment markers the PMMA is developed in a mixture of methyl isobutyl ketone (MIBK) and IPA (with an MIBK:IPA ratio of 1:3) for 1 min, followed by a 1 min rinse in pure IPA.

Microscope images of the markers pattern and the crystal are then acquired at 5X and 100X magnification. An optical image under 5X magnification of a wafer after writing the EBL markers is shown in Figure 3.5.1(a). The optical images are then overlaid on top of the markers pattern in “DesignCAD Express” software and suitable electrodes are designed on the phosphorene crystal. A representative electrode pattern is shown in Fig 3.5.1(b). The electrode design pattern consists of two layers: one for the smallest features near the micrometer-sized crystal (shown as red polygons), and a second layer with the larger connections and the bonding pads (blue polygons).

The sample is then brought for a second EBL writing step. Using the markers

near the crystal, the design is carefully aligned using the NPGS software and then exposed. We use a dose of $475 \mu\text{C}/\text{cm}^2$ for the layer with the smallest features and a dose of $525 \mu\text{C}/\text{cm}^2$ for the larger connections and bonding pads. The pattern is developed in 1:3 MIBK:IPA for 1 min and rinsed in pure IPA for another 1 min.

3.5.2 Thermal Evaporation and Lift-off

After the EBL pattern is ready the metal electrodes are deposited using a thermal evaporator. We use a commercial Kurt J.Lesker “Nano 36” thermal evaporator to deposit a thin layer of Ti at a rate of $0.5 \text{ \AA}/\text{s}$, followed by 50 to 80 nm of Au at $1 \text{ \AA}/\text{s}$. The exact thicknesses are specified in the respective results section for each device. The Ti serves as a wetting layer allowing the Au to stick to the SiO_2 substrate and the sample. The deposition is performed after evacuating the chamber down to about 10^{-6} Torr and a typical pressure during evaporation in range of 10^{-5} Torr.

After thermal evaporation the wafer is manually cut so that no lateral dimension exceeds 1.1 cm, in order to allow packaging. The cut sample is placed in an acetone beaker for 3 to 12 hours for lift-off. After the residual PMMA and Au film detach from the substrate, the wafer is placed in clean acetone for 15 min, followed by rinsing in IPA and drying with compressed N_2 . Optical images of some of the measured devices under 100X magnification will be shown in the results section.

3.6 Packaging and Wire-bonding

After lift off the sample is fixed onto a 44-pin leadless chip carrier purchased from Spectrum Semiconductor Materials Inc (model MLCC04420). The wafer is fixed to the chip carrier using conducting silver paint. The thin-film Au pads are bonded to the carrier using a commercial WestBond “7700E” manual ultrasonic wedge-wedge

wire bonder. The bonding force of the wire bonder is set to the equivalent of 20 g pressure, in order to avoid cracking the SiO_2 dielectric and gate leakage current. A photograph of a complete device after wire bonding is shown in Figure 3.6.1(a).

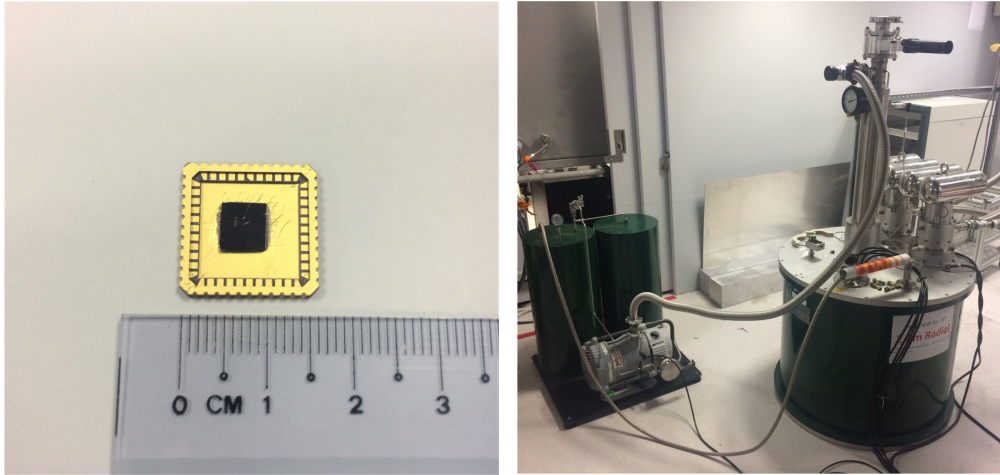


Figure 3.6.1: **(a)** Photograph of a completed device ready for measurement. The Au-plated square is the 44-pin chip carrier. The dark square in the middle is the Si/SiO_2 wafer. The Au bonding pads and Al bonding wire are barely visible. **(b)** Photograph of the cryogen-free 16 Tesla VTI system.

3.7 Electrical Transport Measurements

Electrical transport measurements are performed using direct current (DC) in either two- or four-probe configuration. When concentrating on material properties (like mobility, conductance, etc) we employ four-probe measurements, while FET device characteristics (on-current, on-off ratio, I-V curves, etc) are taken from two-probe measurements. Four-probe measurements are performed using either a Keithley “2400 SourceMeter” in Ohms mode, or a Keithley “2182a Nanovoltmeter” together with a Keithley “6430 Sub-Femtoamp Remote SourceMeter” as a current source. Two-probe measurements are performed using a Keithley “6430 Sub-Femtoamp Remote

SourceMeter”. The exact values of the sourced voltage or current are specified when discussing the respective measurement in the results section.

The measurements in section 4.1 were performed using a Scientific Instruments “SR 830 Lock-In Amplifier”. In section 4.3 low-noise measurements are performed using a Scientific Instruments “SR 830 Lock-In Amplifier” together with a Keithley “6221 DC+AC Current Source”.

3.8 Low-Temperature and Magnetic Field Measurements

The low-temperature measurements are performed in either one of three cryogen-free systems: a custom 9 Tesla or 16 Tesla cryogen-free measurement system (CFMS) with a 3 Kelvin variable temperature insert (VTI) produced by Cryogenic Ltd; or a 4 Kelvin closed-cycle refrigerator system produced by Janis Research Company LLC. A photograph of the 16 Tesla system is shown in Figure 3.6.1(b).

Transport measurements in magnetic field were performed in the Cryogenic Ltd 9T CFMS using a superconducting magnet.

Chapter 4

Results

This chapter summarizes the results and experimental findings of the PhD research. It describes the isolation and characterization of ultrathin bP and electrical transport studies of van der Waals heterostructures of the material.

4.1 Electrical Transport in Bulk bP

Electrical transport measurements were performed on millimeter-sized bulk bP provided by Prof Takashi Taniguchi's from National Institute for Materials Science, Tuskuba, Japan. The crystals were grown by conversion of red phosphorus at high pressure. For transport measurements a crystal was fixed in a 44-pin chip carrier (methods section 3.6) using double-sided Kapton tape. Electrical contacts were made using a combination of wire-bonding and silver paint. The wire was first bonded to the chip carrier and pulled towards the crystal. It was then manually cut with scissors and fixed onto the crystal with a small droplet of silver paint under a 2.5X optical microscope at the wire bonder. A total of 6 contacts were fabricated; two on both ends of the crystal for current biasing and 4 on the side for longitudinal and trans-

verse resistivity measurement. The dimensions of the crystals were measured using a microscope with calibrated 5X objective. After completing the electrical transport measurements, the direction of the crystal was determined using polarization resolved Raman spectroscopy and was found to be in the armchair direction. Transport in other crystal directions was not measured. The 4-probe resistivity and Hall effect across ± 2 Tesla were measured at temperatures between 3 K and 300 K at 1 μ A current bias. The results are shown in Figure 4.1.1.

Starting from 300 K the resistivity slightly increases with decreasing temperature down to 220 K, followed by a slight decrease down to about 50 K and a sharp increase below for $T < 50$ K. The carrier concentration in Figure 4.1.1(b) also exhibits three different regions. It first decreases from 300K down to 220 K, followed by a less steep decrease between 220 K and 50 K and a sharp decrease for $T < 50$ K. The Hall mobility is seen to increase with decreasing temperature down to 50 K following $\mu \propto T^{-3/2}$ characteristic of phonon scattering in 3D.[58] Below 50 K the mobility remains constant.

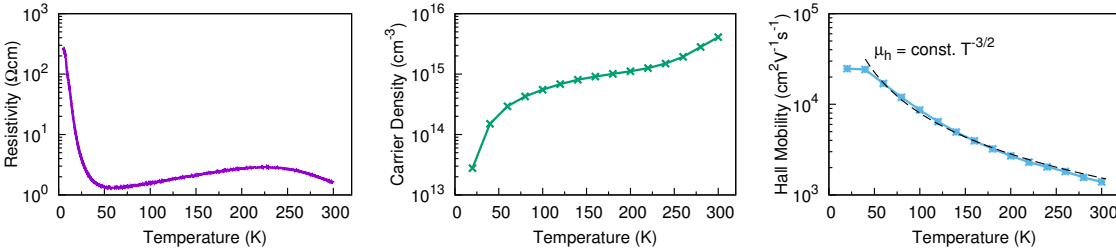


Figure 4.1.1: Measured resistivity, carrier concentration, and Hall mobility of a bulk bP crystal.

The measured electrical transport is characteristic of a doped narrow-band-gap semiconductor and can be understood as follows. The increase in carrier concentration above 200 K is the beginning of the intrinsic regime where carriers are starting to get thermally excited across the band gap. The relatively constant (temperature

independent) carrier density between 220 K and 50 K is indicative of unintentional dopants. From the sign of the Hall signal we conclude that carrier concentration is p-type and the dopants are acceptors, consistent with bulk measurements in the literature, see section 2.3. Below 50 K the acceptor states freeze out and the carrier density decreases sharply.

The temperature dependence of the resistivity can now be understood as a combination of the carrier density's and mobility's temperature dependence. The increase in resistivity with decreasing temperature between 300 K and 200 K is due to the reduction in intrinsic (thermally excited) carriers. The slight decrease in resistivity between 220K and 50K is due to the increasing mobility while the carrier density remains largely unchanged. The sharp decrease in resistivity below 50 K is due to the sharp decrease in carrier density due to the freezing of the acceptors states.

4.2 Electric Field Effect in Few-layer bP

The results of this section are published in *Appl. Phys. Lett.* **104**, 103106 (2014), Steven P. Koenig, [Rostislav A. Doganov](#), Henrik Schmidt, A. H. Castro Neto¹, and Barbaros Özyilmaz.

Ultrathin bP is obtained by exfoliating bulk bP crystals purchased from “SmartElements” GmbH using Nitto scotch tape (see section 3.1). The crystals are exfoliated onto prime grade Si wafers with 300 nm SiO₂ which is used as gate dielectric in the field-effect device. Ultrathin crystals were identified with an optical microscope and further characterized by AFM and Raman spectroscopy. Figure 4.2.1(a) shows a microscope image of a typical ultrathin bP crystal and the insert shows the fabricated devices after deposition of electrical contacts. An AFM scan is shown in Figure 4.2.1(c), while the Raman spectrum is shown in Figure 4.2.1(d). Three Raman peaks

can be seen at wavenumbers 466 cm^{-1} , 438 cm^{-1} , and 360 cm^{-1} . These can be identified as the A_g^2 , B_{2g} , and A_g^1 peaks observed in Raman studies of bulk bP.[64, 65]

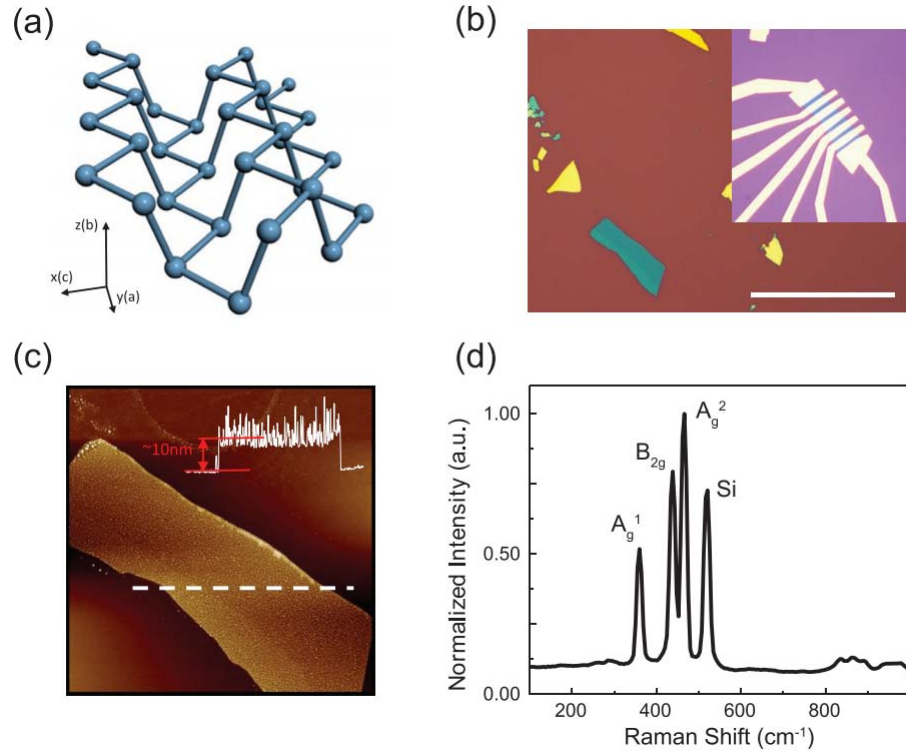


Figure 4.2.1: **(a)** Lattice structure of a single layer of phosphorene. **(b)** Micrograph of an exfoliated ultrathin bP crystal on a Si/SiO₂ wafer. The inset is an image of a FET device after fabrication of metal electrodes. Scale bar is 50 μm . **(c)** AFM scan and **(d)** Raman spectrum of the ultrathin bP crystal from (b). Reprinted from *Appl. Phys. Lett.* **104**, 103106 (2014), with the permission of AIP Publishing.

The AFM scan in Figure 4.2.1(c) shows that there is a considerable roughness on the surface of the exfoliated ultrathin bP crystal. This demonstrates that although bulk bP is the most stable form of phosphorus, few-layer crystals are not entirely nonreactive in ambient conditions.[66] The deterioration of the surface roughness with time was observed in situ under AFM. The root mean square roughness against time is plotted in Figure 4.2.2(b), whereby a bP crystal was exfoliated and a 500×500

nm^2 area was continuously scanned. The first AFM scan is taken approximately 21 min after the exfoliation and the calculated roughness is 0.43 nm. After additional 9 min the roughness increases to 0.59 nm, and after 41 min of air exposure it further increases to 0.98 nm.

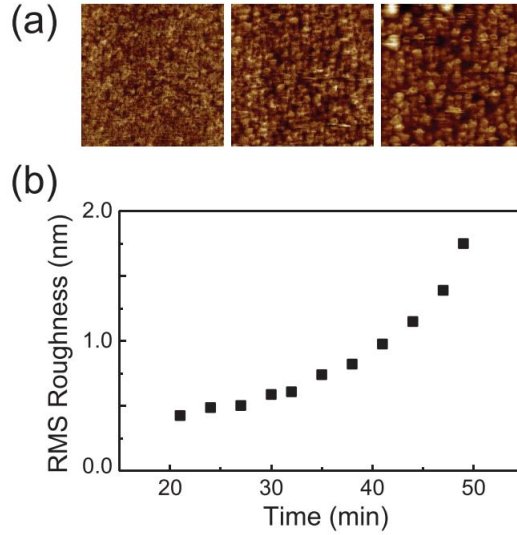


Figure 4.2.2: **(a)** AFM topology of the surface of an ultrathin bP crystal 21 min, 30 min, and 41 min (from left to right) after exfoliation in ambient conditions. The scan size is 500 x 500 nm. All three AFM scans were acquired at the same location of the surface of the crystal. **(b)** Measured RMS roughness (extracted from the AFM images) versus time after exfoliation in ambient conditions. Reprinted from *Appl. Phys. Lett.* **104**, 103106 (2014), with the permission of AIP Publishing.

In order to reduce the effect of degradation in electrical transport measurements, the exfoliated crystals used for device fabrication were rapidly covered with PMMA after being identified under the optical microscope. The average duration before an exfoliated crystal was coated with PMMA is around 30 min. Ti+Au electrodes (5 nm + 90 nm) are fabricated by EBL and thermal evaporation. The devices were characterized in a four-probe configuration using an SRS lock-in amplifier (13 Hz) to extract the field effect mobility and in a two-probe DC configuration to extract the on-off current ratio.

In Figure 4.2.3(a) we show the conductance versus gate voltage, V_{bg} , at room temperature. The device was biased with a constant current of 50 nA while the gate voltage, V_{bg} , was varied between -60 V and +60 V. The field effect mobility, μ_{FE} , is extracted from the linear conduction region using

$$\mu_{FE} = \frac{L}{WC_g} \frac{dG}{dV_{bg}} \quad (4.2.1)$$

where G is the conductance, L and W are respectively the length and width of the channel, and C_g is the gate capacitance. For the discussed device we extract a field effect mobility of approximately $300 \text{ cm}^2\text{V}^{-1}\text{s}^{-1}$ at room temperature. In these early devices we did not determine the crystal orientation and the transport direction, so the reported value of the mobility might not be the maximal one and could be affected by the unknown transport direction.

The linear I-V characteristic of the device, shown in Figure 4.2.3(b), confirm that the electrical contacts are ohmic at negative gate voltages. To accurately measure the on-off ratio of the device we use two-probe DC characterization at fixed source-drain voltage. Shown in Figure 4.2.3(c) is temperature dependent source drain current, I_{sd} , versus V_{bg} at $I_{sd} = 50 \text{ mV}$ and various temperatures between 5 K and 200 K. For $T > 200\text{K}$ we observe a significant gate sweep hysteresis which is can be seen in the plotted gate sweep at $T = 250 \text{ K}$ in Figure 4.2.3(d). The temperature-dependence of the hysteresis is plotted in the inset. The fact that the hysteresis has a positive direction (as defined in ref.[67]) leads to the conclusion that it is due to charge traps.[67] This is also in agreement with the fact that the hysteresis vanishes at low temperatures.[67] The observed ambipolar transport in Figure 4.2.3(c) shows an asymmetry between the p-type and n-type transport which will be studied in more detail in the next sections.

In conclusion, a novel 2D material exfoliated from bulk bP was isolated using mechanical exfoliation. Few-layer phosphorene field effect devices on Si/SiO₂ were characterized in electrical measurements. We find a hole mobility of $\approx 300 \text{ cm}^2\text{V}^{-1}\text{s}^{-1}$ and a FET on-off ratio in the range 10^3 - 10^5 . The field effect mobility extracted here is lower than the Hall mobility measured in bulk bP. By in situ measurement of the surface roughness, using AFM, exfoliated bP was found to considerably degrade in ambient conditions. Isolation and device fabrication of ultrathin bP in an environment with low oxygen and water content will be essential for studying the intrinsic material properties and for enabling electronic applications.

4.3 Van der Waals Passivation of Few-layer bP in Inert Atmosphere

The results of this section are published in *Nature Communications* **6**, 6647 (2015), [Rostislav A. Doganov](#), Eoin C.T. O'Farrell, Steven P. Koenig, Yuting Yeo, Angelo Ziletti, Alexandra Carvalho, David K. Campbell, David F. Coker, Kenji Watanabe, Takashi Taniguchi, Antonio H. Castro Neto, and Barbaros Özyilmaz.

The initial work in the preceding section demonstrated that exfoliated few-layer bP is not fully chemically stable under ambient conditions. A considerable degradation of the surface one hour after exfoliation was observed in situ using AFM. The degradation is also observable under optical microscopy if the exfoliated crystals are left in ambient conditions for more than 24 hours.[16] Furthermore, theoretical papers show that oxygen can easily adsorb onto phosphorene under normal environmental conditions.[68] In these early stage of ultrathin bP research the disintegration of the ultrathin material limits the possibility to study monolayer crystals and also raises

the question of how degradation affects the physical properties. A robust process for passivating ultrathin bP without any exposure to ambient air, or precursor treatment is essential for progress in the field.

In this section we demonstrate that creating a van der Waals heterostructure with graphene or hBN onto ultrathin bP isolated in an inert Ar gas environment preserves the few-layer crystal and protects it from degradation in ambient air. We show that the van-der-Waals-passivated bP is preserved under ambient conditions by examining the AFM topology and the Raman spectrum. Graphene and hBN have excellent properties to act as a degradation barrier for bP, because they are atomically thin, non-reactive, and exhibit near-perfect gas impermeability. [69] To study the transport properties we fabricate ultrathin bP FETs that enable comparison of passivated and unprotected regions. This enables us to study the charge transport properties of pristine ultrathin bP; to observe in situ how degradation impacts the charge transport properties, and allows us to exclude the effect of sample-to-sample variation and bulk material quality. Passivated ultrathin bP FET channels are found exhibit an improved (10- to 100-fold) electron conduction and electron mobility resulting in almost symmetric n-type and p-type characteristics. The observed ambipolar behavior agrees with theoretical band-structure calculations of intrinsic bP.[50, 54]

We start by exfoliating few-layer ultrathin bP onto Si/SiO₂ wafers in an Ar-filled glovebox with O₂ and H₂O content of less than 2 ppm. Ultrathin crystals of thickness between 3 and 10 nm are identified using an optical microscope inside the Ar-filled glovebox. The passivation process is similar to the dry transfer method described in section 3.2. Either graphene or hBN is exfoliated onto polymer-coated Si/SiO₂ wafers. The spin-coated polymers are PMGI and PMMA, which are used as release and support layers. After exfoliation and identification of a suitable graphene or few-layer hBN crystal, the PMGI polymer is developed and the exfoliated crystal,

supported by the PMMA, is brought into the glovebox after desiccation in a loading chamber. To finish the passivation process, the graphene or hBN is lowered on top of the ultrathin bP using an alignment stage inside the glovebox and the PMMA layer is removed with acetone.

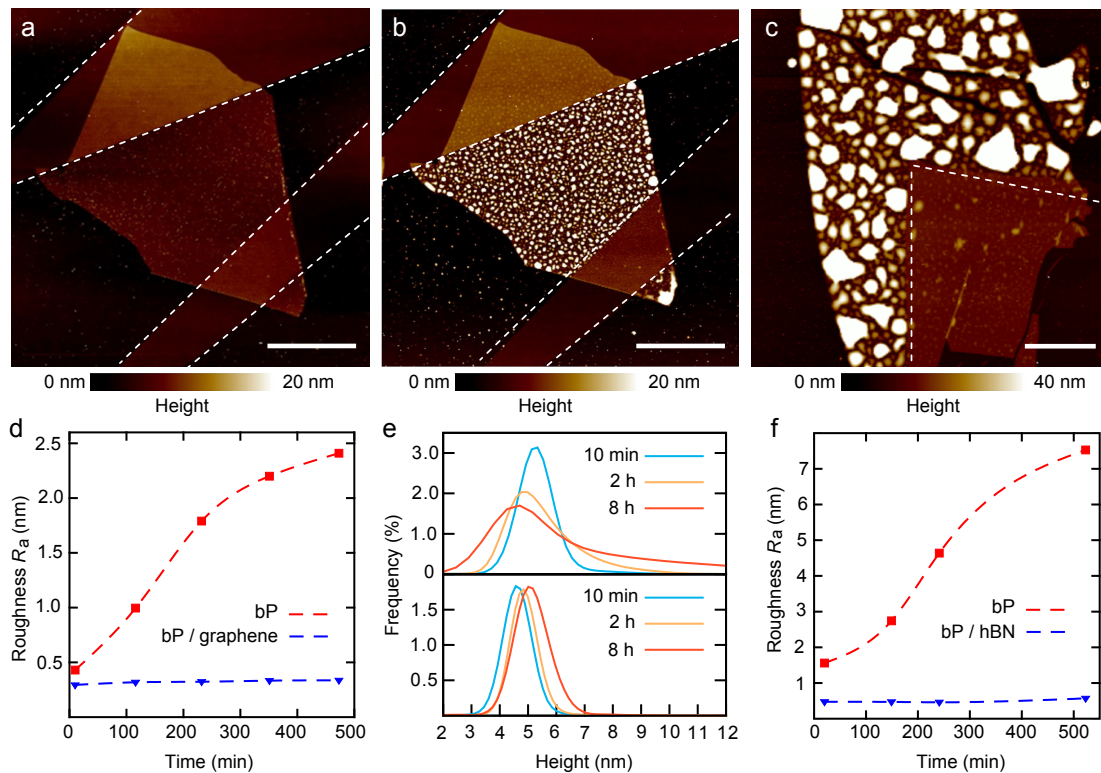


Figure 4.3.1: **(a)** - **(b)** AFM images of a 5 nm thick phosphorene crystal partly covered with graphene, acquired respectively 10 min and 24 hours after removal from the inert atmosphere and exposure to ambient air. The white dashed lines outline the top graphene crystal. **(c)** AFM image of 10-nm-thick bP crystal partly covered with hBN after 5 days in ambient air. Scale bar in all images is 4 μm . **(d)** Average roughness, R_a , against time in ambient air for the covered (blue triangles) and unprotected (red squares) surface of the sample from (a) and (b). The colored dashed lines are a guide to the eye. **(e)** Height histogram, of the unprotected (top) and graphene-covered phosphorene surface (bottom) at different times after exposure to ambient air. **(f)** R_a against time for the covered (blue triangles) and hBN-covered (red squares) surface of the phosphorene / hBN heterostructure sample from (c).

To show that the resulting van der Waals heterostructure protects the pristine bP

crystals we study the AFM topology and Raman spectrum of passivated and unprotected surfaces. Figures 4.3.1(a)&(b) show AFM images of 5 nm thick bP passivated with graphene and exposed to ambient conditions for 10 min and 24 hours. From the AFM topology we observe that the unprotected surface of the ultrathin bP develops significant roughness over time while parts of the crystal that are passivated with graphene do not show significant change in the surface topology. Similar behavior can be seen in crystals passivated with hBN, shown in Figure 4.3.1(c). To quantify the AFM measurements, in Figures 4.3.1(d)&(f) we show the average surface roughness, R_a , versus time in air for the graphene-passivated and unprotected regions of the surface. Here the surface roughness is extracted as the average of the absolute values of the surface height fluctuations, $R_a = \sum_i^N |\Delta z_i|/N$, where Δz is height fluctuation measured from the mean surface plane of the scan. Because of graphene's ultrathin character we can assume that the measured roughness value is entirely determined by the underlying ultrathin bP. We see in Figure 4.3.1(d) that even in the first AFM image, only 10 min after exposure to ambient conditions, the unprotected surface roughness is $R_a = 0.43$ nm, in comparison to $R_a = 0.29$ nm for the surface passivated with graphene. During a time period of 8 hours the R_a value of the passivated phosphorene does not change while the roughness in the unprotected area increases to above 2.0 nm due to surface deterioration. In Figure 4.3.1(e) we analyze the height histograms of the AFM scans from the passivated and unprotected regions. The protected surface exhibits a normal height distribution, which does not change over time, besides a 0.5 nm shift of the average height which could suggest deterioration at the bottom surface (on the SiO_2 side). In contrast, the unprotected surface region exhibits an asymmetric height distribution even in the first scan, which further broadens with time and develops tails for heights above 8 nm. After additional exposure the roughness on the unprotected surface gathers into droplets, which are

visible under optical microscopy, see Figures 4.3.1(c) and 4.3.2(a)&(b). In the passivated ultrathin bP surface deterioration can be observed after a long period of 48 hours in ambient conditions, predominantly near the edges of the passivated region, as shown in Figure 4.3.2(b).

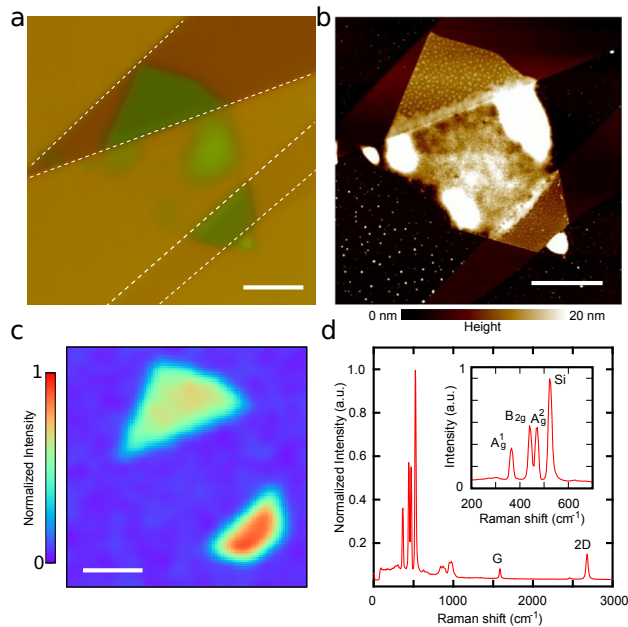


Figure 4.3.2: **(a)** Micrograph of the bP/graphene sample from the previous figure after 48 hours in ambient air. **(b)** AFM scan acquired after 48 hours of exposure to ambient conditions. Scale bar is 4 μm . **(c)** Spatial map of the normalized intensity of the bP A_g^1 Raman peak. **(d)** Raman spectrum of the bP/graphene van der Waals heterostructure. The inset shows a close up on the bP peaks.

In order to probe the quality of the passivated ultrathin bP we examine the Raman spectrum after 48 hours in ambient conditions at which point the unprotected phosphorene has fully degraded, see Figures 4.3.2(a) & (b). The Raman spectrum confirms the quality of the passivated ultrathin bP by the presence of well-defined peaks as expected for phosphorene (the A_g^1 , B_{2g} , and A_g^2 Raman peaks in the back scattering configuration, as in Section 4.2). The Raman spectra of the graphene or hBN layers in the heterostructure are not perturbed by the underlying bP, which rules

out reactions between the 2D materials. In Figure 4.3.2(c) we plot a spatial map of the intensity of the A_g^1 Raman peak. The peak can only be measured under the graphene passivation, while the fully oxidized surface does not show any characteristic Raman signal.

We now study the difference between the charge transport properties of the passivated and unprotected ultrathin bP by fabricating FET channels partly covered with hBN. Electrodes to the passivated 2D semiconductor are fabricated on both sides of the hBN strip and additional electrodes are deposited to probe the unprotected region of the same phosphorene crystal. The device geometry and a micrograph of a representative sample are shown in Figure 4.3.3(a)& (b). The four-probe conductances versus gate voltage, V_g , of the passivated and unprotected ultrathin bP for two typical devices at room temperature are shown in Figure 4.3.3(c). In the unprotected FET channel at $V_g = -70$ V the p-type conductance increases to more than 2 μ S, while at positive V_g the n-type electrical conductance remains at least 10 times lower. A higher p-type conductance and suppressed n-type transport for the unprotected phosphorene is in agreement with our previous results (section 4.2). On the other hand, the passivated phosphorene exhibits sheet conductance over 5 μ S at $V_g = +70$ V thereby having almost symmetric n-type and p-type conductance centered around $V_g = 0$. In the passivated ultrathin bP the n-type conductance is enhanced more than 10 times, while the off current and the hole transport remain almost unchanged besides a p-doping corresponding to $\Delta V_g \approx 30$ V, which suggest p-doping of few-layer bP upon exposure to air.

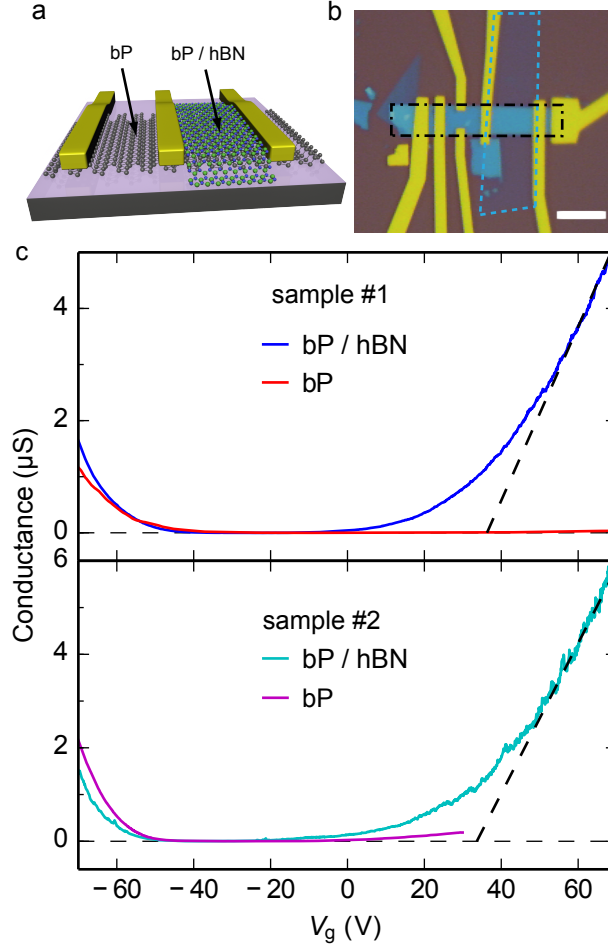


Figure 4.3.3: **(a)** Schematic of the device geometry. **(b)** Micrograph of a typical device. The ultrathin bP crystal is outlined with a black dashed-dotted line and the passivating hBN crystal is in blue dashed line. Scale bar is 3 μm . **(c)** Four-probe conductance against gate voltage, V_g , of the graphene-covered and unprotected channels of two ultrathin bP FETs at $V_{sd} = 50$ mV at room temperature. Sample #1 thickness is ≈ 4.5 nm and sample #2 thickness ≈ 5.7 nm. The back gate voltage has been shifted by -10 V and -40 V respectively for the exposed region.

Using the four-probe conductance discussed above we can estimate the field effect mobility using Eq. 4.2.1. With the SiO_2 gate we can not accumulate enough carriers to reach fully into the conduction or valence bands (and correspondingly to $dG/dV_g = \text{const.}$) so the actual field effect mobility of our FETs is expected to be higher than what we extract with Eq.4.2.1. On the p-conduction side, at negative gate

voltage, μ_{FE} is above $10 \text{ cm}^2\text{V}^{-1}\text{s}^{-1}$ at room temperature for both the unprotected and passivated ultrathin bP channels. At lower temperature, $T = 200 \text{ K}$, we extract $\mu_{\text{FE}} = 118 \text{ cm}^2\text{V}^{-1}\text{s}^{-1}$ for the unprotected region and $86 \text{ cm}^2\text{V}^{-1}\text{s}^{-1}$ for the passivated FET channel. These values are in agreement with what has been measured previously in phosphorene of comparable thickness.[13, 14] On the n-conduction side, at $V_g = 70 \text{ V}$, for the crystal the improved electron transport leads to enhanced electron field effect mobility. For the n-type conduction in the passivated ultrathin bP we extract μ_{FE} over $10 \text{ cm}^2\text{V}^{-1}\text{s}^{-1}$ while the mobility in the unprotected phosphorene remains 10 to 100 times smaller. At $T = 200 \text{ K}$ in the passivated crystal we obtain n-type mobility of $62 \text{ cm}^2\text{V}^{-1}\text{s}^{-1}$, while in the unprotected channel it does not exceed $5 \text{ cm}^2\text{V}^{-1}\text{s}^{-1}$. Similar improvement of the electron transport and n-type field effect mobility was observed and reproduced in five out of five passivated exfoliated bP samples. In these experiments the crystal orientation and the transport direction were not determined so the reported absolute values of the mobility could be affected by the unknown crystal orientation. However, the experiment is designed as a comparison of the transport properties of an exposed and passivated channel on the same underlying bP crystal, with the same transport directions, so the unknown overall transport direction can account for the observed changes in electron mobility.

We now characterize the I-V behavior of sample #2 from Figure 4.3.3 which is performed at a temperature $T = 200 \text{ K}$ in order to exclude complications arising from the gate hysteresis (see section 4.2). In Figure 4.3.4(a) we show the two-probe conductance against gate voltage for the unprotected and passivated ultrathin bP channels at a constant source-drain voltage $V_{\text{sd}} = 50 \text{ mV}$. In the passivated region we measure nearly symmetric n-type and p-type charge transport as discussed in the paragraph above. The on-off current ratio is 10^5 and is limited by the SiO_2 back gate leakage current. The I-V characteristic on the p-side, at negative V_g of both

the passivated and unprotected phosphorene exhibits small deviations from linearity, Figure 4.3.4(b). On the n-conduction side, at positive gate voltages, the I-V behavior of the passivated and unprotected channels is significantly different. A non-linear behavior is observed for the unprotected channel, while on the n-conduction side of the passivated phosphorene we measure linear I-V for V_{sd} up to 0.5 V, see Figure 4.3.4(c). At source-drain voltage above 0.5 V we observe current saturation and the FET exhibits a residual linear increase of I_{sd} with V_{sd} , which is not sensitive to the gate voltage.

The enhanced n-type charge transport and electron mobility, in addition to the the measured linear and saturation regime in the I-V characteristic at negative V_g shows the operation of the passivated ultrathin bP channel as an n-FET. We suggest that the transport properties of the passivated channel corresponds to the behavior of *pristine* ultrathin bP, while the properties in the unprotected phosphorene are affected by air exposure and the resulting degradation. We conclude that air-exposure of the bP leads to deterioration of n-type transport and significant hole doping. These results could be due to the formation of low-energy electron traps states as a result of degradation. Electron charge traps in phosphorene could be induced by oxygen defects as demonstrated in a theoretical study, or by adsorption of an oxygen/water redox couple which is known to degrade electron transport in carbon nanotubes.[68, 70]

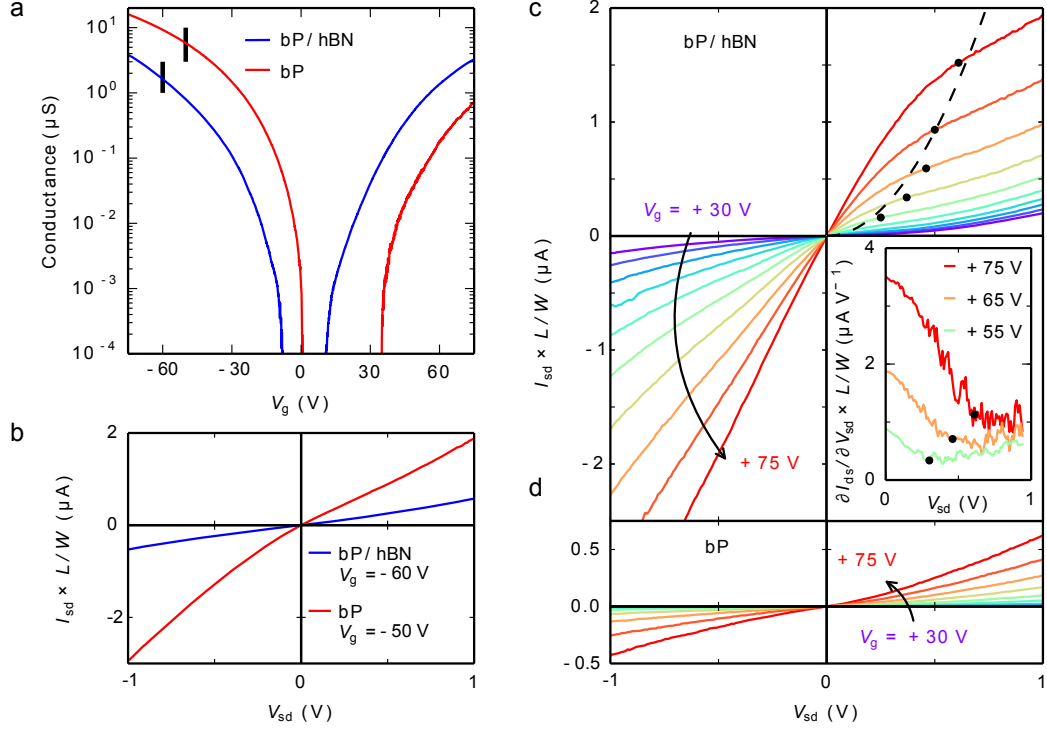


Figure 4.3.4: **(a)** Two-probe conductance against back gate voltage for sample #2 from the previous figure for the passivated (solid blue curve) and unprotected (solid red curve) channels at $T = 200$ K. **(b)** I-V behavior of the FET on the hole side for the passivated (solid blue curve) and unprotected (solid red curve) channel at gate voltages $V_g = -60$ V and $V_g = -50$ V. **(c)** Source-drain current (I_{sd}) against source-drain voltage (V_{sd}) for the hBN-passivated channel on the electron conduction side at V_g from +30 V to +75 V in steps of 5 V (solid curves). **(d)** I_{sd} versus V_{sd} for the exposed region on the electron conduction side at V_g from +30 V to +75 V in steps of 5 V.

In conclusion, in this section we demonstrated that van der Waals heterostructures of ultrathin bP with graphene or hBN, fabricated in an inert Ar gas environment, can be utilized to passivate the air-sensitive phosphorene. FET channels of the material which are exfoliated and fabricated with no exposure to air exhibit enhanced n-type charge conduction, which results in symmetric electron and hole transport. This leads us to the conclusion that the doped p-type behavior and the low n-type conduction in

unprotected phosphorene channels is caused by oxygen traps or chemical by-products of the oxidation upon exposure to ambient conditions. The transport properties measured here make pristine phosphorene one of few 2D semiconductor crystals for which ambipolar and nearly symmetric n-type and p-type charge transport has been demonstrated using a SiO₂ back gate and the same contact metal for both electron and hole injection.[71] The high electron and hole field effect mobilities, the large on-off current ratio at room temperature, and the nearly symmetric ambipolar behavior make ultrathin bP a candidate for CMOS-like digital logic applications.

4.4 Electrical Properties of Few-Layer bP on hBN

The results of this section are published in *Appl. Phys. Lett.* **106**, 083505 (2015), Rostislav A. Doganov, Steven P. Koenig, Yuting Yeo, Kenji Watanabe, Takashi Taniguchi, and Barbaros Özyilmaz.

In FETs based on 2D materials, like ultrathin bP or graphene, the charge transport is confined within a few-nanometer-thick conducting layer supported on a macroscopic substrate. The physical properties of the underlying base often significantly affect the transport in the atomic crystal and the overall performance of the FET device. For example, for the case of graphene it is known that the disorder (roughness) of standard SiO₂ wafers causes the formation of electron-hole puddles which limit the mobility in comparison to the intrinsic one.[24, 45] FET devices of atomically thin MoS₂ on PMMA have been reported to exhibit ambipolar transport different from what is observed on SiO₂. [72] An understanding of how the underlying substrate and processes such as annealing affect the transport properties of a 2D material is important in order to decouple the intrinsic material properties from those of the whole device including the substrate.

In this section the charge transport properties of few-layer bP are studied on an hBN substrate, which has lower roughness than SiO_2 and is free of dangling bonds and surface charge traps.[24] Being an atomically thin crystal itself, hBN is arguably the most important insulating substrate and gate dielectric for potential few-layer transparent flexible FETs and it has already been utilized to improve charge transport in graphene and MoS_2 FETs.[24, 73] Here we study the transport characteristics of annealed ultrathin bP on hBN and analyze the temperature dependence of the measured field-effect mobility. We find that the mobility in our exfoliated samples is limited by charged impurities (CI). We compare the sub-threshold behavior of ultrathin bP FET channels on SiO_2 and hBN and find that in situ vacuum annealing reduces the hole doping and improves the room temperature hysteresis of air-exposed ultrathin bP. This finding indicates that vacuum annealing at 400 K cleans oxidation and fabrication residues on the top surface of phosphorene surface.

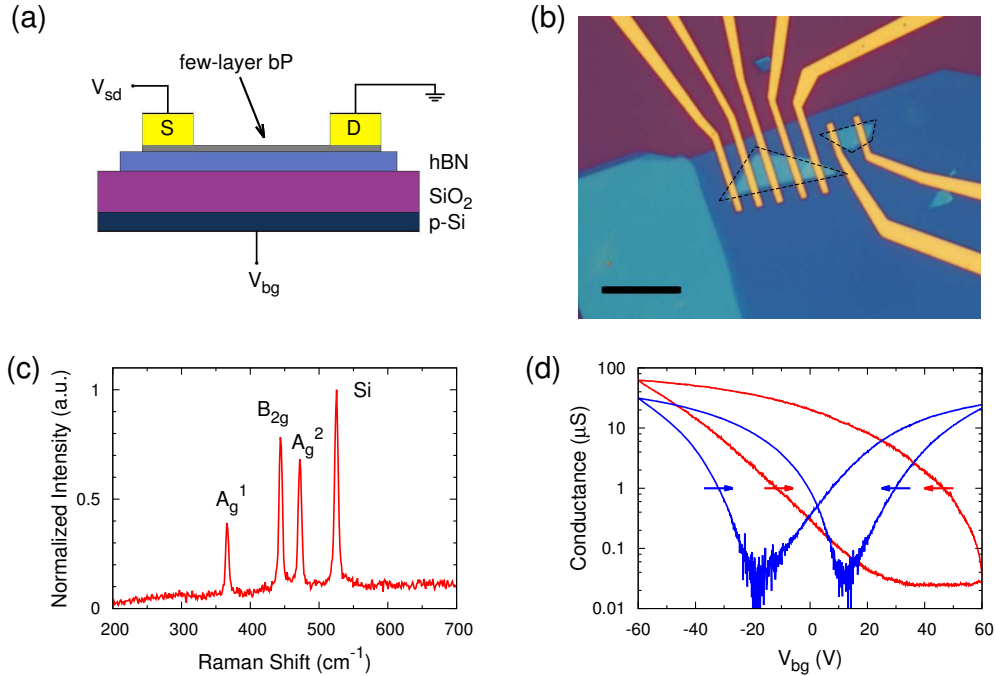


Figure 4.4.1: **(a)** Device schematic of a hBN/bP heterostructure. **(b)** Micrograph of two devices with bP thickness of 10 nm and 8 nm on top of 20 nm hBN. The ultrathin bP is outlined with black dashed lines. Scale bar is 10 μm . **(c)** Raman spectrum of the studied phosphorene/hBN device. **(d)** Four-terminal conductance against gate voltage V_{bg} for an as-fabricated (red line) and vacuum-annealed (blue line) bP channel of thickness 10 nm at room temperature. The arrows show the back gate sweep direction. Reprinted from R.Doganov et al. *Appl. Phys. Lett.* **106**, 083505 (2015), with the permission of AIP Publishing.

We fabricate van der Waals heterostructures of few-nanometer-thick bP on hBN using the dry transfer technique described in section 3.2. Before transfer the exfoliated hBN crystals are annealed at 340^o C in Ar:H₂ gas mixture (9:1 ratio) and are scanned under AFM to check that the surface roughness is around 0.1 nm and below that of SiO₂. Electrodes to the ultrathin crystal are fabricated using EBL and thermal deposition of Ti+Au (5+80 nm), similarly to the device fabrication in the preceding two sections. A schematic of the van der Waals FET heterostructure and an optical micrograph of the device are shown in Figure 4.4.1(a)&(b). The optical contrast of

few-layer bP on hBN was found to be quite low so the crystal's fingerprint is verified using Raman spectroscopy after electrode deposition in Figure 4.4.1(c). Typical four-probe conductance versus gate voltage, V_{bg} , for a 10 nm thick bP crystal at room temperature is shown in Figure 4.4.1(d). We measure dominant hole transport with a conductance of up to 60 μ S at $V_{bg} = -60$ V; a significant hysteresis of about $\Delta V_{bg} \approx 60$ V; and no electron transport at positive back-gate voltage.

Vacuum annealing of the samples at 400 K for 60 min immediately before measurement drastically changes the transport behavior of the bP/hBN heterostructure. As plotted in Figure 4.4.1(d), after temperature treatment the hole doping of the device is reduced to almost zero, the electron transport for positive V_{bg} is enhanced, and the gate sweep hysteresis is reduced almost two times. Identical result after vacuum annealing are reproduced in few-layer bP on SiO₂. We attribute the changes in transport resulting from the 400 K in-situ annealing to removal of oxidation, which was shown to produce p-doping in section 4.3. Thus, when no protection in air is required, the in-situ vacuum annealing of the sample right before measurement provides an easy pathway to measuring the properties of pristine ultrathin bP.

The four-terminal conductance versus back gate voltage at a temperature, of $T = 190$ K for the bP/hBN heterostructure is plotted in Figure 4.4.2(a). The absence of gate voltage offsets due to the hysteresis or doping results in the trans-conductance curve being centered at $V_{bg} = 0$ V and leads to symmetric threshold voltage $V_{th} = \pm 22$ V for both hole and electron conduction. In order to demonstrate that linear conduction with V_{bg} can be obtained for both p-type and n-type conduction we plot $d\sigma/dn$ in Figure 4.4.2(b), where σ is the conductivity and n is an approximation for the charge carrier density from the capacitance of the gate, $n = V_{bg} C_g$, where $C_g = 6.8 \times 10^{10} \text{ cm}^{-2} \text{ V}^{-1}$ is the capacitance for the 300 nm SiO₂ + 20 nm hBN back gate. From the linear conduction regime, $d\sigma/dn = \text{const.}$, we extract a field effect mobility

of $\mu_{\text{FE}} = 189 \text{ cm}^2\text{V}^{-1}\text{s}^{-1}$ for p-type transport (at $n_{\text{h}} = 4.8 \times 10^{12} \text{ cm}^{-2}$) and $\mu_{\text{FE}} = 106 \text{ cm}^2\text{V}^{-1}\text{s}^{-1}$ for n-type transport (at $n_{\text{e}} = 3.4 \times 10^{12} \text{ cm}^{-2}$). In Figure 4.4.2(b)&(c) we plot the measured the $I_{\text{sd}}-V_{\text{sd}}$ curves showing linear (ohmic) contacts for both the n-type and the p-type conduction. This indicates that both the valence and conduction band of bP can be accessed using Ti+Au contacts. This is consistent with the behavior observed in the passivated devices discussed in section 4.3.

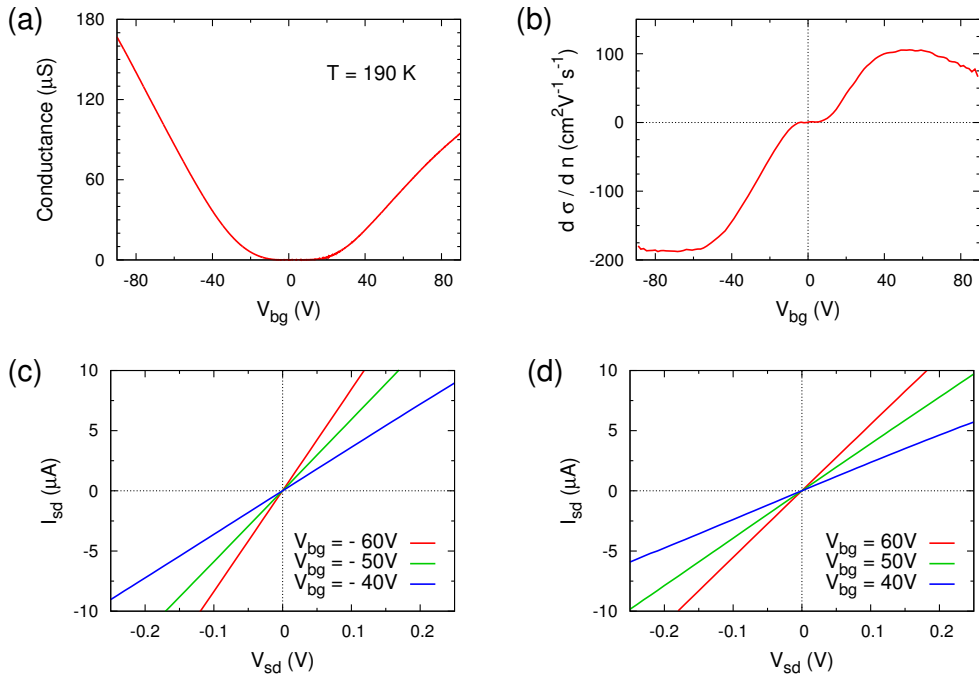


Figure 4.4.2: **(a)** Four-terminal conductance against gate voltage at $T = 190 \text{ K}$ for the 10 nm sample from the previous figure. **(b)** Derivative of the conductivity $\sigma(V_{\text{bg}})$ demonstrating linear conduction on both the hole and electron conduction sides. **(c)** I-V characteristic on the hole conduction side for V_{bg} from -40 V to -60 in steps of 10 V. **(d)** I-V characteristic on the electron conduction side for V_{bg} from 40 to 60 V in steps of 10 V. Reprinted from R.Doganov et al. *Appl. Phys. Lett.* **106**, 083505 (2015), with the permission of AIP Publishing.

Next we look at the temperature dependence of the electron and hole field effect mobilities which are plotted in Figure 4.4.3(a). There is an increase of mobility with decreasing temperature from around $170 \text{ cm}^2\text{V}^{-1}\text{s}^{-1}$ at 300 K to $210 \text{ cm}^2\text{V}^{-1}\text{s}^{-1}$ at 100

K. Below 100 K the mobility of our bP/hBN sample shows almost no dependence on temperature. For temperatures above 100 K we observe that the field effect mobility follows $\mu_h \propto T^{-0.25}$ for holes and roughly $\mu_e \propto T^{-0.5}$ for electrons. Thus, the measured dependence in the ultrathin samples is significantly different than $\mu \propto T^{-3/2}$ in bulk, see section 2.3 and section 4.1. Here the orientation of the exfoliated crystal and the transport direction were determined to be in the armchair direction, using polarization-resolved Raman spectroscopy.

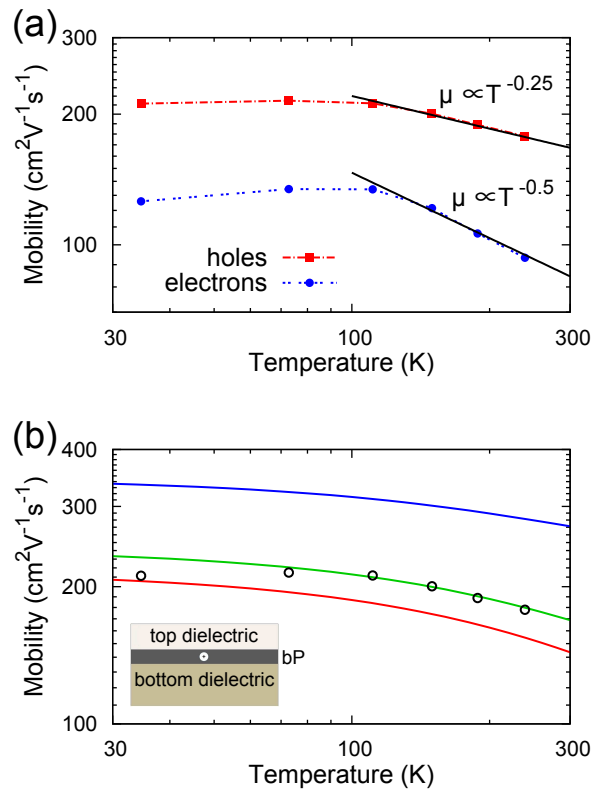


Figure 4.4.3: **(a)** Field effect mobility extracted from the linear conduction regime for holes (red squares) and electrons (blue circles) versus temperature. The solid black lines are fits at temperatures above 100 K **(b)** Numerical charge-impurity limited mobility obtained from with $n = 8 \times 10^{12} \text{cm}^{-2}$ and $N_i = 10^{13} \text{cm}^{-2}$ for different dielectrics: bP/SiO₂ (red), bP/hBN (green), and hBN/bP/hBN (blue). The black circles are the measured hole field effect mobility values from (a). The inset shows a schematic of the theoretical model. Reprinted from R.Doganov et al. *Appl. Phys. Lett.* **106**, 083505 (2015), with the permission of AIP Publishing.

The curve of the temperature dependence of the field effect mobility suggests that the transport is limited by charged impurities (CI), similarly to the case of early monolayer MoS₂ FETs.[74, 75, 76, 77] To study the effect of CI on the transport properties of 2D bP we adopt a theoretical model developed in Refs. [74, 76] to numerically calculate the mobility limited by CI. The theoretical model considers scattering from a Coulomb potential within a 2D semiconductor with vanishing thickness, which is “sandwiched” between two insulators, see the schematic in the inset of Figure 4.4.3(b). The dielectric constants of the two surrounding insulators and the thickness of the top dielectric can be varied. The characteristic temperature dependence of the mobility, saturating at low temperatures, comes from the screening of the Coulomb potential, which is highly temperature dependent and is expressed through the static charge polarizability of the carriers. For an anisotropic semiconductor with charge transport along one direction we can write

$$\mu = \frac{e}{\pi n^2 k_B T} \left(\frac{m_{eff}}{m_x} \right)^2 \int f(E)[1 - f(E)]\Gamma(E)^{-1} E dE \quad (4.4.1)$$

where n is the charge carrier density, $m_{eff} = (m_x m_y)^{1/2}$ is the average carrier mass in the plane, $f(E)$ is the equilibrium Fermi-Dirac distribution, and m_x, m_y are the carrier masses along the two anisotropic directions of the semiconductor. We find the orientation of the exfoliated crystal by measuring the angle-dependence the Raman spectrum as discussed in section 3.3. The momentum relaxation of the carriers for scattering off a Coulomb potential, $\Gamma(E)$ in Eq.4.4.1, is calculated from:

$$\Gamma(E) = \frac{N_i}{2\pi} \int d^2k |\phi_{|k-k'|}]^2 (1 - \cos \theta_{kk'}) \delta(E_k - E_{k'}) \quad (4.4.2)$$

with N_i is the impurity density, $\theta_{kk'}$ the angle of scattering between momenta k and k' . $\phi_{|k-k'|}$ is the screened Coulomb potential as derived in Ref.[74], $\phi_q = \frac{e^2 G_q(0,0)}{\epsilon_{2D}}$,

with $\epsilon_{2D} = 1 - e^2 G_q(0, 0) \Pi(q, T, E_F)$, $G_q = \frac{1}{(\epsilon_{tox}^0 \coth(qt_{ox}) + \epsilon_{box}^0)q}$, and

$$\Pi(q, T, E_F) = \int_0^\infty d\mu \frac{\Pi(q, 0, \mu)}{4k_B T \cosh^2\left(\frac{E_F - \mu}{2k_B T}\right)}, \quad (4.4.3)$$

where $\Pi(q, 0, \mu) = -\frac{gm_{\text{eff}}}{2\pi\hbar^2} \left(1 - \theta(q - 2k_F) \sqrt{1 - \frac{4k_F^2}{q^2}}\right)$, $\theta()$ is the Heavyside step function, $k_F = \sqrt{2m_{\text{eff}}\mu}/\hbar$, and $E_F = k_B T \ln\left(\exp\left(\frac{\pi\hbar^2 n}{2m_{\text{eff}}k_B T}\right) - 1\right)$. With given carrier density (n), impurity concentration (N_i), effective mass (m_{eff}), thickness of the top dielectric (t_{ox}), and dielectric constants of the two oxides (ϵ_{tox} and ϵ_{box}), the model can calculate the temperature dependent mobility.

The dielectric constants and thickness of the top dielectrics enter the calculation through $\phi_{|k-k'|}$, which is calculated assuming isotropic polarizability of the carriers in a semiconductor with effective mass $m_{\text{eff}} = (m_x m_y)^{1/2}$ (following the assumptions in Ref.[75]). For the effective masses we use the values measured in bulk bP, namely $m_x = 0.076 m_0$ and $m_y = 0.648 m_0$. [50] In Figure 4.4.3(b) we plot the calculated results for mobility against temperature assuming $n = 8 \times 10^{12} \text{ cm}^{-2}$ and $N_i = 1.1 \times 10^{13} \text{ cm}^{-2}$ (those parameters give mobility values close to the measured ones). The assumed carrier concentration $n = 8 \times 10^{12} \text{ cm}^{-2}$ is approximately 70% higher than the concentration expected from the capacitive model. This disagreement is attributed to the simplicity of the used scattering model which considers isotropic static polarizability and absolutely neglects intrinsic phonon scattering and phonon scattering between the substrate and the semiconductor. Quantitative disparities could also come from uncertainty in the effective masses in ultrathin bP, which could be different from those in the bulk. In spite of these limitations, we observe that overall the theoretical model provides a good qualitative (and agreeable quantitative) agreement with the measurement. In Figure 4.4.3(b) we further show theoretical curves for 2D bP on standard SiO_2 with vacuum as a top dielectric, as well as for a hBN/bP/hBN heterostructure

calculated by changing the dielectric constants and keeping the carrier concentration and impurity density unchanged. We find that the hBN substrate contributes to a higher mobility and the full sandwiching with hBN on both sides would result in additional improvement of the mobility limited by CI. The numerical calculations are performed in *Mathematica* by the code attached in the Appendix.

To further explore the role played by the hBN we also measure annealed bP devices on SiO₂ and directly compare with regions of the crystal on hBN, see inset of Figure 4.4.4. Vacuum annealing of bP on SiO₂ at 400 K for 60 min results in improvement of the transport properties identical to those observed on hBN. In addition to the enhancement in mobility, in the bP/hBN device we also measure an improved sub-threshold slope, $S = dV_{bg}/d\log I_{sd}$. For the bP/hBN FET we obtain a sub-threshold swing of $S \approx 1.5$ V/dec, compared to $S \approx 2.1$ V/dec on the SiO₂ wafer. We attribute this difference to the superior quality of the bP/hBN interface, as has been argued for MoS₂ FETs on hBN.[73] The overall large values of S , when compared to the ideal thermal limit of 60 mV/dec at room temperature, are due to the thick (300 nm) SiO₂ back-gate dielectric.

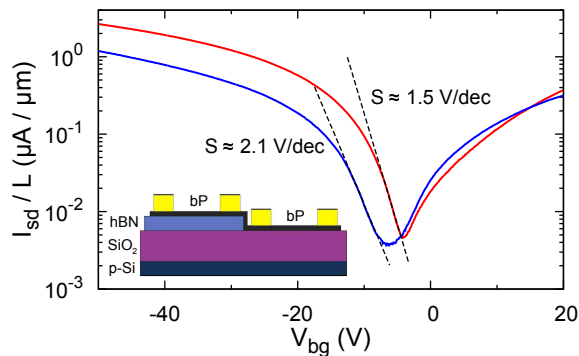


Figure 4.4.4: Source-drain current, I_{sd} , against back gate voltage, V_{bg} , at fixed source-drain voltage of $V_{sd} = 0.1$ V for vacuum annealed few-layer bP on hBN (red curve) and on SiO₂ (blue curve). The black dashed lines show the sub-threshold slope S . The inset shows the geometry of the measured device. Reprinted from R.Doganov et al. *Appl. Phys. Lett.* **106**, 083505 (2015), with the permission of AIP Publishing.

In summary, in this section we studied the electrical transport characteristics of few-layer bP on an hBN substrate. After in situ vacuum annealing we measure intrinsic semiconductor behavior with negligible hole doping, smaller hysteresis at room temperature, and symmetric electron and hole transport. The linear I - V curves at positive back gate voltages confirm that Ti+Au contacts efficiently inject both holes and electrons into few-layer bP. We used a theoretical model to describe the observed temperature dependence of the field effect mobility taking into account scattering from CI. We found agreement between the measurements and the theoretical model which points out that improved crystal quality, with lower impurity density, should allow for higher mobility in bP.

4.5 N-type Doping of Few-Layer Phosphorene Using Metal Adatoms

The results of this section are published in *Nano Lett.* **6**, 2145 (2016), Steven P. Koenig, Rostislav A. Doganov, Leandro Seixas, Alexandra Carvalho, Jun You Tan, Kenji Watanabe, Takashi Taniguchi, Nikolai Yakovlev, Antonio H. Castro Neto, and Barbaros Özyilmaz.

In the previous sections it was shown that degradation of exfoliated bP in ambient air contributes to the unintentional p-doping of the crystal. It was also demonstrated that the passivation with a chemically-stable 2D material (like graphene and hBN), or vacuum annealing at 400 K, enhance the n-type transport. Furthermore, from the measured trans-conductance curves in Figure 4.4.1 and 4.4.2 it is seen that the on-state conductance for electrons and holes is almost equal. This observation is also consistent with the fact that bP exhibits almost equal carrier effective masses in the

conductance and valence band. These characteristics make few-layer bP a promising semiconductor for CMOS applications, which require both a p-FET and an n-FET in the same parent material. In Table 4.1 we show the effective carrier masses of Si, Ge, GaAs, and few-layer bP. From the known conventional bulk semiconductors only Si shows a close match of the two values (about 5 %) and intrinsic bP also exhibits very low difference between the two carrier masses (around 8%). It should therefore be possible to fabricate well-balanced CMOS-like devices if there is a reliable method to control the threshold voltage and tune bP to operate either as an unipolar p-FET or an unipolar n-FET. In this section we show that functionalization of few-layer bP with Cu adatoms can change the doping of the channel and shift the threshold voltage, without degrading the electronic properties.

	Si	Ge	GaAs	bP
m_e (m_0)	1.09	0.55	0.067	0.083
m_h (m_0)	1.15	0.37	0.45	0.076

Table 4.1: Comparison of the effective carrier mass for electrons and holes of some common semiconductors. [78]

Before we look into the experimental results it is instructive to briefly compare the situation with the TMDC semiconductors. MoS₂, WS₂, and other TMDCs have a strong natural propensity toward unipolar FET operation. For example, MoS₂ has a strong tendency to be n-type due to a low-lying valence band and native defects such as sulfur vacancies.[47, 79, 80] So far WSe₂ is the only TMDC semiconductor that exhibits nearly symmetric transport, although it has proven difficult to achieve low contact resistance for both electron and hole transport. Attempts to control the carrier type in 2D TMDCs by work function engineering are not very practical, while strategies using substitutional doping, as in MoS₂:Nb have not resulted in good electronic quality for the complementary carrier, because of the detrimental effect of

defects (dopants).[81]

We begin by performing DFT calculation for the electronic structure of bP combined with Cu adatoms. The DFT calculations were performed by Leandro Seixas, Dr Alexandra Carvalho, and Prof Castro Neto, and were obtained using a SIESTA package.[82] They calculated the effect of a Cu adatom on the band structure of four-layer bP. An illustration of the two dopant geometry referred to as Cu-ad a is shown in Fig.4.5.1(a). The Cu-ad was found to have large binding energy of E_b [Cu-ad] = - 2.62 eV. The respective band structure is shown in Figure 4.5.1(c). The DFT calculation shows that the Cu adatom is strongly bonded to the phosphorene layer and result in a significant electron doping of the crystal, while not causing any local DOS in the band gap or reduction of the effective carrier mass in the bands.

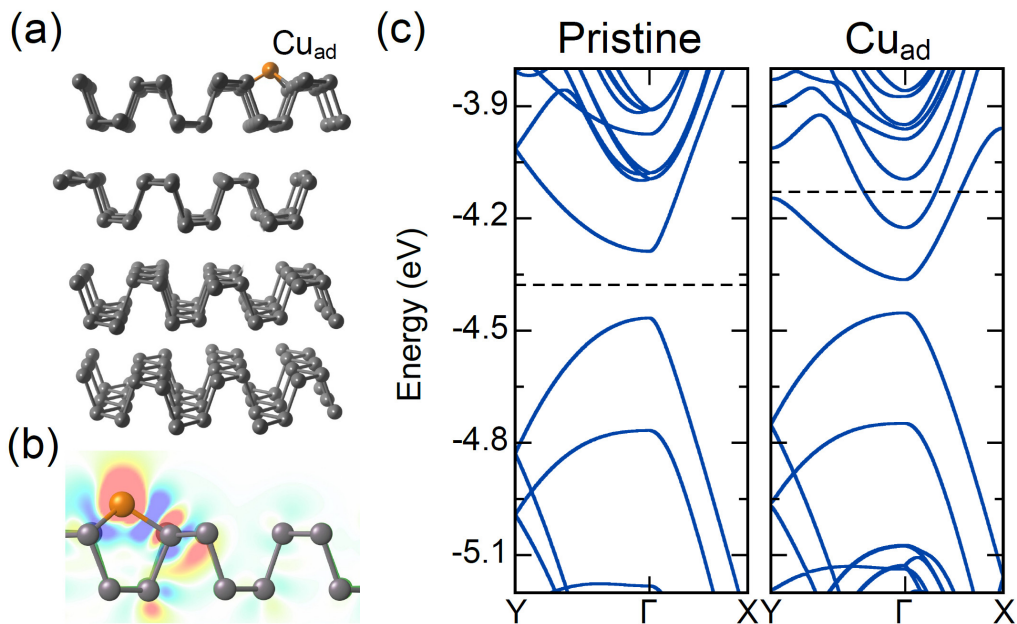


Figure 4.5.1: **(a)** Schematic drawing of the two defects studied here: surface adsorbed Cu_{ad} and interstitial, Cu_{int} . **(b)** Calculated charge density difference of the Cu_{ad} . The red and blue regions refer to electron depletion ($\Delta\rho = -2 \times 10^{-3} \text{ e/a}_0^3$) and accumulation ($\Delta\rho = +2 \times 10^{-3} \text{ e/a}_0^3$), respectively. **(c)** DFT band structure of pristine four-layer bP, four layer bP with adsorbed Cu, (Cu_{ad}), and four layer bP with interstitial Cu (Cu_{int}). The dashed line indicates the Fermi level for each case. The energies are with respect to the vacuum level. All DFT calculations were performed by Leandro Seixas, Alexandra Carvalho, and Antonio Castro Neto. Reprinted with permission from Steven P. Koenig, Rostislav A. Doganov, et al. *Nano Lett.* **6**, 2145. Copyright 2016 American Chemical Society.

Next we examine in more detail the band structure in Fig.4.5.1(c). The metal dopants are seen to donate one electron to the 2D crystal and to shift the Fermi level towards the conduction band. The large shift of the Fermi energy in the calculations of Figure4.5.1(c) is because of the the relatively small crystal cell used in the numerical computation, which translates into a very high Cu adatom concentration in a macroscopic crystal. The electron donated by the Cu atom is seen to originate from its 4s electronic shell, resulting in a closed-shell Cu^+ ion. Fig.4.5.1(b), shows

the difference in charge density between the combined bP + Cu_{ad} system ($\rho_{\text{Cu} + \text{bP}}$), pristine bP (ρ_{bP}), and the isolated Cu atom (ρ_{Cu}), i.e. $\Delta \rho = \rho_{\text{Cu} + \text{bP}} - \rho_{\text{bP}} - \rho_{\text{Cu}}$.

Here it is worthwhile to briefly compare the situation to graphene and TMDCs. It is established that these materials are chemically more stable and nonreactive than bP. However, this also reduces the ability to dope and functionalize them using adatoms. It is known that adsorption energy of adatoms on graphene is small, which can lead to their movement on the surface and easy de-adsorption upon heating. In this respect, the higher reactivity of few-layer bP is an advantage when it comes to the ability to modulate the crystal's properties using strongly-bonded adatoms.

Next we turn to the experimental section and attempt to introduce a small amount of Cu adatoms and study how they affect the charge transport measurements. The most direct way to deposit a small amount of Cu on the crystal surface is by thermal evaporation. However, as shown in Figure 4.5.2, we find that thermal deposition makes the Cu cluster in nanometer-sized dots. In order to avoid this we tried depositing a small amount of Cu using a DC magnetron sputtering system. We use a Cu source with a 2 inch (5.08 cm) diameter and deposit for 1 sec at 60W applied power and 2 mTorr Ar gas pressure. AFM measurements after deposition show that there are no clusters on the bP surface and the AFM-measured roughness, $R = 0.193$ nm, is similar to that of an untreated crystal, see Figure 4.5.3(a). In order to obtain direct experimental evidence for the presence of metal adatoms on the crystals, the Cu-treated samples were characterized by collaborators using x-ray photo-electron spectroscopy (XPS) and time-of-flight secondary ion mass spectroscopy (ToF-SIMS).

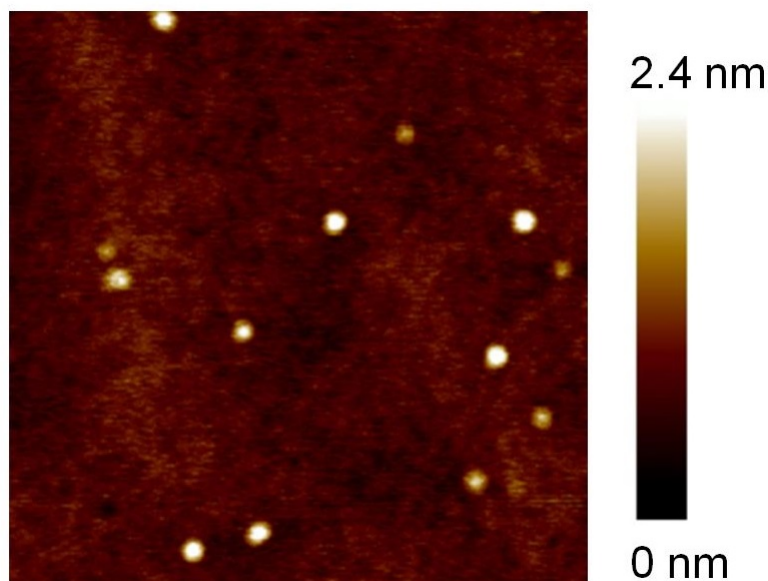


Figure 4.5.2: AFM scan of a 15-nm-thick bP crystal with Cu deposited by thermal evaporation. The image reveals clustering of Cu atoms on the surface (white dots). The scan size is 600 nm x 600 nm .

XPS is surface-sensitive tool for bulk samples that can detect elemental composition in the range of 1 per 1000.[83] The XPS measurements were performed in the Materials Science and Engineering Department at NUS on bulk crystals surfaces that allow a large spot size for performing XPS. Cu was deposited on a piece of bulk bP under the same conditions as the exfoliated samples. A control sample with no Cu deposition was also sent for characterization. The returned XPS spectra in the region between 925 eV and 965 eV are shown in Figure 4.5.3(b). The bulk sample treated with Cu shows clear peaks at 932 eV and 954 eV which can be attributed to the Cu $2p_{3/2}$ and Cu $2p_{1/2}$ shells.[84] The control sample does not show any peaks in this region. Furthermore, the XPS facility allows to easily perform supplementary ultraviolet photo-electron spectroscopy (UPS) of the sample. UPS has been shown to be a good tool for extracting the work function of a material.[85] In Figure 4.5.3(c) we plot the onset energy for the secondary photo-electrons, also referred to as the secondary

electron cutoff (SECO). The SECO can be used to extract the work function, because it corresponds to the vacuum level of the sample with respect to the Fermi energy (the energy at which the first electron escape the material). The cut-off in Figure 4.5.3(c) confirms a decrease in the work function of the surface by $\Delta E = 0.15$ eV after Cu deposition.

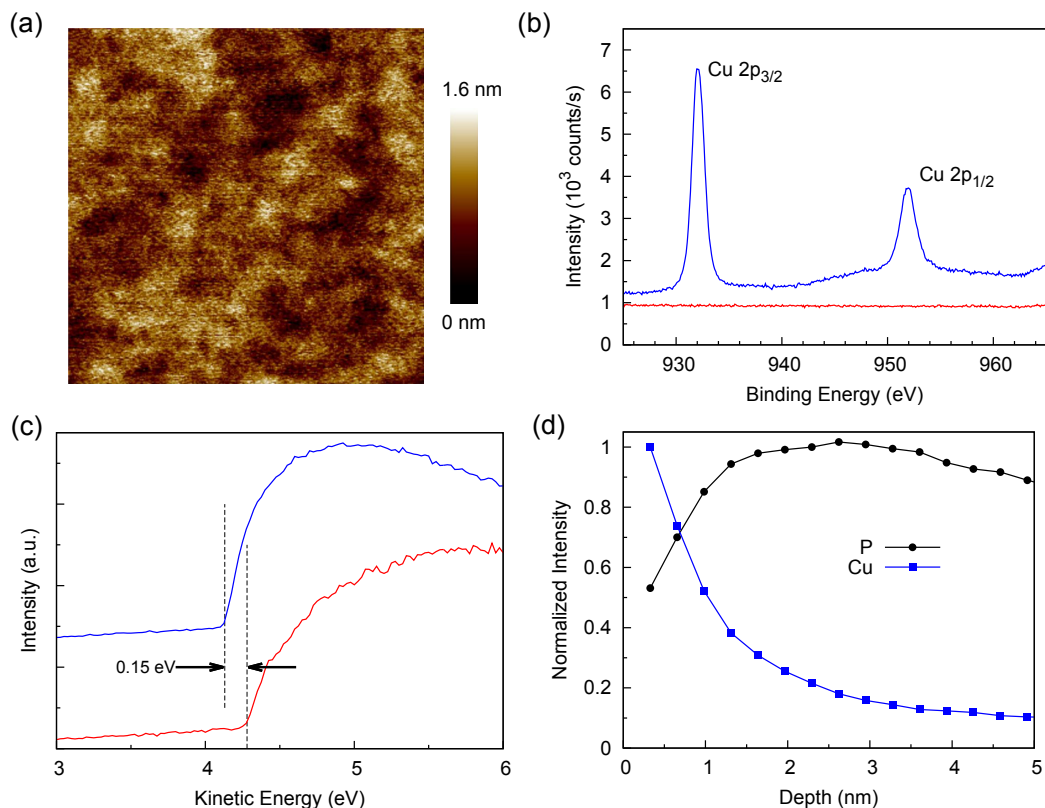


Figure 4.5.3: **(a)** AFM scan of a 7.5 nm thick bP crystal after sputtered deposition of Cu adatoms. AFM scan size is 750 nm \times 750 nm. **(b)** XPS spectra of bulk bP with (blue) and without (red) Cu sputtering treatment. **(c)** UPS spectra of bulk bP with (blue) and without (red) Cu sputtering. The dashed lines show the SECO. **(d)** ToF-SIMS of exfoliated bP treated with sputtered Cu. The black and blue symbols show the intensity of the ToF-SIMS signal versus sample depth for the P and ^{63}Cu ions, respectively. The signal is normalized to the maximum measured intensity for the particular ion. The XPS and UPS measurements were performed by staff at the Materials Science and Engineering Department in NUS. The ToF-SIMS measurement was performed by Dr Nikolai Yakovlev in IMRE, Singapore. Reprinted with permission from Steven P. Koenig, Rostislav A. Doganov, et al. *Nano Lett.* **6**, 2145. Copyright 2016 American Chemical Society.

The XPS measurements can confirm the presence of a small amount of Cu, however photo-electrons can be excited from anywhere between 0 to 10 nm depth. The measurements were also performed on bulk crystals with a spot size much larger than a typical exfoliated crystal. In order to measure the depth distribution of Cu we turn to ToF-SIMS which was done by Dr Nikolai Yakovlev in the Institute for Materials Science and Engineering (IMRE) in Singapore. A wafer with exfoliated bP which has undergone Cu deposition using the same sputtering conditions was sent for analysis. The SIMS technique focuses a 25kV primary beam of Bi ions onto a thin exfoliated crystal. The primary beam slowly mills down the sample and in the process ejects secondary ions from the crystal. The secondary ions are analyzed using a mass spectrometer. Because of the milling effect, the measurement is time-of-flight and a time profile of the extracted ions can be measured. The time profile is converted into a depth profile by knowledge of the approximate milling rate. In Figure 4.5.3(d) we show the returned results for the depth profile of the ^{63}Cu ion and the P ion. The element- and energy-dependent cross section for ejection of secondary ions makes SIMS unsuitable for absolute measurements (and composition comparison), so the curve for each ion is normalized to the maximum measured intensity (for that particular ion). We observe that the ^{63}Cu ions exhibit a maximum at the top-most surface (0 nm depth) and the intensity quickly decreases with depth as the crystal is milled away. The curve for the P ions shows a different profile. The initial value is lower, which we interpret as part of the surface being covered with Cu atoms, and then the intensity peaks at around 3 nm and slowly starts decreasing, which we attribute to the finite thickness of the exfoliated bP crystal. From the ToF-SIMS results we conclude that the majority of the deposited Cu remains at the top surface of the ultrathin bP crystal. We note that in the following transport characterization the devices are annealing prior to measurement (and after Cu deposition), in order

to remove any residual oxidation and p-type doping resulting from the transportation and loading of the devices. The samples studied in ToF-SIMS, on the other hand, were not annealed in vacuum prior to the SIMS measurement. We don't expect that the annealing step changes the depth profile of the deposited Cu in bP, but this has not been experimentally tested by us and the transport samples and SIMS samples might not be comparable vis-a-vis.

Having established the presence of a small amount of Cu deposited by the described sputtering deposition, we now turn to study how this affects the charge transport properties. First we perform a direct comparison on a single sample before and after Cu deposition. In this section we use bulk bP crystals purchased from "HQ graphene", which were found to exhibit higher mobility when exfoliated. The device consists of 10 nm bP transferred on top of a 30 nm hBN crystal and contacted with 5 nm Au and 70 nm Au. An optical image, AFM scan, and height profile of the device are shown in Figure 4.5.4(a-c). Prior to the first characterization the sample is annealed in the measurement probe for 1 hour at 400 K under high vacuum ($<5 \times 10^{-7}$ Torr) in order to remove p-doping arising from degradation (see section 4.4). The trans-conductance curve shown in Figure 4.5.4(d) in red is characteristic of pristine bP and is similar to the measurement of annealed bP in the previous section. The sample exhibits a hole mobility of $\mu_{\text{FE}} = 690 \text{ cm}^2\text{V}^{-1}\text{s}^{-1}$ at room temperature which increases to $\mu_{\text{FE}} = 1780 \text{ cm}^2\text{V}^{-1}\text{s}^{-1}$ below 50 K, as shown in Figure 4.5.4(e). Hole mobilities are extracted at a carrier concentration of $n_{\text{h}} = 3.0 \times 10^{12} \text{ cm}^{-2}$. The obtained mobility for electrons prior to Cu treatment is $\mu_{\text{FE}} = 340 \text{ cm}^2\text{V}^{-1}\text{s}^{-1}$ at 300 K and reaches $580 \text{ cm}^2\text{V}^{-1}\text{s}^{-1}$ at 150 K (extracted at $n_{\text{e}} = 3.2 \times 10^{12} \text{ cm}^{-2}$).

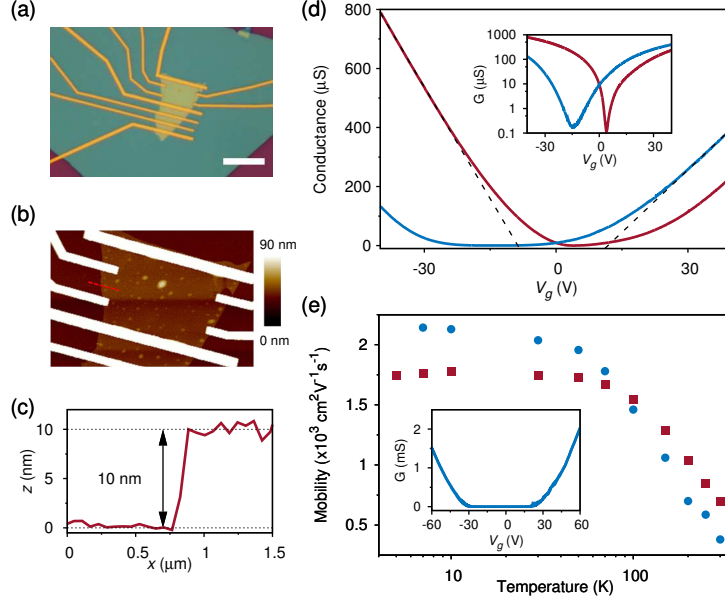


Figure 4.5.4: **(a)** Optical image of a 10-nm-thick bP crystal on top of hBN measured before and after Cu deposition. The scale bar is $10 \mu\text{m}$. **(b)** AFM image of the channel and **(c)** a line cut showing the AFM height. The AFM image is $16 \mu\text{m}$ wide. **(d)** Four-point conductance versus gate voltage, V_g , at room temperature before (red) and after (blue) Cu doping. The inset shows the same data on a logarithmic scale. The black dashed lines show the fits used for extracting the mobility. **(e)** Temperature dependence of the hole field effect mobility before Cu doping (red symbols) and the electron mobility after Cu doping (blue symbols). The inset shows the conductance versus back-gate voltage after Cu doping at $T = 7 \text{ K}$. Reprinted with permission from Steven P. Koenig, Rostislav A. Doganov, et al. *Nano Lett.* **6**, 2145. Copyright 2016 American Chemical Society.

After the first transport measurement the sample is brought to the sputtering system for Cu deposition. Then it is loaded back in the measurement probe and annealed at 400 K for 1 hour, in order to reduce any potential p-doping that might have resulted from the temporary exposure of the sample to air. The conductance of the channel versus gate voltage after Cu doping is plotted together with the measurement of the untreated sample in Figure 4.5.4(d) in blue. We see a shift of the minimum conductance towards negative gate voltages and increase in the n-type conduction (at positive V_g), which we attribute to electron doping by the Cu. The electron mobility

increases in comparison to the untreated sample to $380 \text{ cm}^2\text{V}^{-1}\text{s}^{-1}$ at 300 K and to $2140 \text{ cm}^2\text{V}^{-1}\text{s}^{-1}$ at $T = 7 \text{ K}$ (at $n_e = 3.2 \times 10^{12} \text{ cm}^{-2}$). The extracted hole mobility is slightly reduced to $570 \text{ cm}^2\text{V}^{-1}\text{s}^{-1}$ at room temperature ($n_h = 3.0 \times 10^{12} \text{ cm}^{-2}$). In Figure 4.5.4(e) we plot the measured temperature-dependent field effect mobility for electrons. At low temperatures the values reaches $2000 \text{ cm}^2\text{V}^{-1}\text{s}^{-1}$ which confirms that the Cu doping does not introduce a significant amount of additional impurities (scatterers) and preserves the electronic quality of the crystal. This is the highest electron mobility that we have measured in few-layer bP. From the logarithmic plots of the conductance before and after the Cu treatment (Figure 4.5.4(e), insert) we can compare the position of the conductance minima. We extract an average gate voltage shift on the hole and electron side of $\Delta V_g = -18.1 \text{ V}$ which, within the simple capacitor model, translates to the addition of $12.7 \times 10^{11} \text{ electrons/cm}^2$ by the Cu. Similarly to section 4.3, in this experiment we did not determine the crystal orientation and transport direction. However, the transport characterizations before and after Cu were always performed on the same channel, so the unknown transport direction could only affecting the absolute values of the mobility but not the changes attributed to Cu deposition.

We point out that the adatom doping of phosphorene is not specific to Cu. There are theoretical studies which predict that other metal elements also induce a shift in the Fermi level of monolayer bP.[86, 87] Our sputtering system allows us to easily test this for Au and Ag, which are readily available in the system. In Figure 4.5.5 we show the measured effect for these metal dopants and observe that Au induces a small p-doping, while Ag induces small n-type doping which is consistent with the theoretical results. This suggests that the introduction of metal adatoms on phosphorene is a versatile method which could be further optimized to produce both p- and n-type shifts.

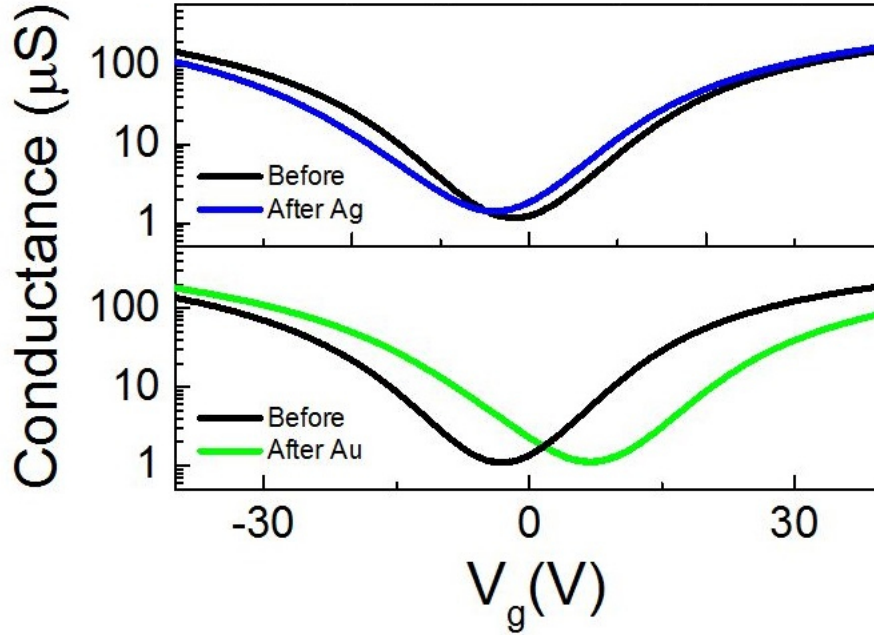


Figure 4.5.5: Conductance versus gate voltage before and after deposition of Cu, Ag, and Au. Cu and Ag serve as electron dopants while Au is a p-dopant.

The ability to change the threshold voltage opens the opportunity to fabricate two FETs on the same channel and find a V_g interval such that one FET is in the on-state when the other is off, and vice versa. The two FETs could then be connected in a CMOS configuration to form a voltage inverter. To this end, we transfer a heterostructure consisting of 6 nm multilayer graphene on the bottom, a 30 nm hBN crystal in the middle, and a 6 nm thick bP on top. The graphene will serve as a metal gate, the hBN is the gate dielectric, and the ultrathin bP is the semiconductor channel. After fabrication of the metal electrodes we perform an additional EBL step and expose the area between some pairs of contacts. The sample is then loaded into the sputtering system and Cu adatoms are selectively deposited only on some channels, while the rest of the device is protected by the PMMA resists. This allows

us to have two FETs with shifted threshold voltages, which are on the same ultrathin bP crystal. This is similar to Si CMOS technology and makes the process applicable on larger scale. An optical image, AFM scan, and line cut of the device are shown in Figure 4.5.6(a-c). By measuring the individual FETs in a two-probe configuration we observe that for V_g between 0 and +2V the untreated channels behave as p-FET, while the Cu-functionalized channel operates as an n-FET, Figure 4.5.6(d)(f) and (e)(g), respectively. The insets show the I-V curves which confirm that the devices operate as FETs with current-saturation regime.

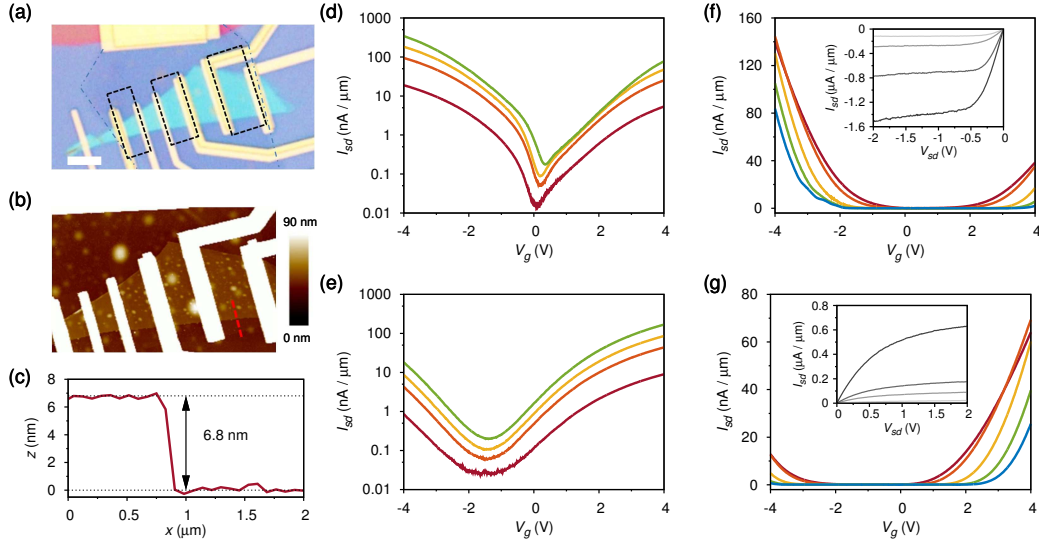


Figure 4.5.6: **(a)** Optical image of a device consisting of 6-nm-thick multilayer graphene / hBN/ and 6-nm-thick bP. The black boxes outline the areas in which Cu was deposited. The scale bar is $5\ \mu\text{m}$ **(b)** AFM image and **(c)** line cut taken from **(b)** showing the flake thickness. **(d,e)** Two-point source-drain current, I_{sd} , versus gate voltage, V_{g} , at room temperature for V_{sd} values of 10, 50, 100, and 200 mV for the untreated bP p-FET and Cu-doped bP n-FET, respectively. **(f)** Two-point source drain current, I_{sd} , versus gate voltage, V_{g} , at V_{sd} of 10 mV of the untreated bP p-FET at temperatures of 250, 200, 100, 50, and 30 K with the colors going from red to blue. **(g)** Two-point source drain current, I_{sd} , versus gate voltage, V_{g} , at V_{sd} of 10 mV for the Cu doped n-FET at temperatures of 250, 200, 100, 50, and 30 K, with the colors going from red to blue. The insets shows the $I_{\text{sd}}-V_{\text{sd}}$ characteristics at 300 K for V_{g} from 0.5 V (lightest gray) to 2.5 V (darkest gray) in steps of 0.5 V. Reprinted with permission from Steven P. Koenig, Rostislav A. Doganov, et al. *Nano Lett.* **6**, 2145. Copyright 2016 American Chemical Society.

Now we can connect the two complementary FETs in a voltage-inverter configuration, as illustrated in Fig.4.5.7(a)&(b). A constant positive voltage of $V_{\text{DD}}=+2\text{V}$ is applied on the source side of the p-FET. The drain of the n-FET is grounded and the voltage on the contact in the middle is measured while sweeping the gate, V_{in} , from 0 V to +2 V. As V_{in} is being swept across 0 V to 2 V, the measured voltage at the middle terminal, V_{out} , changes from 1.99 V at $V_{\text{in}}=0\text{ V}$ to a low-state value of about 0.04 V at $V_{\text{in}}=2\text{ V}$. If we use 0 V to depict a Boolean “0” and +2 V for a “1”,

we see that the device works a logical inverter.

An important figure of merit for an inverter is the gain, which characterizes how quickly the state changes from one value to the other. It is defined by $g = |dV_{\text{out}}/dV_{\text{in}}|$, and can be extracted by numerical differentiation of the data. We plot the result in Figure 4.5.7(c) together with the V_{out} versus V_{in} characteristic. We observe a maximum value of $g=46$. Further important figures of merit are high-state and low-state noise margins defined as $NM_{\text{H}}=V_{\text{OH}} - V_{\text{IH}}$ and $NM_{\text{L}}=V_{\text{IL}} - V_{\text{OL}}$, respectively. Here V_{IL} (V_{IH}) is the smallest (highest) input voltage where $g=1$, and V_{OL} (V_{OH}) is the smallest (largest) output voltage with $g=1$. The extracted margins for the presented device are $NM_{\text{H}} = 0.30 \times V_{\text{DD}}$ and $NM_{\text{L}} = 0.37 \times V_{\text{DD}}$. This means that the device is immune to noise in the logical “0” and “1” of up to 30% of V_{DD} . For example, if there is a cascade of many inverters, and the first one receives a noisy signal with $V_{\text{in}} = 1.5$ V as a logical “1” (instead of of $V_{\text{in}} = 2.0$ V), the noise will not cause a wrong binary value in the following inverters, and the voltage error will eventually drop to zero after several inverting stages.

A further important figure of merit for an inverter is the current flowing through the device, I_{DD} . The main advantage of the complementary transistor configuration is that one of the FETs is always in the off -state and there is very little current flow through the inverter. I_{DD} , plotted in the inset of Figure 4.5.7(c), is less than 0.5 μA at all input voltages and peaks around the switching voltage of $V_{\text{in}}= 1$ V when both FETs are not fully in the off state. We see a second increase of I_{DD} towards $V_{\text{in}} = 2\text{V}$, which is due to the fact the p-FET (the untreated bP channel) exhibits a finite n-type conduction at $V_{\text{g}}= 2$ V, as can be seen from Figure 4.5.6(d). The device was also tested at an elevated temperature of 330 K, which is important for practical devices in an integrated circuit which usually operate above room temperature because of heating. Measurements over the course of 10 days, during which the device was kept in

the measurement probe at room temperature in vacuum, do not show significant loss of performance, see Figure 4.5.8(a)&(b). At elevated temperatures the inverter gain decreases because the switching characteristics become less steep with gate voltage (decreased sub-threshold slope). Returning the device to room temperature recovers the initial gain values, Figure 4.5.8(c)&(d).

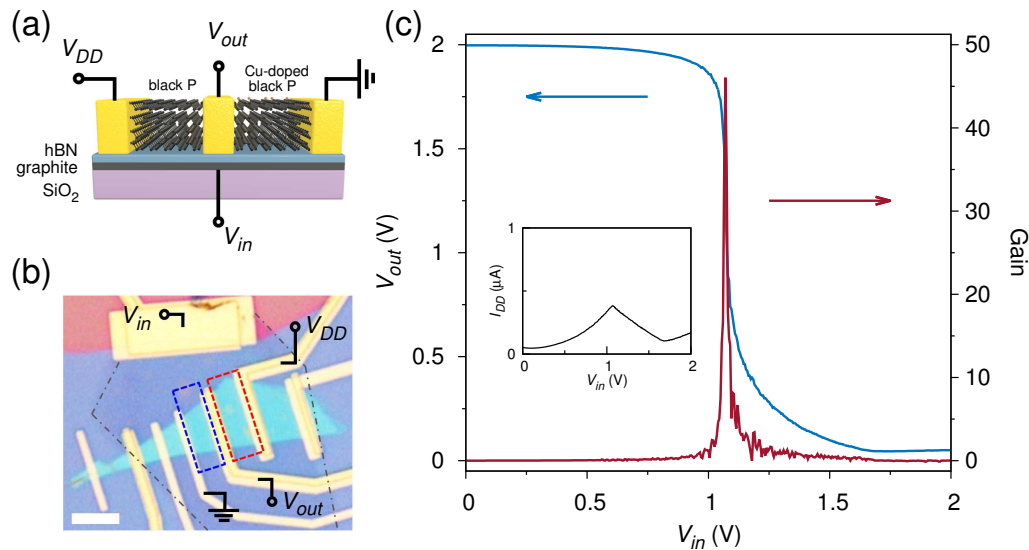


Figure 4.5.7: **(a)** Schematic of the bP inverter fabricated using an untreated p-FET channel and a Cu doped n-FET channel. The heterostructure consist of a 6 nm thick graphite bottom gate, used as V_{in} , a 30 nm thick hBN gate dielectric, and a single 7 nm bP flake with Ti/Au contacts, all on an SiO₂ substrate. **(b)** Optical image of the device. The gray dash-dot line outlines the graphite bottom gate, and the red and blue boxes mark the p-FET channel and Cu doped n-FET channel, respectively. The scale bar is 5 μm . **(c)** Output voltage, V_{out} , versus input voltage, V_{in} , of the inverter at $V_{DD} = 2\text{ V}$. The inverter gain, g , versus V_{in} is shown in red on the right axis. The inset shows the device current, I_{DD} , versus V_{in} . Reprinted with permission from Steven P. Koenig, Rostislav A. Doganov, et al. *Nano Lett.* **6**, 2145. Copyright 2016 American Chemical Society..

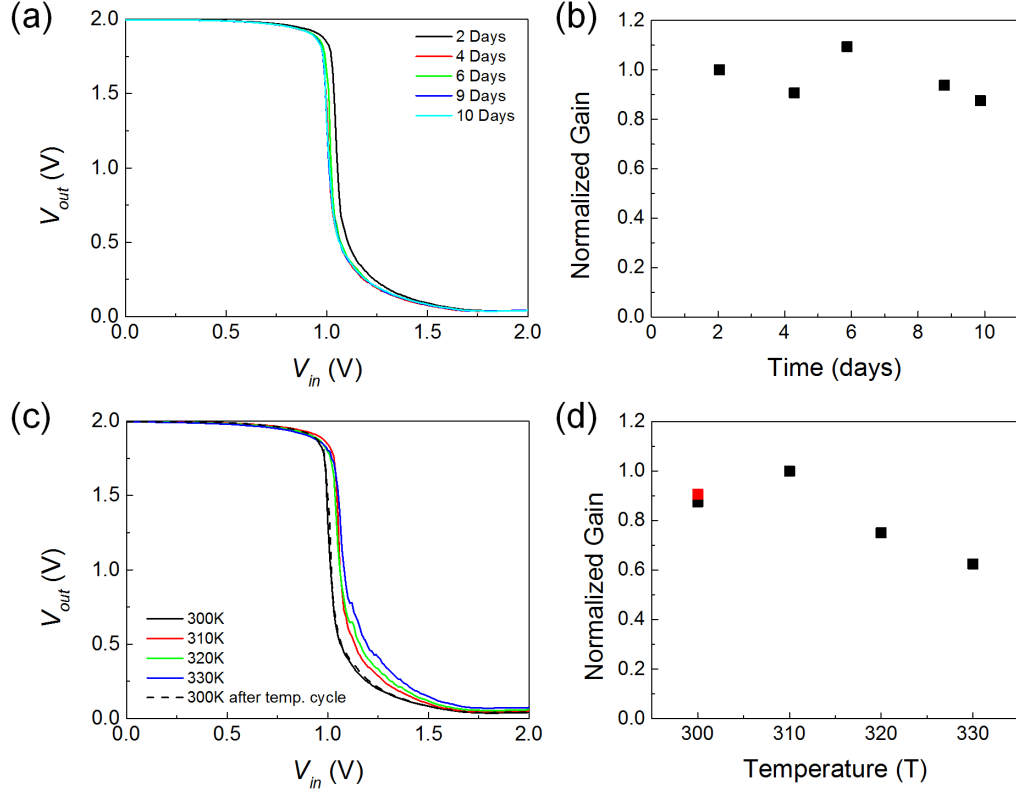


Figure S8

Figure 4.5.8: Temperature and time stability of the operation of the inverter. (a) Inverter V_{out} versus V_{in} and (b) extracted gain during 10 days in vacuum. (c) Inverter V_{out} versus V_{in} and (d) extracted gain elevated temperatures up to 330 K. The red point is the inverter gain after the device was measured at 330K and then cooled down to 300K. The values are normalized to the initial inverter gain.

In summary, in this section we showed that the doping of an ultrathin bP semiconductor channel can be controlled using deposition of metal adatoms. In particular, Cu adatoms can serve as a good electron dopant and allow bP to operate as an n-FET. Numerical calculation showed that the Cu adatoms bond strongly to the crystal surface, but do not introduce any gap-states and do not affect the edges of the conduction and valence bands. We demonstrated a method for cluster-free deposition of Cu using sputtering, which was validated in AFM, XPS, UPS and ToF-SIMS characterizations. Electrical transport measurements on a single sample before and after

Cu deposition confirmed the introduction of additional electrons after the Cu deposition. Finally, we fabricated a voltage inverter with the same ultrathin bP crystal for both the p-FET and the n-FET. For the p-FET we used the pristine crystal, while n-FET operation was achieved by selectively doping regions of the material with Cu adatoms. The presented inverter operates at matched input and output voltages of 0 to 2V, exhibits the highest inverter gain achieved with 2D materials to date, and shows good noise margins with noise immunity.

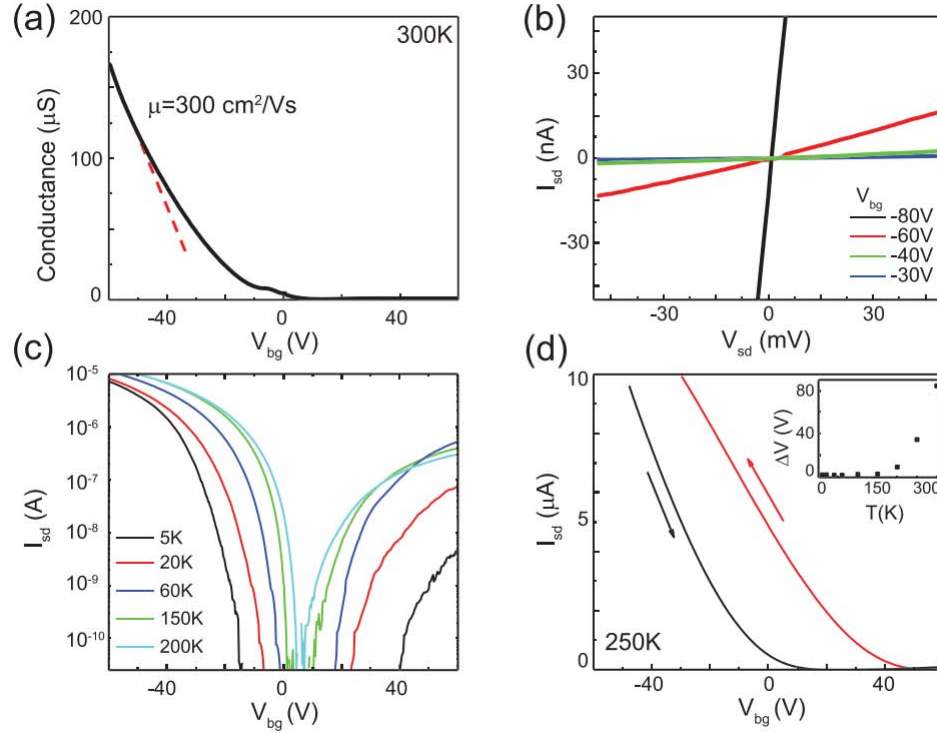


Figure 4.2.3: **(a)** Four-terminal conductance versus back gate voltage of a few-layer phosphorene FET channel. The dashed line shows the linear part of the curve from which a mobility of $300 \text{ cm}^2\text{V}^{-1}\text{s}^{-1}$ is extracted. **(b)** Two-probe $I_{\text{sd}}-V_{\text{sd}}$ characteristic and various gate voltages between -80 V and -30 V at room temperature for the device from (a). **(c)** Two-terminal source-drain current, I_{sd} , against gate voltage, V_{bg} , at various temperatures between 5 K and 200 K . **(d)** I_{sd} versus V_{bg} for two gate sweep directions indicated by the arrows at $T = 250 \text{ K}$ and a sweep rate of 0.1 V/s . The inset shows the difference in threshold voltage, ΔV , between the two sweep directions as a function of temperature (the threshold voltage is taken as the value of V_{bg} at which I_{sd} is equal to 10^{-9} A). Reprinted from *Appl. Phys. Lett.* **104**, 103106 (2014), with the permission of AIP Publishing.

Chapter 5

Critical Discussion

5.1 Comparison to Results from the Literature

5.1.1 Isolation and Electrical Characterization of Ultrathin bP

Several other groups also reported on isolating and characterizing exfoliated bP around the same time as our publication on electric field effect in few-layer bP from 2014 (described in section 4.2). Different reports concentrated on different aspects of the material's properties and all were important for what would turn into a large research interest in ultrathin bP.

Li et al. studied the properties of ultrathin bP transistors.[13] The authors observed pronounced p-type behavior in samples on Si/SiO₂, consistent with the results presented in section 4.2. The authors reported room-temperature mobility of up to 1000 cm²V⁻¹s⁻¹, which is more than three times higher than the value in our devices. However, as seen in Figure 5.1.1(a), their $\mu = 1000$ cm²V⁻¹s⁻¹ point is an outlier with an almost 100% error bar on the logarithmic scale. In subsequent reports the room-temperature mobility has consistently been measured to be closer to 300

$\text{cm}^2\text{V}^{-1}\text{s}^{-1}$, even in cleaner samples with improved low-temperature mobility. Li et al. also performed a study on the thickness dependence of the field effect mobility and drain-current modulation (on-off ratio). They found that the highest mobility is measured in samples with thickness in the range 5 to 10 nm, as seen in the inset of Figure 5.1.1(a). The reduced mobility in thicker samples was attributed to incomplete gating of the channel in the vertical direction, while thinner channels are more heavily affected by degradation on the top surface.

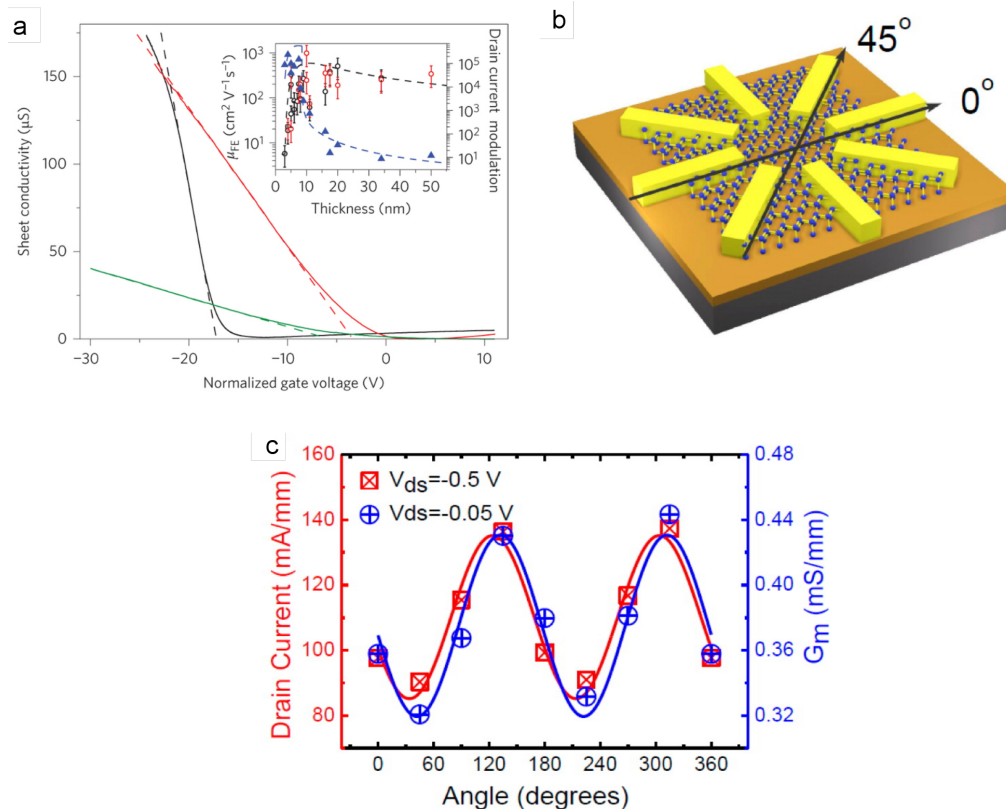


Figure 5.1.1: **(a)** Sheet conductivity measured as a function of gate voltage for devices with different thicknesses: 10 nm (black solid line), 8 nm (red solid line) and 5 nm (green solid line), with field-effect mobility values of 984, 197 and $55 \text{ cm}^2\text{V}^{-1}\text{s}^{-1}$, respectively. Field-effect mobilities were extracted from the line fit of the linear region of the conductivity (dashed lines). All gate voltages are normalized to 90 nm gate oxide for easy comparison. Inset: Summary of drain current modulation (filled blue triangles) and carrier mobility (open circles) of black phosphorus FETs of varying thicknesses. Mobilities measured in four-terminal and two-terminal configuration are denoted by black and red open circles, respectively. Error bars result from uncertainties in determining the carrier density, due to hysteresis of the conductance during gate sweep, and the irregular shape of our samples. The upper bound of the those uncertainties is used to estimate the error bars. Dashed lines indicate the models described in the main text. Adapted by permission from Macmillan Publishers Ltd: Nature Nanotechnology [13], copyright 2014. **(b)** Device structure used to determine the angle-dependent transport behavior. Zero degree is defined by the electrodes, not few-layer phosphorene crystal orientation. **(c)** Angular dependence of the drain current and the trans-conductance G_m of a device with a film thickness of ~ 10 nm. The solid red and blue curves are fitted by the directional dependence of low-field conductivity in anisotropic material with minimum and maximum conductivity times sine and cosine square of the angle. Adapter with permission from [14]. Copyright 2014 American Chemical Society.

Around the same time Liu et al. also reported on the properties of exfoliated bP.[14] The authors were able to isolate a large enough single layer for performing photo-luminescence characterization and measured a band-gap energy of 1.45 eV. In electrical characterization of field effect devices the authors found a room-temperature mobility of around $300 \text{ cm}^2\text{V}^{-1}\text{s}^{-1}$ which is consistent with the results presented here in section 4.2. The authors also studied the thickness-dependent mobility and on-off ratio and found results similar to those of Li et al. [13]. Additionally, the authors demonstrated the anisotropy of the electrical transport by measuring the drain current at different crystal orientations, as reprinted in Figure 5.1.1(b)&(c).

In a related paper Xia et al. also studied the properties of exfoliated bP.[15] The authors demonstrated the anisotropy of the conductance, mobility, polarized infrared (IR) extinction, and polarization-resolved Raman spectrum. The authors also found p-type behavior with a room-temperature mobility of around $600 \text{ cm}^2\text{V}^{-1}\text{s}^{-1}$ in a 15-nm-thick crystal and $400 \text{ cm}^2\text{V}^{-1}\text{s}^{-1}$ in 8 nm.

None of these early works showed the degradation of the crystal in ambient air, as found in our paper and Figure 4.2.2 of the thesis.

5.1.2 Passivation of Ultrathin bP

After the first reports on exfoliated bP a considerable amount of work was focused on exploring techniques for protecting the crystal against degradation. In section 4.3 we demonstrated an all-2D-materials passivation technique based on the transfer of graphene or hBN in inert gas atmosphere. However, other approaches were also explored and reported in the literature.

Wood et al. studied the passivation of exfoliated bP by protecting the surface with a layer of AlO_x grown by atomic layer deposition (ALD).[88] This technique is

scalable and, therefore, potentially more useful for large-scale production than our all-2D-materials approach. However it does not allow the fabrication of pristine bP devices without any ALD chemical precursor treatment and the study of pristine samples, as described in section 4.3. Nevertheless, the authors also observed an increase in the p-type doping upon increasing the exposure to air which is consistent with our measurements that passivated samples show intrinsic behavior, see Figure 5.1.2. Other works also studied the passivation of exfoliated bP using aluminum oxide.[89, 90]

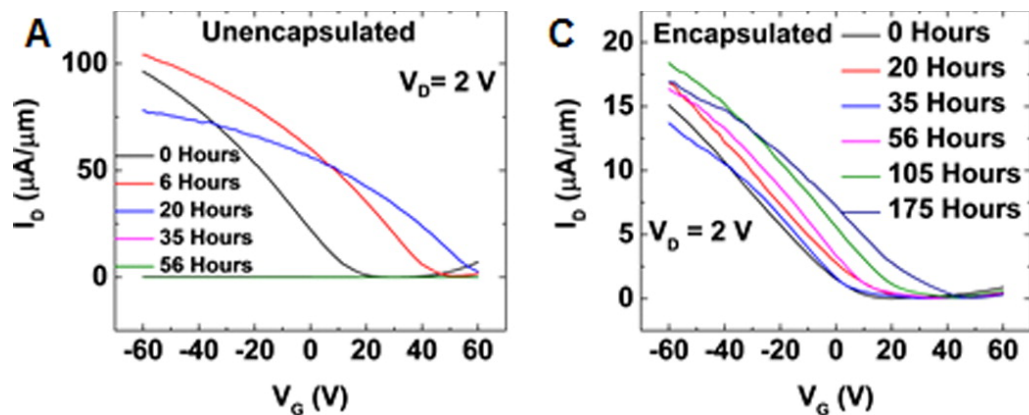


Figure 5.1.2: (a) Transfer curves for an un-encapsulated bP FET with Ti/Au contacts, measured as a function of ambient exposure time. (b) Transfer curves for a $\sim 30\text{ nm}$ thick ALD AlO_x encapsulated bP FET with Ti/Au contacts, measured as a function of ambient exposure time. Adapter with permission from [88]. Copyright 2016 American Chemical Society.

Around the same time Avsar et al. demonstrated a full encapsulation of ultra-thin bP using 2D materials in an inert atmosphere.[91]¹ The authors pre-fabricated equally-spaced graphene stripes on Si/SiO₂ which would serve as source and drain electrodes. The electrodes were transferred on an exfoliated hBN crystal. Ultra-thin bP was exfoliated inside an Ar-filled glovebox and the hBN crystal with the graphene electrodes was transferred on top. Metal contacts were then fabricated to

¹The work by Avsar et al. was also performed in the group of Prof Barbaros Özyilmaz.

the graphene stripes. A schematic of the device structure is shown in Figure 5.1.3(a). In the studied devices the authors found only p-type conduction, which can be explained by the fact that the resistance is dominated by the graphene-bP interface, i.e. the device operates as a Schottky-barrier transistor. This is seen from the overall low current through the device. The device structure did not allow a direct comparison of how the degradation affects the material properties in two nearby regions of the same single crystal like in section 4.3 of this thesis. However, in [91] the ultrathin bP is fully encapsulated with hBN and the device was shown to exhibit the same transport characteristics in air and in vacuum, as shown in Figure 5.1.3(b), as well as unchanged transport characteristics after two months of air exposure.

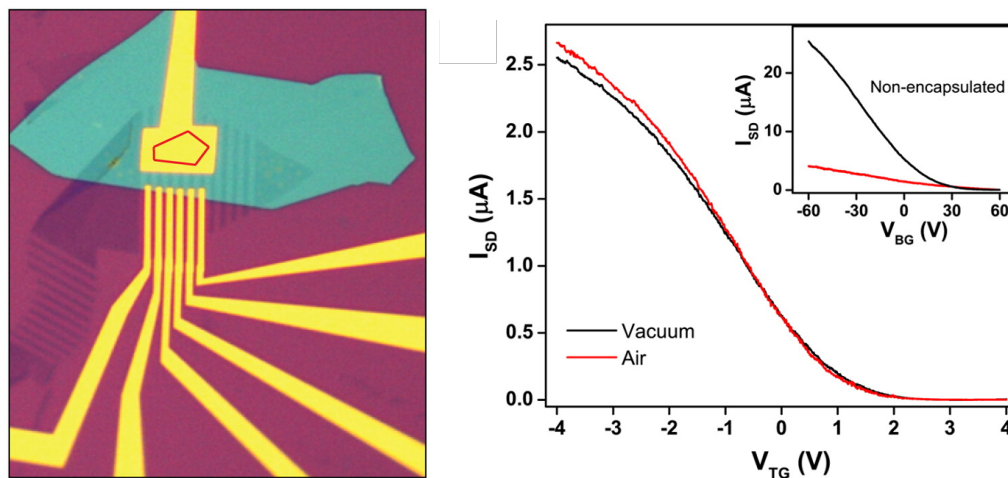


Figure 5.1.3: **(a)** Optical image of fully encapsulated bP with graphene contacts. The bP crystal is outlined by the red polygon under the Au top gate. The blue-green polygon is the hBN crystal. The graphene stripes and Au contacts are also visible. **(b)** Device characteristics of the fully encapsulated device in air and in vacuum, showing identical electrical curves. Adapter with permission from [91]. Copyright 2015 American Chemical Society.

5.1.3 High-Mobility Ultrathin bP on hBN Substrate

The goal of obtaining high-mobility ultrathin bP by transferring it onto hBN, as described in section 4.4, was perused also by other groups.

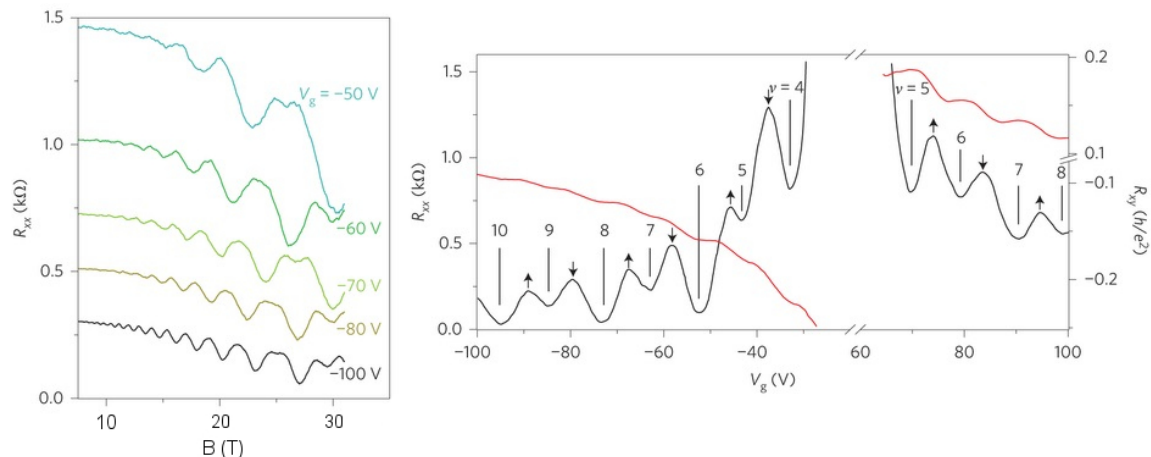


Figure 5.1.4: **(a)** Longitudinal resistance, R_{xx} , as a function of magnetic field measured at varying gate voltages. SdH oscillations are observed for both holes (upper panel) and electrons (lower panel). Curves are shifted vertically for clarity. **(b)** R_{xx} (black) and R_{xy} (red) measured as a function of V_g with magnetic field fixed at $B = 31$ T. The fill factor at each valley is marked. Spin degeneracy is lifted at each Landau level (LL), and the arrows indicate the spin-up and spin-down LLs. Data in a and b were obtained at $T = 0.3$ K. Adapted by permission from Macmillan Publishers Ltd: Nature Nanotechnology [92], copyright 2014.

Li et al studied ultrathin bP transferred onto hBN using an improved higher-quality bulk material.[92] This allowed them to reach low-temperature mobility of over $1000 \text{ cm}^2\text{V}^{-1}\text{s}^{-1}$ and measure Shubnikov–de Haas oscillations in high magnetic field, see reprinted in Figure 5.1.4. Around the same time Gillgren et al. and Cao et al. demonstrated encapsulation by “sandwiching” bP with hBN on both sides, and obtained even higher mobility of around $4000 \text{ cm}^2\text{V}^{-1}\text{s}^{-1}$ at low temperature.[93, 94] All three works validate the results and discussion in section 4.4 where we showed that reduced charged impurity density and encapsulation with a high- k dielectric increase the CI-limited mobility. We attribute our inability to obtain high mobility (at that

point in time) by the fact that we did not have a high-quality bulk material at our disposal. Since then mobility of over $1000 \text{ cm}^2\text{V}^{-1}\text{s}^{-1}$ has been achieved in our group with better bulk crystals, see section 4.5.

5.1.4 Adatom Functionalization and Electron Doping of Ultrathin bP

Prior to our metal-adatoms work Xiang et. all demonstrated n-type doping of bP by in situ deposition of Cs_2CO_3 from a Knudsen cell, see Figure 5.1.5(a).[95] However this technique requires deposition of around 0.2 nm thick films on the crystal surface which induces additional impurity scattering. The authors measured low electron mobility values of round $30 \text{ cm}^2\text{V}^{-1}\text{s}^{-1}$.

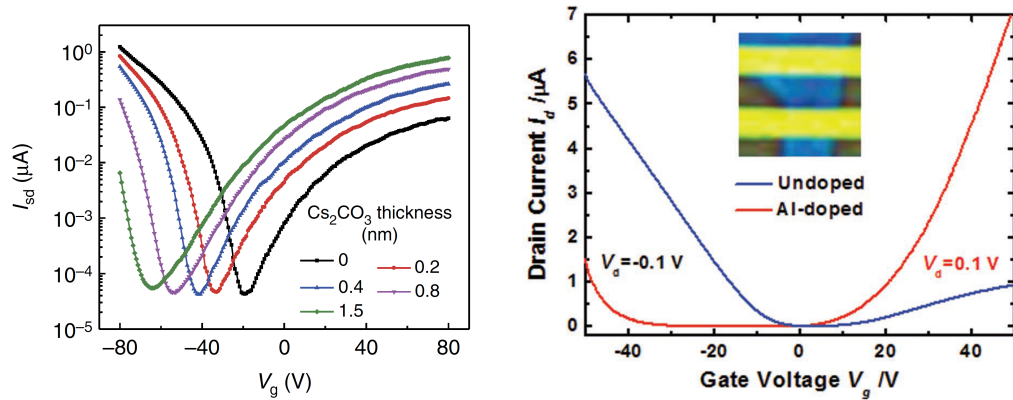


Figure 5.1.5: **(a)** Forward transfer characteristics (V_g from -80 to 80 V) evolution of a bP FET measured at $V_{sd}=100 \text{ mV}$ in logarithmic scale with increasing Cs_2CO_3 thickness from 0 to 1.5 nm. Adapted by permission from Macmillan Publishers Ltd: Nature Communications [95], copyright 2015. **(b)** Comparison of the transfer curves for pristine and Al-doped bP FETs explicitly shows the dominant n-type conduction behavior in the Al-doped device. Adapted from [96] with permission from Wiley.

Eight months after our experimental demonstration of electron doping using metal adatoms, a similar approach was employed by Prakash et al. using Al adatoms.[96] The Al dopants were deposited in an ALD system by pulsing a trimethylaluminium

precursor, followed by growth of an Al_2O_3 encapsulation layer. The authors found that the resulting devices exhibit pronounced n-type behavior with a threshold voltage of almost 0 V and no reduction in the on-off current ratio, see Figure 5.1.5(b). This validates our approach of using metal adatoms for doping of few-layer bP, and in particular for use as electron donors.

5.2 What Makes Phosphorene Interesting?

Since the initial publications on exfoliation and electric field effect in ultrathin bP in 2014 the material has aroused great interest and research efforts. In an interval of three years the research on ultrathin bP has resulted in over 1000 peer-reviewed publications and several review articles.[97, 98, 99, 100] Here I will present my interpretation on the important aspects that have made ultrathin bP a unique and distinct member of the 2D materials family.

(1) Ultrathin bP is the only other mono-atomic 2D crystal besides graphene. It is composed entirely of P atoms and, similarly to Si and graphene, allows the opportunity to grow high-purity crystals.

(2) Ultrathin bP is outside the TMDC material family, which was the only source of semiconducting 2D materials before 2014. This made the isolation of ultrathin bP unanticipated, as highlighted by the overview of Figure 2.1.4, which was published in 2013 shortly before the first works on bP.

(3) The material has a thickness-dependent band gap between 0.3 eV and 1.5 eV. This bridges a region between graphene nano-ribbons with band gap below 0.3 eV and monolayer TMDCs (MoS_2 and WS_2) with band gaps above 1.5 eV.

(4) The material exhibits relatively high mobility. The values are lower than in graphene but higher than in semiconducting TMDCs. Currently it is one of few crystal

with high enough mobility for observing quantum oscillations at low temperature. Considering that research is still at an early phase it is likely that the electronic quality will get even better.

(5) Ultrathin bP is the first 2D material with a large in-plane anisotropy. In contrast to graphene and TMDCs, it exhibits pronouncedly directional-dependent properties.

(6) The crystal was found to be gradually degrading in ambient air but was stable enough for initial characterizations. This has made it one of the first widely-studied 2D materials for which passivation is essential. It is likely that after bP the search for new 2D materials will expand towards less stable crystals, including silicene (2D Si)[101].

5.3 Ultrathin bP for opto-electronic applications

Besides in transistor applications, the electronic properties of ultrathin bP make the material very promising for opto-electronic applications. The material exhibits a direct band gap in the bulk form and all the way down to monolayer thickness. [54] The thickness dependence of the direct band- gap, ranging from 1.8 eV in monolayer to 0.6 eV in five-layer thickness was recently demonstrated experimentally in photoluminescence measurements. [102] This allows bP to be used as a sensitive material for photo-detection and photovoltaics in the wavelength range from around 4.1 μm to 680 nm, which covers the technologically important interval from visible to mid-infrared light. The fact that the band gap in bP remains direct for all number of layers is in marked contrast to TMDCs, which exhibit a direct band gap only in monolayer crystals. This makes bP a unique 2D material that allows tuning of the band gap energy and potential development of infra-red and multi-spectral opto-electronic devices.

[103, 104] Furthermore, the observation of robust and spatially anisotropic excitons in monolayer bP suggests further promising future of the material in opto-electronic devices.[105]

5.4 Ultrathin bP: Prospects and Future Challenges

Ultrathin bP was found to exhibit electronic properties which make it a technologically-relevant material. It is a semiconductor allowing both good on-off ratios and high mobility. It has almost equal effective masses for holes and electrons, which make ultrathin bP particularly promising for CMOS-like devices, in stark contrast to MoS₂ and WS₂. The narrow band gap, which can be made even lower with As doping, holds potential for infra-red optical devices in the mid-infrared region.[104] The air instability is a disadvantage at first consideration, but in fact the higher chemical reactivity could allow much better control of the doping using surface adsorbents, unlike MoS₂ where controlling the threshold voltage has proved a major challenge. Furthermore, the crystal is made entirely of P atoms, which is the 13-th most abundant element on Earth. In contrast, TMDCs include rare-earth elements like Mo and W, which are much more scarce and expensive.

All of the above considerations show that ultrathin bP is indeed a technologically-relevant material that could find many applications **if** a number of important material problems can be solved in an efficient manner in the near future. Some of these challenges are common for all 2D materials and are briefly discussed in the following sections.

5.4.1 Large-scale Growth of Ultrathin bP

Arguably the biggest challenge for now is finding a way to grow large area (wafer-scale) ultrathin bP with good crystallinity. In the case of graphene, monolayer CVD growth from CH_4 gas on metal substrates was developed around 5 years after the first exfoliation.[29, 106] During the past 3-4 years researchers have also been actively developing and optimizing the CVD growth of TMDCs from solid and gas precursors.[107] In order to become viable for technological applications, ultrathin bP must also be grown on a large scale.

In principle, P forms the chemical compound PH_3 which at room temperature is a gas with a structure similar to that of CH_4 . The gas is called phosphine and is a possible starting point for the growth of CVD ultrathin bP. However, the gas is highly flammable and toxic, which is probably the main reason why no one has reported on attempting CVD growth with it so far. Because of the higher reactivity of phosphorus it is also not clear whether a metal film would provide the optimal substrate. It appears more likely that the growth could be achieved directly on SiO_2 or on semiconductor substrate like Si, or Ge. The (only) positive thing about PH_3 is that the gas is already being used as n-dopant for Si in some semiconductor facilities, so the industry does have experience in handling it.

Another potential approach for growing large-scale ultrathin bP is to try to crystallize thin red phosphorus films under high pressure. One can envision a process where red phosphorus is deposited using evaporation or sputtering, and the film is then brought to high pressure.

Whether these approaches would work remains to be seen. But it appears that the next milestone for ultrathin bP has to be the demonstration of large-area growth.

5.4.2 Isolation and Characterization of High-Quality Monolayers

So far most of the research on ultrathin bP is performed on crystals with several nanometer thickness. Isolation of large monolayer crystals has proven much more difficult than for graphene and TMDCs, probably due to the reactivity in air which quickly degrades monolayer sheets. There have been only few characterizations and studies on the monolayer material. An optimized method for reproducibly isolating monolayer crystals, even at a scale of a $10 \times 10 \mu\text{m}^2$ and using exfoliation-based techniques, would constitute important progress enabling further studies on the monolayer the material.

5.4.3 Optimization of the Device Control

Methods for controlling the doping level and threshold voltage in bP-based transistors are already being developed and reported on, including in this thesis. The further development and optimization of such methods is an important prerequisite for potential electronic applications. 2D materials achieve their excellent transport characteristics partly because of the absence of impurity dopants. However, in bulk Si transistor technology the doping level is a crucial design parameter which gives device engineers the most direct handle for modeling and tuning the device characteristics. Substitutional doping is not a viable option for 2D materials because it significantly deteriorates their electronic properties. The optimization and development of surface charge-transfer methods, like metal adatoms, which do not distort the lattice, will probably be of great importance.

5.4.4 Long-term Passivation

Methods have already been developed and demonstrated for the chemical passivation of ultrathin bP, including in this thesis. However, these methods have so far been tested on time scales of days to a few months at most. Being inherently more reactive, it is still not clear whether ultrathin bP can survive over a period of years even when encapsulated. This question has to be addressed using more precise degradation studies, which can quantify the passivation and can predict the total lifetime of a device.

Chapter 6

Conclusion

In this thesis I showed results on the isolation and electrical characterization of a new two-dimensional material, exfoliated from bulk bP, and called ultrathin bP. Similarly to the bulk crystal, the 2D material was found to be a high-mobility semiconductor. It was shown that the electrical transport of the ultrathin material can be tuned using the electric field effect, thereby allowing the fabrication of the first FETs based on bP. The ultrathin material was found to slowly degrade in ambient atmosphere during a time period of several hours to several days. I demonstrated a process for the passivation of exfoliated bP using dry transfer of graphene or hBN in an inert gas glovebox. The process allowed, for the first time, to study bP surfaces that have not undergone any exposure to air. The pristine unoxidized material was found to exhibit nearly symmetric electron and hole transport, which is consistent with its intrinsic band structure. Oxidation was found to induce unintentional p-doping, which might be the reason for the unintentional effective acceptor concentration in bulk bP. Furthermore, I studied the electrical transport of ultrathin bP on an hBN substrate and argued that the mobility in the early samples was limited by charged impurity scattering. Finally, it was demonstrated that metal adatoms deposited on the few-layer crystal

can be used to control the doping level and the threshold voltage. This allowed the fabrication of an all-2D-materials voltage inverter which utilizes the same bP crystal for both the p-FET and the n-FET. The developed adatom functionalization process is scalable and the characterized inverter operates at matched input-output voltages and exhibits excellent gain and noise margins. The results presented in this thesis constitute some of the first electrical transport studies on ultrathin bP.

Bibliography

- [1] Fagan, B. M. The three-age system. In *The Oxford Companion to Archaeology* (Oxford University Press, 1996).
- [2] Tylecote, R. F. *A history of Metallurgy* (The Metals Society, 1976).
- [3] Webster, F. *Theories of the Information Society* (Routledge, 2014), 4th edn.
- [4] The story of the intel 4004. <http://www.intel.com/content/www/us/en/history/museum-story-of-intel-4004.html>.
- [5] Schaller, R. R. Moore's law: past, present and future. *IEEE Spectrum* **34**, 52–59 (1997).
- [6] Hoefflinger, B. (ed.) *CHIPS 2020 VOL.2:New Vistas in Nanoelectronics* (Springer International Publishing, 2016).
- [7] Waldrop, M. M. The chips are down for Moore's law. *Nature* **530**, 144–147 (2016).
- [8] Heath, J. R. Molecular electronics. *Annual Review of Materials Research* **39**, 1–23 (2009).
- [9] Ezziane, Z. DNA computing: applications and challenges. *Nanotechnology* **17**, R27 (2006).

- [10] Ladd, T. D. *et al.* Quantum computers. *Nature* **464**, 45–53 (2010).
- [11] AB, N. M. The nobel prize in physics 2010.
<http://www.nobelprize.org/nobelprizes/physics/laureates/2010/>.
- [12] Novoselov, K. S. *et al.* A roadmap for graphene. *Nature* **490**, 192–200 (2012).
- [13] Li, L. *et al.* Black phosphorus field-effect transistors. *Nature Nanotechnology* **9**, 372–7 (2014).
- [14] Liu, H. *et al.* Phosphorene: an unexplored 2D semiconductor with a high hole mobility. *ACS Nano* **8**, 4033–41 (2014).
- [15] Xia, F., Wang, H. & Jia, Y. Rediscovering black phosphorus as an anisotropic layered material for optoelectronics and electronics. *Nature Communications* **5**, 4458 (2014).
- [16] Castellanos-Gomez, A. *et al.* Isolation and characterization of few-layer black phosphorus. *2D Materials* **1**, 025001 (2014).
- [17] Novoselov, K. S. *et al.* Electric field effect in atomically thin carbon films. *Science* **306**, 666–669 (2004).
- [18] Geim, A. K. & Grigorieva, I. V. Van der Waals heterostructures. *Nature* **499**, 419–25 (2013).
- [19] Castro Neto, a. H., Guinea, F., Peres, N. M. R., Novoselov, K. S. & Geim, a. K. The electronic properties of graphene. *Reviews of Modern Physics* **81**, 109–162 (2009).

- [20] Momma, K. & Izumi, F. *VESTA*: a three-dimensional visualization system for electronic and structural analysis. *Journal of Applied Crystallography* **41**, 653–658 (2008).
- [21] Oshima, C. & Nagashima, A. Ultra-thin epitaxial films of graphite and hexagonal boron nitride on solid surfaces. *Journal of Physics: Condensed Matter* **9**, 1 (1997).
- [22] Lee, J.-H. *et al.* Wafer-scale growth of single-crystal monolayer graphene on reusable hydrogen-terminated germanium. *Science* (2014).
- [23] Landau, L. & Lifshitz, E. *Statistical Physics*. v.5 (Elsevier Science, 2013).
- [24] Dean, C. R. *et al.* Boron nitride substrates for high-quality graphene electronics. *Nature Nanotechnology* **5**, 722–6 (2010).
- [25] Soule, D. E. Magnetic field dependence of the hall effect and magnetoresistance in graphite single crystals. *Phys. Rev.* **112**, 698–707 (1958).
- [26] Kim, S. *et al.* Direct measurement of the fermi energy in graphene using a double-layer heterostructure. *Phys. Rev. Lett.* **108**, 116404 (2012).
- [27] Nair, R. R. *et al.* Fine structure constant defines visual transparency of graphene. *Science* **320**, 1308–1308 (2008).
- [28] Lee, C., Wei, X., Kysar, J. W. & Hone, J. Measurement of the elastic properties and intrinsic strength of monolayer graphene. *Science* **321**, 385–388 (2008).
- [29] Li, X. *et al.* Large-area synthesis of high-quality and uniform graphene films on copper foils. *Science* **324**, 1312–1314 (2009).

- [30] Beenakker, C. W. J. *Colloquium* : Andreev reflection and Klein tunneling in graphene. *Rev. Mod. Phys.* **80**, 1337–1354 (2008).
- [31] Zhang, Y., Tan, Y.-W., Stormer, H. L. & Kim, P. Experimental observation of the quantum hall effect and Berry's phase in graphene. *Nature* **438**, 201–204 (2005).
- [32] Gorbachev, R. V. *et al.* Strong Coulomb drag and broken symmetry in double-layer graphene (2012).
- [33] Gorbachev, R. V. *et al.* Detecting topological currents in graphene superlattices. *Science* **346**, 448–451 (2014).
- [34] Schwierz, F. Graphene transistors. *Nature Nanotechnology* **5**, 487–96 (2010).
- [35] Radisavljevic, B., Radenovic, A., Brivio, J., Giacometti, V. & Kis, A. Single-layer MoS₂ Transistors. *Nature Nanotechnology* **6**, 147 – 150 (2011).
- [36] Wang, Q. H., Kalantar-Zadeh, K., Kis, A., Coleman, J. N. & Strano, M. S. Electronics and optoelectronics of two-dimensional transition metal dichalcogenides. *Nature Nanotechnology* **7**, 699–712 (2012).
- [37] Schwierz, F., Pezoldt, J. & Granzner, R. Two-dimensional materials and their prospects in transistor electronics. *Nanoscale* **7**, 8261–8283 (2015).
- [38] Chhowalla, M. *et al.* The chemistry of two-dimensional layered transition metal dichalcogenide nanosheets. *Nature Chemistry* **5**, 263–275 (2013).
- [39] Graphene-like two-dimensional materials. *Chemical Reviews* **113**, 3766–3798 (2013).

- [40] Li, L. J. *et al.* Controlling many-body states by the electric-field effect in a two-dimensional material. *Nature* **529**, 185–189 (2016).
- [41] Schmidt, H., Giustiniano, F. & Eda, G. Electronic transport properties of transition metal dichalcogenide field-effect devices: surface and interface effects. *Chem. Soc. Rev.* **44**, 7715–7736 (2015).
- [42] Sorkin, V., Pan, H., Shi, H., Quek, S. Y. & Zhang, Y. W. Nanoscale transition metal dichalcogenides: Structures, properties, and applications. *Critical Reviews in Solid State and Materials Sciences* **39**, 319 (2014).
- [43] Lipp, A., Schwetz, K. & Hunold, K. Hexagonal boron nitride: Fabrication, properties and applications. *Journal of the European Ceramic Society* **5**, 3 – 9 (1989).
- [44] Tan, J. Y. *et al.* Electronic transport in graphene-based heterostructures. *Applied Physics Letters* **104**, 183504 (2014).
- [45] Kretinin, a. V. *et al.* Electronic properties of graphene encapsulated with different two-dimensional atomic crystals. *Nano letters* **14**, 3270–6 (2014).
- [46] Hattori, Y., Taniguchi, T., Watanabe, K. & Nagashio, K. Layer-by-layer dielectric breakdown of hexagonal boron nitride. *ACS Nano* **9**, 916–921 (2015).
- [47] Radisavljevic, B. & Kis, A. Reply to 'Measurement of mobility in dual-gated MoS₂ transistors'. *Nat Nano* **8**, 147–148 (2013).
- [48] Tung, R. T. Recent advances in schottky barrier concepts. *Materials Science and Engineering: R: Reports* **35**, 1 – 138 (2001).

- [49] Penumatcha, A. V., Salazar, R. B. & Appenzeller, J. Analysing black phosphorus transistors using an analytic schottky barrier mosfet model. *Nature Communications* **6**, 8948 (2015).
- [50] Morita, A. Semiconducting black phosphorus. *Applied Physics A Solids and Surfaces* **39**, 227–242 (1986).
- [51] AB, N. M. The nobel prize in physics 1946. <http://www.nobelprize.org/nobelprizes/physics/laureates/1946/>.
- [52] Bridgman, P. W. Two new modifications of phosphorus. *Journal of the American Chemical Society* **36**, 1344–1363 (1914).
- [53] Endo, S., Akahama, Y., ichi Terada, S. & ichiro Narita, S. Growth of large single crystals of black phosphorus under high pressure. *Japanese Journal of Applied Physics* **21**, L482 (1982).
- [54] Qiao, J., Kong, X., Hu, Z.-X., Yang, F. & Ji, W. High-mobility transport anisotropy and linear dichroism in few-layer black phosphorus. *Nature Communications* **5**, 4475 (2014).
- [55] Keyes, R. W. The electrical properties of black phosphorus. *Phys. Rev.* **92**, 580–584 (1953).
- [56] Warschauer, D. Electrical and optical properties of crystalline black phosphorus. *Journal of Applied Physics* **34**, 1853–1860 (1963).
- [57] Akahama, Y., Endo, S. & Narita, S.-I. Electrical Properties of Black Phosphorus Single Crystals. *Journal of the Physical Society of Japan* **52**, 2148–2155 (1983).

- [58] Ibach, H. & LÄEth, H. *Solid-State Physics: An Introduction to Principles of Materials Science* (Springer-Verlag Berlin Heidelberg, Springer-Verlag Berlin Heidelberg).
- [59] Haigh, S. J. *et al.* Cross-sectional imaging of individual layers and buried interfaces of graphene-based heterostructures and superlattices (2012).
- [60] Mayorov, A. S. *et al.* Micrometer-scale ballistic transport in encapsulated graphene at room temperature. *Nano Letters* **11**, 2396–9 (2011).
- [61] Ferrari, A. C. & Basko, D. M. Raman spectroscopy as a versatile tool for studying the properties of graphene. *Nature Nanotechnology* **8**, 235–46 (2013).
- [62] Wu, J., Mao, N., Xie, L., Xu, H. & Zhang, J. Identifying the crystalline orientation of black phosphorus using angle-resolved polarized raman spectroscopy. *Angewandte Chemie International Edition* **54**, 2366–2369 (2015).
- [63] Bruker. Fastscan-a. <http://www.brukerafmprobes.com/p-3759-fastscan-a.aspx>.
- [64] Akahama, Y., Kobayashi, M. & Kawamura, H. Raman study of black phosphorus up to 13 GPa **104**, 311–315 (1997).
- [65] Vanderborgh, C. a. & Schiferl, D. Raman studies of black phosphorus from 0.25 to 7.7 GPa at 15 K. *Physical Review B* **40**, 9595–9599 (1989).
- [66] Nishii, T., Maruyama, Y., Inabe, T. & Shirotani, I. Synthesis and characterization of black phosphorus intercalation compounds. *Synthetic Metals* **18**, 559–564 (1987).
- [67] Wang, H., Wu, Y., Cong, C., Shang, J. & Yu, T. Hysteresis of electronic transport in graphene transistors. *ACS Nano* **4**, 7221–7228 (2010). 1011.0579.

- [68] Ziletti, A., Carvalho, A., Campbell, D. K., Coker, D. F. & Castro Neto, A. H. Oxygen defects in phosphorene. *Physical Review Letters* **114**, 046801 (2015).
- [69] Koenig, S. P., Wang, L., Pellegrino, J. & Bunch, J. S. Selective molecular sieving through porous graphene. *Nature Nanotechnology* **7**, 728–32 (2012).
- [70] Aguirre, C. M. *et al.* The Role of the Oxygen/Water Redox Couple in Suppressing Electron Conduction in Field-Effect Transistors. *Advanced Materials* **21**, 3087–3091 (2009).
- [71] Pradhan, N. R. *et al.* Ambipolar molybdenum diselenide field-effect transistors: field-effect and hall mobilities. *ACS Nano* **8**, 7923–9 (2014).
- [72] Bao, W., Cai, X., Kim, D., Sridhara, K. & Fuhrer, M. S. High mobility ambipolar MoS₂ field-effect transistors: Substrate and dielectric effects. *Applied Physics Letters* **102**, 042104 (2013).
- [73] Chan, M. Y. *et al.* Suppression of thermally activated carrier transport in atomically thin MoS₂ on crystalline hexagonal boron nitride substrates. *Nanoscale* **5**, 9572–6 (2013).
- [74] Ong, Z.-Y. & Fischetti, M. V. Mobility enhancement and temperature dependence in top-gated single-layer MoS₂. *Physical Review B* **88**, 165316 (2013).
- [75] Ong, Z.-Y., Zhang, G. & Zhang, Y. W. Anisotropic charged impurity-limited carrier mobility in monolayer phosphorene. *Journal of Applied Physics* **116**, 214505 (2014).
- [76] Ma, N. & Jena, D. Charge scattering and mobility in atomically thin semiconductors. *Physical Review X* **4**, 011043 (2014).

- [77] Yu, Z. *et al.* Towards intrinsic charge transport in monolayer molybdenum disulfide by defect and interface engineering. *Nature Communications* **5**, 5290 (2014).
- [78] Sze, S. & Ng, K. *Physics of Semiconductor Devices* (Wiley, 2006).
- [79] Das, S., Chen, H.-Y., Penumatcha, A. V. & Appenzeller, J. High Performance Multilayer MoS₂ Transistors with Scandium Contacts. *Nano Letters* **13**, 100–105 (2013).
- [80] Popov, I., Seifert, G. & Tománek, D. Designing Electrical Contacts to MoS₂ Monolayers: A Computational Study. *Phys. Rev. Lett.* **108**, 156802 (2012).
- [81] Suh, J. *et al.* Doping against the Native Propensity of MoS₂: Degenerate Hole Doping by Cation Substitution. *Nano Letters* **14**, 6976–6982 (2014). PMID: 25420217.
- [82] Soler, J. M. *et al.* The SIESTA method for ab initio order-N materials simulation. *eprint arXiv:cond-mat/0111138* (2001).
- [83] Seah, M. A review of the analysis of surfaces and thin films by aes and xps. *Vacuum* **34**, 463 – 478 (1984).
- [84] NIST. Xps database. <https://srdata.nist.gov/xps/EnergyTypeValSrch.aspx>.
- [85] Park, Y., Choong, V., Gao, Y., Hsieh, B. R. & Tang, C. W. Work function of indium tin oxide transparent conductor measured by photoelectron spectroscopy. *Applied Physics Letters* **68**, 2699–2701 (1996).
- [86] Hu, T. & Hong, J. First-principles study of metal adatom adsorption on black phosphorene. *The Journal of Physical Chemistry C* **119**, 8199–8207 (2015).

- [87] Kulish, V. V., Malyi, O. I., Persson, C. & Wu, P. Adsorption of metal adatoms on single-layer phosphorene. *Phys. Chem. Chem. Phys.* **17**, 992–1000 (2015).
- [88] Wood, J. D. *et al.* Effective passivation of exfoliated black phosphorus transistors against ambient degradation. *Nano Letters* **14**, 6964–6970 (2014).
- [89] Luo, X. *et al.* Temporal and thermal stability of al₂o₃-passivated phosphorene mosfets. *IEEE Electron Device Letters* **35**, 1314–1316 (2014).
- [90] Na, J. *et al.* Few-layer black phosphorus field-effect transistors with reduced current fluctuation. *ACS Nano* **8**, 11753–11762 (2014).
- [91] Avsar, A. *et al.* Air-stable transport in graphene-contacted, fully encapsulated ultrathin black phosphorus-based field-effect transistors. *ACS Nano* **9**, 4138–4145 (2015).
- [92] Li, L. *et al.* Quantum oscillations in a two-dimensional electron gas in black phosphorus thin films. *Nature Nanotechnology* **10**, 608–613 (2015).
- [93] Gillgren, N. *et al.* Gate tunable quantum oscillations in air-stable and high mobility few-layer phosphorene heterostructures. *2D Materials* **2**, 011001 (2015).
- [94] Cao, Y. *et al.* Quality heterostructures from two-dimensional crystals unstable in air by their assembly in inert atmosphere. *Nano Letters* **15**, 4914–4921 (2015).
- [95] Xiang, D. *et al.* Surface transfer doping induced effective modulation on ambipolar characteristics of few-layer black phosphorus. *Nature Communications* **6**, 6485 (2015).

- [96] Prakash, A., Cai, Y., Zhang, G., Zhang, Y.-W. & Ang, K.-W. Black phosphorus n-type field-effect transistor with ultrahigh electron mobility via aluminum adatoms doping. *Small* **1–7** (2016).
- [97] Du, H., Lin, X., Xu, Z. & Chu, D. Recent developments in black phosphorus transistors. *J. Mater. Chem. C* **3**, 8760–8775 (2015).
- [98] Batmunkh, M., Bat-Erdene, M. & Shapter, J. G. Phosphorene and phosphorene-based materials â prospects for future applications. *Advanced Materials* **28**, 8586–8617 (2016).
- [99] Carvalho, A. *et al.* Phosphorene: from theory to applications. *Nature Reviews Materials* **1**, 16061 (2016).
- [100] Kou, L., Chen, C. & Smith, S. C. Phosphorene: Fabrication, properties, and applications. *The Journal of Physical Chemistry Letters* **6**, 2794–2805 (2015).
- [101] Kara, A. *et al.* A review on silicene â new candidate for electronics. *Surface Science Reports* **67**, 1 – 18 (2012).
- [102] Li, L. *et al.* Direct observation of the layer-dependent electronic structure in phosphorene. *Nature Nanotechnology* **12**, 21–25 (2016).
- [103] Engel, M., Steiner, M. & Avouris, P. Black phosphorus photodetector for multispectral, high-resolution imaging. *Nano letters* **2–5** (2014). URL <http://www.ncbi.nlm.nih.gov/pubmed/25299161>.
- [104] Liu, B. *et al.* Black arsenicâphosphorus: Layered anisotropic infrared semiconductors with highly tunable compositions and properties. *Advanced Materials* **27**, 4423–4429 (2015).

- [105] Wang, X. *et al.* Highly anisotropic and robust excitons in monolayer black phosphorus. *Nature Nanotechnology* **10**, 517–521 (2015).
- [106] Reina, A. *et al.* Large area, few-layer graphene films on arbitrary substrates by chemical vapor deposition. *Nano Letters* **9**, 30–35 (2009).
- [107] Wang, S., Wang, X. & Warner, J. H. All Chemical Vapor Deposition Growth of MoS₂:h-BN Vertical van der Waals Heterostructures. *ACS Nano* **9**, 5246–5254 (2015).

Appendix

Mathematica code for the calculation of the temperature-dependent mobility in section 4.4.

Algorithm 6.1

```
Relevant parameters and constants in ATOMIC UNITS (a.u.)
constants
h = 1; "Reduced Boltzmann Constant in a.u.";
e = 1; "Electron Charge i a.u.";
et = 1.0 * 7.956 * 10^(-2); "Dielectric constant of top oxide in a.u.";
eb = 5.06 * 7.956 * 10^(-2); "Dielectric constant of bottom oxide i a.u.";
tox = 188000.97;
"Thickness of top oxide in a.u. , lm = 5.29177x10-11";
g = 2; "Degeneracy";
mx = 0.0826; "Effective electron mass in armchair direction in a.u.";
my = 1.027; "Effective electron mass in zigzag direction in a.u.";
m = Sqrt[mx * my]; "Effective electron mass the polarizability";
"Temperature in Kelvin. Will be converted in a.u. energy below.";
kBT = T * 1.38065 * 10^-23 / (4.35974 * 10^-18);
nn = 0.02 * 10^13; "Charge density in cm^-2. Will be converted in a.u. below";
n = nn * 10^4 * 28.0 / 10^22; "Charge density in a.u.";
Ni = 1.1 * 10^11 * 10^4 * 28.0 / 10^22;
"Impurity density with conversion factor for a.u.";
T = 2.0;

"Chemical potential and Fermi momentum for the given parameters";
EF = N[kBT * Log[Exp[ $\frac{2 * \pi * h^2 * n}{g * m * kBT}$ ] - 1]]
EFx = N[kBT * Log[Exp[ $\frac{2 * \pi * h^2 * n}{g * m * kBT}$ ] - 1]]
kF = N[ $\sqrt{2 * m * Abs[EF]}$  / h]

"This chops
the line from 0 to Emax in number of points.At each energy point,Ee,the
momentum k=Sqrt[2*m*Ee]/h is evaluated and " GAMMA.nb
" is called to determine  $\Gamma$  (E) at each energy point. $\Gamma$  (E) is gathered in a
table GAE."

GAE = {};
Emax = 12 * Abs[EFx];
points = 128;
EforGamma = Table[Emax / points * i, {i, 1, points}];
GAMMAE = {};
b = 1; While[b < points + 1, Ee = EforGamma[[b]];
k = Sqrt[2 * m * Ee] / h; Quiet[NotebookEvaluate[
"C:\Users\A0107966\Dropbox\BP_on_BN_manuscript\analysis\final\
GAMMA_aleks_v3.nb"]]; b++]

"A table is created containg Ee and  $\Gamma$  (Ee) at all points.
The table is then interpolated by a function, GAAEf (E),
in order to take the final intergral for mobility from 0 to Emax.
The devision by 23.476 converts mobility from atomic units to cm2/Vs."
```

Algorithm 6.2

"This is the calculation notebook where the polarizability and screened scattering potential are evaluated. A function PIni(q) is defined (but not evaluated) which numerically integrates μ from 0 to Emax to give the static polarizability."

```
PIni[q_] := Re[NIntegrate[
  (
    
$$\frac{g * m}{2 * \text{Pi} * h^2} * \left( \left( 1 - \text{HeavisideTheta}[q - 2 * \sqrt{2 * m * \mu}] * \sqrt{1 - \left( \frac{2 * \sqrt{2 * m * \mu}}{q} \right)^2} \right) / \right.$$

    
$$\left. \left( 4 * \text{kBT} * \text{Cosh}\left[\frac{\text{EF} - \mu}{2 * \text{kBT}}\right]^2 \right) \right], \{\mu, 0, \text{Emax}\}, \text{MaxRecursion} \rightarrow 32]]$$

```

"Here the numerical integration of the screened potential around the Fermi circle is performed. First the circle is split into 32 points (angles). Then the above defined function is called to determine the polarizability at each angle (momentum q). The momentum, q, at each angle is parametrized by $q = 2 k \sin(\theta/2)$. The values are collected in a table PI which contains the angle in its first column and the polarizability in the second. The values in the second column are replaced to form $\phi^2(1 - \cos(\theta))$ in the second column of table

"int". The table "

int

" is interpolated by a function GAni(θ), which is then integrated from 0 to π and multiplied by 2 (instead of integrating from 0 to 2π)."

```
qq[x_] := 2 * k * Sin[x / 2];
PI = Table[{N[i], PIni[qq[N[i]]]}, {i,  $\frac{\pi}{32}$ ,  $\pi$ ,  $\frac{\pi}{32}$ }}];
int = ReplacePart[PI, {i_, 2} ->  $\frac{2 * \text{Ni}}{(2 * \pi * h)}$  *
  (
    
$$\frac{e^2}{(e^2 * \text{Coth}[qq[\text{PI}[[i, 1]]] * \text{tox}] + e^b) * qq[\text{PI}[[i, 1]]] + e^2 * \text{PI}[[i, 2]])^2} * \left( 1 - \text{Cos}[\text{PI}[[i, 1]]] \right)];$$

  GAni = Interpolation[int];
  GA = m * Integrate[GAni[x], {x, 0, Pi}];
  GAE = Append[GAE, GA];
```


“Without my attempts in natural science, I should never have learned to know mankind such as it is. In nothing else can we so closely approach pure contemplation and thought, so closely observe the errors of the senses and of the understanding, the weak and the strong points of character. All is more or less pliant and wavering, is more or less manageable; but nature understands no jesting; she is always true, always serious, always severe; she is always right, and the errors and faults are always those of man.”

From “Conversations of Goethe”, Johann Peter Eckermann

Translated by John Oxenford

Da Capo Press 1998